UNIVERSITY OF CALIFORNIA, SAN DIEGO

SAN DIEGO STATE UNIVERSITY

Poro-Elasto-Plastic Off-Fault Response and Dynamics of Earthquake Faulting

A dissertation submitted in partial satisfaction of the requirements for the degree of

Doctor of Philosophy

in

Geophysics

by

Evan Tyler Hirakawa

Committee in charge:

University of California, San Diego

Professor Joel Conte
Professor David Sandwell

San Diego State University

Professor Shuo Ma, Chair
Professor Steven Day
Professor Julio Valdes

2016

The Dissertation of Evan Tyler Hirakawa is approved, and it is acceptable in quality and form for publication on microfilm and electronically:

Chair

University of California, San Diego State University

San Diego State University

2016

Dedication

To my wife, Jessica

Epigraph

It must have appeared almost as improbable to the earlier geologists, that the laws of earthquakes should one day throw light on the origin of mountains, as it must to the first astronomers, that the fall of an apple should assist in explaining the motions of the moon.

Sir Charles Lyell

Somewhere, something incredible is waiting to be known.

Carl Sagan

Table of Contents

List of Figures and Tables

Acknowledgements

The road that has brought me here has been an incredible personal journey, but I owe many thanks to the people I have encountered along the way. My foremost gratitude goes to my advisor, Professor Shuo Ma. Since I was an undergraduate, his guidance through the scientific world has been invaluable. Coming in with no research experience, he influenced me to appreciate the thorough investigation of a scientific problem, to become intimately familiar with the literature on a topic (from the fundamental picture to the nearly irrelevant detail), and to not fear questioning the conventional thinking. His relentless attitude toward rigorous detail and innovative ideas has made me a real scientist. None of my accomplishments would have been possible without his help.

I would like to thank all the professors that I have met during my stay in San Diego, who have stoked my passion for geology and geophysics. I am especially grateful to Steve Day, whose extensive knowledge of earthquake and fracture mechanics was indispensable and whose thorough comments improved this dissertation, and Kim Olsen, who provided me with essential education on numerical modeling. Thank you to George Jiracek and Dave Kimbrough, whose excitement for geosciences gave me a thrilling new view on the infinite research possibilities in Earth science; and thank you to Gary Girty and Tom Rockwell, with whom conversations about geology were especially helpful in understanding fault zone rocks. A special thanks to the faculty at IGPP who converted me from a geologist to a geophysicist, especially Dave Sandwell who was very welcoming to me when I first started there and eventually agreed to serve on my committee. Thank you as well to Joel Conte and Julio Valdes for taking the time to eagerly serve on my

committee without knowing much about me. Lastly, thank you to all the faculty members of the SDSU – UCSD Joint Doctoral Program, who gave me the chance to be the first student in a new program.

In addition, I would like to thank the scientists at Lawrence Livermore National Laboratory, for allowing me to spend the summer there as a visiting student researcher. Specifically, thank you to Rob Mellors and Arben Pitarka, who introduced me to the exciting field of explosion seismology. My work with them appears as a chapter in this dissertation.

A special thanks goes to my JDP classmates Qian Yao, Kyle Withers, Bill Savran, Yuval Levy, and Yongfei Wang, who have provided me with countless discussions about science and life, interesting times in Palm Springs hotel rooms, trips to the coffee shop, and strolls around SDSU which made the days much more enjoyable. Other people whose help in the department has been vital over the years are Sem Tran, Pia Parrish, Irene Ochiello, Joan Kimbrough, Tony Carrasco, and Heather Webb.

Most importantly, thank you to my family, whose love and support has always been the crucial factor in my success. To my dad who got me interested in math when I was a young child and made sure I stayed on track in school, and to my mom, Mike and Trevor for always giving me the best advice and giving me a refreshing break from my work when I am on vacation. Another very special thank you to Matt, who has provided me with a lifetime of brotherly competition and has been a constant source of support as we work toward our PhD's. As an older brother you seemed to always beat me in things, but now I am out of grad school while for now you appear to be still in.

Finally, thank you to my wife Jessica, who has been here for me since before I

even knew I wanted to be a scientist, and whose encouragement through my struggles and successes has been unconditional. You were my driving force through all of this; this work is dedicated to you!

Chapter 2, in full, has been submitted for publication of the material as it may appear in *Journal of Geophysical Research – Solid Earth*: Hirakawa, E. T. and S. Ma, Dynamic Fault Weakening and Strengthening by Gouge Compaction and Dilatancy in a Fluid-Saturated Fault Zone. I was the primary investigator and author of this paper.

Chapter 3, in part is currently being prepared for submission for publication of the material. Hirakawa, E. T. and S. Ma, Undrained Gouge Plasticity and Rupture Dynamics of Rough Faults. I was the primary investigator and author of this paper.

Chapter 4, in part is currently being prepared for submission for publication of the material. Hirakawa, E. T. and S. Ma, Coseismic Strengthening of the Shallow Plate Interface Further Enhances Inelastic Wedge Failure and Tsunami Generation. I was the primary investigator and author of this paper.

Chapter 5, in partial form, has been submitted for publication of the material as it may appear in *Bulletin of Seismological Society of America – Short Notes*: Hirakawa, E. T., Pitarka, A. and R. Mellors. Generation of Shear Motion from an Isotropic Expolosion Source by Scattering in Heterogenous Media. I was the primary investigator and author of this paper.

VITA

Evan Tyler Hirakawa

B.S. Geology with Emphasis in Engineering Geology, 2010
San Diego State University

Ph.D. Geophysics, 2016
University of California, San Diego
San Diego State University

RESEARCH EXPERIENCE

Undergraduate researcher, San Diego State University, 2009-2010
Summer of Applied Geophysical Experience (SAGE), 2009
Summer student intern research, Lawrence Livermore National Laboratory, 2015
Graduate student researcher, San Diego State University, 2010-2016

TEACHING EXPERIENCE

Teaching assistant: Geological Data Analysis, San Diego State University, 2011 – 2015
Teaching assistant: Earthquake Seismology, San Diego State University, 2015

PROFESSIONAL AFFILIATIONS

American Geophysical Union
Seismological Society of America
Southern California Earthquake Center

PUBLICATIONS

Ma, S. and E.T. Hirakawa (2013), Dynamic wedge failure reveals anomalous energy radiation of shallow subduction earthquakes, *Earth and Planetary Science Letters*, 375, 113 – 122.

Hirakawa, E.T., Pitarka, A., and R. Mellors (2015), Generation of Shear Motion from an Isotropic Explosion Source by Scattering in Heterogeneous Media, *manuscript submitted for publication to Bulletin of the Seismological Society of America (BSSA)*.

Hirakawa, E.T. and S. Ma (2016), Dynamic Fault Weakening and Strengthening by Gouge Compaction and Dilatancy in a Fluid-Saturated Fault Zone, *manuscript*

submitted for publication to Journal of Geophysical Research – Solid Earth (JGR).

Hirakawa, E.T. and S. Ma, Undrained Gouge Plasticity and Rupture Dynamics of Rough Faults, *paper in preparation*.

Hirakawa, E.T. and S. Ma, Coseismic Strengthening of the Shallow Plate Interface Further Enhances Inelastic Wedge Failure and Tsunami Generation, *paper in preparation*.

CONFERENCE PRESENTATIONS

Hirakawa, E.T. and S. Ma (2011), Station-to-Station Green's Functions Extracted From Seismic Coda in Southern California, *SCEC Annual Meeting,* Palm Springs, CA.

Hirakawa, E.T. and S. Ma (2012), Dynamic Wedge Failure Reveals Anomalous Characteristics of Shallow Subduction Earthquakes, *SCEC Annual Meeting,* Palm Springs, CA.

Hirakawa, E.T. and S. Ma (2012), Anomalous Seismic Radiation in the Shallow Subduction Zone Explained by Extensive Poroplastic Deformation in the Overriding Wedge, *Fall AGU Meeting*, San Francisco, CA.

Hirakawa, E.T. and S. Ma (2013), Strain Localization in the Coulomb Wedge and the Stabilizing Role of Fluids: A New Splay Faulting Model in the Shallow Subduction Zone, *SCEC Annual Meeting,* Palm Springs, CA.

Hirakawa, E.T. and S. Ma (2014), Can Compaction Further Enhance Inelastic Wedge Failure in Shallow Subduction Zone Earthquakes?, *SSA Annual Meeting*, Anchorage, Alaska.

Hirakawa, E.T. and S. Ma (2014), Dynamic Gouge Compaction as a Simple Mechanism for Fault Zone Weakening, *SCEC Annual Meeting,* Palm Springs, CA

Ma, S. and E.T. Hirakawa (2015), Undrained Gouge Response May Diminish the Effect of Fault Roughness on Earthquake Rupture, *Fall AGU Meeting*, San Francisco, CA.

Hirakawa, E.T., Pitarka, A., and R. Mellors (2015), Finite-Difference Modeling of Seismic Wave Scattering in 3D Heterogeneous Media: Generation of Tangential Motion from and Explosion Source, *Fall AGU Meeting*, San Francisco, CA.

ABSTRACT OF THE DISSERTATION

Poro-Elasto-Plastic Off-Fault Response and Dynamics of Earthquake Faulting

by

Evan Tyler Hirakawa

Doctor of Philosophy in Geophysics

University of California, San Diego, 2016
San Diego State University, 2016

Professor Shuo Ma, Chair

Previous models of earthquake rupture dynamics have neglected interesting deformational properties of fault zone materials. While most current studies involving off-fault inelastic deformation employ simple brittle failure yield criteria such as the Drucker-Prager yield criterion, the material surrounding the fault plane itself, known as fault gouge, has the tendency to deform in a ductile manner accompanied by compaction. We incorporate this behavior into a new constitutive model of undrained fault gouge in a dynamic rupture model. Dynamic compaction of undrained fault gouge occurs ahead of the rupture front. This leads to an increase in pore pressure, which preweakens the fault, reducing the static friction. Subsequent dilatancy and softening of the gouge causes a

reduction in pore pressure, resulting in fault restrengthening and brief slip pulses. This leads to localization of inelastic failure to a narrow shear zone.

We extend the undrained gouge model to a study of self-similar rough faults. Extreme compaction and dilatancy occur at restraining and releasing bends, respectively. The consequent elevated pore pressure at restraining bends weakens the fault and allows the rupture to easily pass, while the decrease in pore pressure at releasing bends dynamically strengthens the fault and slows rupture. In comparison to other recent models, we show that the effects of fault roughness on propagation distance, slip distribution, and rupture velocity are diminished or reversed.

Next, we represent large subduction zone megathrust earthquakes with a dynamic rupture model of a shallow dipping fault underlying an accretionary wedge. In previous models by our group [Ma, 2012; Ma and Hirakawa, 2013], inelastic deformation of wedge material was shown to enhance vertical uplift and potential tsunamigenesis. Here, we include a shallow region of velocity strengthening friction with a rate-and-state framework. We find that coseismic increase of the basal friction drives further inelastic wedge failure in comparison with our previous models, with the implication of larger tsunami generation.

Chapter 1

Introduction

In order to better understand earthquakes, some of the most catastrophic natural disasters in recorded history, it is a necessity that we constrain the mechanics of seismogenic faults. The physical conditions at which coseismic processes take place are closely related to fault strength. However, resolving frictional strength at seismogenic depths is a notoriously difficult problem, due to the physical inaccessibility of the fault zone at hypocentral depth and geophysical observations that are often contradictory.

Laboratory studies have shown that for a wide variety of rock types, the coefficient of static friction is consistently 0.6 – 0.85, a result known as Byerlee's law [Byerlee, 1978]. Byerlee's law for the frictional strength of the Earth's crust is partially authenticated by regional stress measurements from a variety of tectonic settings. Absolute stress estimates are consistent with high friction (consistent with Byerlee's law) values and suggest that Earth's crust is critically stressed to incipient failure [Townend and Zoback, 2000].

However, other observations indicate that large plate-bounding faults may be much weaker than indicated by these laboratory experiments. Failure to detect a significant heat flow anomaly centered across the San Andreas Fault (SAF) suggested to early researchers that average frictional stress on the fault is only around 10 – 20 MPa [Brune et al., 1969; Lachenbruch and Sass, 1980]. In addition to this, a general absence of

frictional melt products (known as pseudotachylytes) in the fault core implied relatively low frictional heating, and contributed to the hypothesis that the fault operates at low shear stress [Sibson, 1975; Sibson, 2003]. Furthermore, regional stress measurements suggest that principal stresses are at a high angle to the SAF fault strike, indicating that the fault is a plane of relatively low shear stress [e.g. Zoback et al., 1987; Townend and Zoback, 2004]. Together, these observations have led researchers to believe that the SAF operates at friction coefficients of around 0.1 – 0.2.

These inferences are in contradiction to rock strength inferred by Byerlee's [1978] experiments, as well as the high friction values inferred by the stress state in some faults. It is said that the SAF apparently has very low shear strength in both an absolute and relative sense. This concept is commonly known as the 'stress – heat flow paradox' or the 'weak SAF hypothesis' [Scholz, 2006].

The simplest explanation involving a fault zone consisting of inherently low friction material (like some clays found near the fault zone) is not likely since laboratory experiments indicate that clay materials actually tend to exhibit velocity-strengthening behavior and stable sliding at low strain rates, which are representative of nucleation conditions [Ikari, 2011]. Rate weakening frictional behavior is necessary for nucleation of frictional instability (i.e. stick-slip behavior), and thus for earthquakes to occur.

The necessity of rate-weakening behavior for fault instability implies that some process must be in place by which shear strength drops from some static value to a lower dynamic strength during higher slip rates. Laboratory experiments have confirmed that as the sliding velocity of a frictional surface approaches values typical of coseismic slip rates, frictional strength drops rapidly [e.g. Di Toro et al., 2004; Reches and Lockner,

2010; Goldsby and Tullis, 2011].

In light of this, a class of models has emerged under the presumption of statically strong, dynamically weak faults. Among these are models involving normal interface vibrations and separation [Brune et al., 1993], propagation of a 'wrinkle pulse' [Andrews and Ben Zion, 1997], acoustic fluidization [Melosh, 1979], the formation of silica gel that lubricates the surface [Goldsby and Tullis, 2002; Di Toro et al., 2004], flash heating [Goldsby and Tullis, 2011], and thermal pressurization [Sibson, 1973; Rice, 2006].

One problem with most dynamic weakening mechanisms is that at a specific location, slip is required there for that portion of the fault to be weakened [Scholz, 2006]. Thus, shear stress on faults must reach the statically high frictional values before slip begins and strength drops to the low dynamic level. At seismogenic depth, this corresponds to a huge strength drop that can cause unrealistically large slip velocities and fault parallel strains. For example, Noda et al. [2009] incorporated flash heating and thermal pressurization into a dynamic rupture model and showed that a large strength drop (~100 MPa) led to slip velocities of around ~300 m/s and fault parallel strains on the order of ~0.1. These values are not realistic for real earthquakes. Dunham et al. [2011a] showed that the inclusion of plastic strain in the fault zone reduced the slip velocities to more realistic levels, but the simple plasticity law used may misrepresent the true behavior of the material in the fault core.

One of the main goals of this dissertation is to address the complex relationship between more realistic off-fault material behaviors, pore fluid pressure, and dynamic fault strength. In Chapter 2, I investigate the effect undrained fault gouge deformation has on fault strength. Fault gouge represents the product of continual attrition of fault

material. It consists of an extremely fine-grained matrix, with evidence of continual reworking during each earthquake [Chester et al., 1993]. Laboratory experiments show that in comparison to the relatively dilatant brittle failure and strain softening experienced during deformation of sandstones from the damage zone, fault gouge is more ductile, it readily compacts, and exhibits strain hardening [Chester and Logan, 1986]. Here, I develop a more elaborate approach to modeling the complex properties of inelastic gouge deformation, and compare its effect on rupture dynamics with that of the traditional Mohr-Coulomb yield surface used in most studies. I show that when undrained, the compactant nature of the gouge increases pore pressure and weakens the fault. Shear-enhanced compaction associated with extreme shear stresses ahead of the rupture front causes this process to occur before rupture arrives, and consequently lowers the apparent static friction of the fault. Other proposed dynamic weakening mechanisms do not have this feature. Subsequent dilatancy of the fault gouge during high sliding rates causes the pore pressure to decrease, and restrengthens the fault. This leads to short duration slip pulses, a slip mode that has been inferred by seismological observations [Heaton, 1990].

Over the last few decades, a significant amount of evidence has led to the discovery that faults are actually fractal surfaces, with roughness at all length scales [e.g. Brown and Scholz, 1985; Aviles et al., 1987; Okubo and Aki, 1987; Power and Tullis, 1991; Renard et al., 2006; Candela et al., 2009; Candela et al., 2012]. Because of this, the earthquake modeling community has been increasingly moving in the direction of incorporating these rough faults into studies of rupture dynamics.

Fault roughness leads to a host of interesting rupture characteristics due to the fact that spatially variable tractions on the fault cause its closeness to failure to be

heterogeneous, because slip induces dynamic normal stress changes and redistributes strain energy in the volume near the fault, and because fluctuations in fault orientation affect the distribution of radiated energy. Ruptures will accelerate when propagating into releasing bends, where initial friction is high and the fault is initially closer to failure. The opposite is true at restraining bends, where the low initial friction puts the fault further from failure and causes rupture velocity to slow [Dunham et al., 2011b]. This latter effect can arrest rupture when the initial background stress is too low [Fang and Dunham, 2013]. These fluctuations in rupture velocity have been shown to increase the power of the high frequency part of the seismic wave spectrum [Dunham et al., 2011b], and in 3D lead to site averaged synthetic spectra that are in agreement with empirical estimates in the period range 0.1 – 3.0 seconds [Shi and Day, 2013]. Most recently, it has been found that the rupture process along the fault can become quite chaotic if roughness is high, leading to supershear ruptures, rupture jumps, and rerupture of segments that have already slipped [Bruhat et al., 2016].

In Chapter 3, I apply the undrained gouge model developed in Chapter 2 to a self-similar rough fault. I find that dynamic compaction and dilatancy are amplified at restraining and releasing bends, respectively. This allows rupture to propagate past restraining bends that arrested rupture in a reference case with only Mohr-Coulomb failure. Furthermore, I show that the response of rupture velocity is reversed in respect to those models, where weakening from undrained compaction at restraining bends actually causes ruptures to accelerate, and strengthening by undrained dilatancy at releasing bends causes ruptures to decelerate. Chaotic rupture behavior, as described by Bruhat et al. [2016], is prevented by the stabilizing effect of the dynamic fluid pressure change.

Apart from strike-slip faults, other large, plate-bounding faults seem to present characteristics that are perplexing. The study of accretionary wedges and large subduction zone megathrusts is significant, as the faults here host some of the world's largest earthquakes. Recent notable examples were the 2004 Sumatra earthquake and the 2011 Tohoku earthquake. Both had magnitudes of over M_w 9.0 and caused devastating tsunamis that caused thousands of fatalities. A rare class of earthquakes known as 'tsunami earthquakes' [Kanamori, 1972] occurs in the shallowest part of the subduction zone. These are puzzling because this region of the megathrust is traditionally thought to be aseismic (velocity strengthening). Nevertheless, events that rupture this segment produce much larger tsunamis than expected from their moment magnitudes, radiate low levels of high frequency energy, have slow rupture velocities and long duration, and low energy-to-moment ratios (see Lay et al. [2012] for a review on this topic).

Critical taper theory considers accretionary wedges to be analogous to a wedge of soil or snow in front of a moving bulldozer, where the entire wedge is internally at the state of failure [e.g. Davis et al., 1983; Dahlen, 1984]. In Ma and Hirakawa [2013], we included ideas from this theory in a dynamic rupture model of a subduction zone megathrust, by assuming the overlying wedge to be a critically tapered structure that was on the verge of Coulomb failure. Extensive failure in the wedge led to model predictions corresponding to many of the observations characteristic of tsunami earthquakes, such as large amounts of uplift, lower frequency seismic radiation, and low energy-to-moment ratios. However, in that study we did not consider the shallow portion of the megathrust to be a velocity strengthening region, a commonly held belief.

In Chapter 4, I extend the study of Ma and Hirakawa [2013] to include velocity

strengthening friction in the shallow portion of a subduction zone plate interface, in a rate-and-state framework. The increase in basal friction drives the wedge even closer to failure, increasing off-fault inelastic strain, and enhancing the effects of vertical uplift and implicit tsunamigenesis described in Ma and Hirakawa [2013]. This model supports the quasi-static analytical model of the dynamic Coulomb wedge as described by Wang and Hu [2006], where it was shown that increase in basal friction during a coseismic event will push an accretionary wedge to its critical state.

Overall, the topics discussed in these chapters all lead to a common assertion. To a first approximation, it may be adequate to consider seismogenic faults as localized shear planes of zero width, which accomodate earthquakes in the form of simple elastic rebound. However, the neglect of the finite region that actually accommodates inelastic failure during earthquakes may lead to misinterpretation of geophysical observations and distort our understanding of fault mechanics. In reality, off-fault failure, pore fluids, fault strength, and rupture dynamics are all intimately related.

Finally, In Chapter 5 I depart from the topic of fault physics and focus on another seismic source: explosions. One of the major topics in explosion seismic monitoring is the origin of shear waves from explosions, which are ideally a purely isotropic source. Understanding the shear waves from explosions has implications for earthquake-explosion discrimination, explosion monitoring, and national security. Here, I present a brief study investigating the influence from seismic scattering at small-scale velocity heterogeneities on P-S conversion and tangential motion generated from an explosion source.

References

Andrews, D. J., and Ben-Zion, Y. (1997). Wrinkle□like slip pulse on a fault between different materials. *Journal of Geophysical Research: Solid Earth (1978–2012)*, *102*(B1), 553-571.

Aviles, C. A., Scholz, C. H., and Boatwright, J. (1987). Fractal analysis applied to characteristic segments of the San Andreas fault. *Journal of Geophysical Research: Solid Earth*, *92*(B1), 331-344.

Brown, S. R., and Scholz, C. H. (1985). Broad bandwidth study of the topography of natural rock surfaces. *J. geophys. Res*, *90*(B14), 12575-82.

Bruhat, L., Z. Fang, and E. M. Dunham (2016), Rupture complexity and the supershear transition on rough faults, *J. Geophys. Res. Solid Earth*, *121*

Brune, J. N., Henyey, T. L., and Roy, R. F. (1969). Heat flow, stress, and rate of slip along the San Andreas fault, California. *J. Geophys. Research*, *74*(15), 3821-3827.

Brune, J. N., Brown, S., and Johnson, P. A. (1993). Rupture mechanism and interface separation in foam rubber models of earthquakes: a possible solution to the heat flow paradox and the paradox of large overthrusts. *Tectonophysics*, *218*(1), 59-67.

Byerlee, J. (1978). Friction of rocks. *Pure and applied geophysics*, *116*(4-5), 615-626.

Candela, T., Renard, F., Bouchon, M., Brouste, A., Marsan, D., Schmittbuhl, J., and Voisin, C. (2009). Characterization of fault roughness at various scales: Implications of three-dimensional high resolution topography measurements. *Pure and Applied Geophysics*, *166*(10-11), 1817-1851.

Candela, T., F. Renard, Y. Klinger, K. Mair, J. Schmittbuhl, and E. E. Brodsky (2012), Roughness of fault surfaces over nine decades of length scales, J. Geophys. Res., 117.

Chester, F. M., and J.M. Logan (1986), Implications for mechanical properties of brittle faults from observations of the Punchbowl fault zone, California, *Pure Appl. Geophys.*, 124(1-2), 79-106.

Chester, F.M, Evans, J.P., and R.L. Siegel (1993). Intemal structure and weakening mechanisms of the San Andreas fault. *Journal of Geophysical Research*, *98*(B1), 771-786.

Chester, F. M., Chester, J. S., Kirschner, D. L., Schulz, S. E., and Evans, J. P. (2004). Structure of large-displacement, strike-slip fault zones in the brittle continental crust. *Rheology and Deformation in the Lithosphere at Continental Margins*, *1*, 223-260.

Dahlen, F. A. (1984). Noncohesive critical Coulomb wedges: An exact solution. *Journal of Geophysical Research: Solid Earth*, *89*(B12), 10125-10133.

Davis, D., Suppe, J., and Dahlen, F. A. (1983). Mechanics of fold-and-thrust belts and accretionary wedges. *J. geophys. Res*, *88*(B2), 1153-1172.

Di Toro, G., Goldsby, D. L., and Tullis, T. E. (2004). Friction falls towards zero in quartz rock as slip velocity approaches seismic rates. *Nature*, *427*(6973), 436-439.

Dieterich, J. H., and Smith, D. E. (2009). Nonplanar faults: mechanics of slip and off-fault damage. In *Mechanics, Structure and Evolution of Fault Zones* (pp. 1799-1815). Birkhäuser Basel.

Dunham, E. M., Belanger, D., Cong, L., and Kozdon, J. E. (2011a). Earthquake ruptures with strongly rate-weakening friction and off-fault plasticity, Part 1: Planar faults. *Bulletin of the Seismological Society of America*, *101*(5), 2296-2307.

Dunham, E. M., Belanger, D., Cong, L., and Kozdon, J. E. (2011b). Earthquake ruptures with strongly rate-weakening friction and off-fault plasticity, Part 2: Nonplanar faults. *Bulletin of the Seismological Society of America*, *101*(5), 2308-2322.

Fang, Z., and E. M. Dunham (2013), Additional shear resistance from fault roughness and stress levels on geometrically complex faults, J. Geophys. Res. Solid Earth, 118, 3642-3654.

Goldsby, D. L., and Tullis, T. E. (2002). Low frictional strength of quartz rocks at subseismic slip rates. *Geophysical Research Letters*, *29*(17), 25-1.

Goldsby, D. L., and Tullis, T. E. (2011). Flash heating leads to low frictional strength of crustal rocks at earthquake slip rates. *Science*, *334*(6053), 216-218.

Heaton, T. H. (1990). Evidence for and implications of self-healing pulses of slip in earthquake rupture. *Physics of the Earth and Planetary Interiors*, *64*(1), 1-20.

Ikari, M. J., Marone, C., and Saffer, D. M. (2011). On the relation between fault strength and frictional stability. *Geology*, *39*(1), 83-86.

Kanamori, H. (1972). Mechanism of tsunami earthquakes. *Physics of the earth and planetary interiors*, *6*(5), 346-359.

Lachenbruch, A. H., and Sass, J. H. (1980). Heat flow and energetics of the San Andreas fault zone. *Journal of Geophysical Research: Solid Earth (1978–2012)*, *85*(B11), 6185-6222.

Lay, T., H. Kanamori, C. J. Ammon, K. D. Koper, A. R. Hutko, L. Ye, H. Yue, and T. M. Rushing (2012), Depth-varying rupture properties of subduction zone megathrust faults, *J. Geophys. Res.*, 117, B04311, doi:10.1029/2011JB009133.

Ma, S., and Hirakawa, E. T. (2013). Dynamic wedge failure reveals anomalous energy radiation of shallow subduction earthquakes. *Earth and Planetary Science Letters*, *375*, 113-122.

Melosh, H. J. (1979). Acoustic fluidization: a new geologic process?. *Journal of Geophysical Research: Solid Earth (1978–2012)*, *84*(B13), 7513-7520.

Noda, H., Dunham, E. M., and Rice, J. R. (2009). Earthquake ruptures with thermal weakening and the operation of major faults at low overall stress levels. *Journal of Geophysical Research: Solid Earth (1978–2012)*, *114*(B7).

Noda, H., and Lapusta, N. (2013). Stable creeping fault segments can become destructive as a result of dynamic weakening. *Nature*, *493*(7433), 518-521.

Okubo, P. G., and Aki, K. (1987). Fractal geometry in the San Andreas fault system. *Journal of Geophysical Research: Solid Earth*, *92*(B1), 345-355.

Power, W. L., and Tullis, T. E. (1991). Euclidean and fractal models for the description of rock surface roughness. *Journal of Geophysical Research: Solid Earth*, *96*(B1), 415-424.

Reches, Z. E., and Lockner, D. A. (2010). Fault weakening and earthquake instability by powder lubrication. *Nature*, *467*(7314), 452-455.

Renard, F., C. Voisin, D. Marsan, and J. Schmittbuhl (2006), High resolution 3D laser scanner measurements of a strike-slip fault quantify its morphological anisotropy at all scales, Geophys. Res. Lett., 33, L04305, doi:10.1029/2005GL025038.

Rice, J. R. (2006). Heating and weakening of faults during earthquake slip. *Journal of Geophysical Research: Solid Earth (1978–2012)*, *111*(B5).

Scholz, C. H. (2006). The strength of the San Andreas Fault: A critical analysis. *Geophical Monograph – American Geophysical Union*, *170*, 301.

Shi, Z., and S. M. Day (2013), Rupture dynamics and ground motion from 3-D rough-fault simulations, J. Geophys. Res. Solid Earth, 118, doi:10.1002/jgrb.50094.

Sibson, R. H. (1973). Interactions between temperature and pore-fluid pressure during

earthquake faulting and a mechanism for partial or total stress relief. *Nature*, *243*(126), 66-68.

Sibson, R. H. (1975). Generation of pseudotachylyte by ancient seismic faulting. *Geophysical Journal International*, *43*(3), 775-794.

Sibson, R. H. (2003). Thickness of the seismic slip zone. *Bulletin of the Seismological Society of America*, *93*(3), 1169-1178.

Townend, J., and Zoback, M. D. (2000). How faulting keeps the crust strong. *Geology*, *28*(5), 399-402.

Townend, J., and Zoback, M. D. (2004). Regional tectonic stress near the San Andreas fault in central and southern California. *Geophysical Research Letters*, *31*(15).

Wang, K., and Y. Hu (2006), Accretionary prisms in subduction earthquake cycles: The theory of dynamic Coulomb wedge, *J. Geophys. Res.*, 111, B06410, doi:10.1029/2005JB004094.

Zoback, M. D. et al., (1987). New evidence on the state of stress of the San Andreas fault system. *Science*, *238*(4830), 1105-1111.

Chapter 2

Dynamic Fault Weakening and Strengthening by Gouge Compaction and Dilatancy in a Fluid-Saturated Fault Zone

Abstract

Fault gouge deformation likely plays a significant role in controlling the strength of mature, large-displacement faults. Experiments show that intact gouge deforms in an overall ductile and stable manner, readily compacting, but dilates and experiences brittle failure under large strain rate. We model inelastic gouge compaction and dilatancy using a combined Mohr-Coulomb and end-cap yield criterion in a dynamic rupture model of a strike-slip fault with strongly velocity-weakening friction. We show that large shear stress concentration ahead of the rupture associated with the rupture front causes the gouge layer to compact (e.g., by structural collapse and comminution), leading to rapidly elevated pore pressure and significant weakening of the principal fault surface. Shortly after the rupture front passes, strong dilatancy during strength drop and rapid sliding reduces pore pressure and strengthens the fault, promoting slip pulses. Large strain localization in the gouge layer occurs as a result of rapid gouge dilatancy and strain softening. The combination of pre-rupture weakening from compaction and restrengthening from dilatancy hardening leads to a smaller strength drop, and limits the stress concentration outside the gouge layer. This leads to a reduction of inelastic shear strain in the damage zone, consistent with geological observations and high-speed frictional experiments. Current dynamic rupture models incorporating inelastic off-fault

response may overestimate the effect off-fault damage in the damage zone but underestimate the effect in the gouge layer. With the presence of well-developed fault gouge, the strength of mature faults may be controlled by end-cap, rather than Mohr-Coulomb failure; thus, their frictional strengths are significantly smaller than Byerlee friction.

2.1. Introduction

Resolving the strength of mature, large-displacement, faults has been a longstanding problem in tectonics and earthquake mechanics. Multiple pieces of evidence suggest that these faults may operate at low shear stresses. Failure to detect a heat flow anomaly across the San Andreas Fault (SAF) implies that the dynamic frictional coefficient during past earthquake ruptures is only 0.1 – 0.2 or less [Brune et al., 1969; Lachenbruch and Sass, 1980]. Regional stress measurements also suggest that maximum compressive stresses are at a high angle to the SAF fault strike, indicating low shear stress on the fault [e.g. Zoback et al., 1987; Townend and Zoback, 2004]. In addition, a general absence of frictional melt products (pseudotachylytes) in the fault core implies relatively low frictional heating [Sibson, 1975; Sibson, 2003]. Measurements at other tectonic settings seem to corroborate this view that mature faults are weak [e.g., Suppe, 2007; Fulton et al., 2013; Ujiie et al., 2013].

Yet, laboratory studies have shown that for a wide variety of rock types, static friction of rocks is consistently 0.6 – 0.85, a result known as Byerlee's law [Byerlee, 1978]. Regional stress measurements from a variety of tectonic settings suggest that the crust is critically stressed to incipient failure on preexisting microcracks with friction values consistent with Byerlee's law and hydrostatic pore pressure [Townend and Zoback, 2000]. The inconsistency between the inferred low friction on mature faults and Byerlee's law is the well-known 'stress – heat flow paradox'. Current debate on this topic can be found in Scholz [2006] and Townend [2006]. Noda et al. [2009] and Dunham et al. [2011a] also thoroughly discussed this topic.

In this work we focus on one leading hypothesis to address the heat flow paradox:

the statically strong and dynamically weak fault hypothesis [e.g., Lapusta and Rice, 2003; Rice, 2006; Noda et al., 2009; Dunham et al., 2011a,b], in which both Byerlee's law and heat flow constraints are satisfied. Low dynamic strength is well supported by high-speed frictional experiments [e.g., Di Toro et al., 2011], which demonstrate that rock friction plummets to extremely low values (~0.1) at coseismic speeds. Among various dynamic weakening mechanisms, flash heating [e.g., Goldsby and Tullis, 2011] and thermal pressurization [Sibson, 1973; Lachenbruch and Sass, 1980] are two favorable dynamic weakening mechanisms in earthquake rupture [e.g., Andrews, 2002; Rice, 2006; Noda, et al., 2009].

One possible shortcoming of most dynamic weakening mechanisms and the above hypothesis is that slip is required for the mechanisms to take effect and static friction cannot be reduced [Scholz, 2006]. If Byerlee's law governs static friction, and dynamic friction is governed by dynamic weakening mechanisms, large strength drops (static friction minus dynamic friction) on the order of 100 MPa are inevitable at seismogenic depths. It may be questionable that the fault can sustain such large strength drops. In the model by Noda et al. [2009] that incorporates flash heating and thermal pressurization, large strength drop partly caused slip velocities greater than 300 m/s and fault parallel strain of around ~0.1. Off-fault brittle shear failure can restrict these values towards those that are characteristic of earthquake ruptures [Dunham et al., 2011a]. However, the inelastic off-fault strain in these models may be oversimplified, as we discuss below.

In view of the realization that large off-fault stress concentration associated with rupture propagation can cause material failure [e.g., Poliakov et al., 2002; Rice et al., 2005], dynamic rupture models incorporating off-fault plasticity have become common

[e.g., Andrews, 2005; Templeton and Rice, 2008; Viesca et al., 2008; Duan and Day, 2008; Ma, 2008; Ma and Andrews, 2010; Dunham et al., 2011a,b; Gabriel, et al., 2013; Shi and Day, 2013; Xu and Ben-Zion, 2013; Kang and Duan, 2014], and are supported by geologic observations of complex fault zone architecture formed as a result of irreversible damage [e.g. Chester et al., 1993; Rempe et al., 2013]. These models use the Mohr-Coulomb or Drucker-Prager criteria that mimic brittle off-fault shear failure, and have greatly advanced our understanding of coseismic damage generation and their resulting effects on rupture dynamics. These models, however, ignored the presence of well-developed fault gouge for mature faults.

Fault zone geology consists of a gradational deformation trend, where host rock has been subjected to irreversible damage with progressively increasing intensity towards the main fault trace (Figure 1). This largely comprises a region of mesoscopic brittle deformation that forms the outermost unit of fault zones known as the 'damage zone' (~10 – 100 m thick), but most relevant damage is localized to the highly deformed unit known as the 'fault core', which consists primarily of fault gouge. The fault core becomes especially localized at depth (on the order of 10's of centimeters to meters [Sibson, 2003]). Further localization occurs on an extremely narrow principal fracture surface (hundreds of microns) within the gouge (Figure 1) [also see Rockwell and Ben-Zion, 2007]. Laboratory experiments provide analogous observations where extreme slip localization develops in high-speed friction tests [e.g., Kitajima et al., 2010; Di Toro et al., 2011].

Based on particle size analysis and grain surface area estimates, it is inferred that fracture energy (a factor that significantly contributes to rupture dynamics) in the damage

zone may be less than 10% of that in the fault gouge [e.g. Chester et al. 2005]. Consequently, the behavior of gouge material that is closest to the fault plane should have a much greater effect on rupture dynamics. Lachenbruch [1980] wrote, "… a more complete understanding of the earthquake process will probably require measurements of the permeability of fault zone materials, the width of the active shear zone, and studies of fault gouge dynamics." In this work, we consider the dynamics of fault gouge and investigate how they may contribute to the weakness of mature faults.

While the damage zone typically has the appearance of brecciated host rock or cataclastic rock, the centimeters thick layer of ultracataclasite gouge is a narrow zone of highly deformed, low permeability rock that has experienced large amounts of deformation and grain size reduction (comminution) from frictional wear and grain crushing. In the Punchbowl fault, the gouge consists of a very fine-grained matrix, composed of grains around ~10 μm in diameter which constitute a combination of host rock particles and fragmented vein material (e.g., Chester et al. [1993]).

Apart from textural differences, fault gouge and rock samples from the surrounding damage zone have distinctly different deformational behavior [Chester and Logan, 1986; Scott et al., 1994]. Damage zone rocks deform in a typical elastic-brittle manner accompanied by dilatancy and strain localization, while fault gouge readily compacts and experiences continued compaction and strain hardening in triaxial tests (Figure 2). Although the intact gouge has relatively low initial porosity, structural collapse and comminution under the increase of shear and normal stresses can still cause gouge to compact. The fact that gouge readily compacts leads to an important deformation mode that we consider in this work.

Sleep and Blanpied [1992] proposed interseismic fault zone compaction and the resultant fluid overpressure as a possible mechanism for the weakness of the SAF. Segall and Rice [1995] noted the contradiction with this model, in that extreme pore pressures can drastically reduce effective normal stress, and leave faults in the frictionally stable regime, prohibiting earthquakes from nucleating. Compaction of fault gouge has also been studied in Daub and Carlson [2008], Van der Elst et al. [2012], and Lieou et al. [2014]; in these works, the effects of pore fluids were not considered.

Another important characteristic of gouge deformation is its sensitivity to strain rate. Frictional experiments [e.g., Morrow and Byerlee, 1989; Marone et al., 1990] show that gouge compacts during slow frictional sliding, but dilates when slip rate on the fault increases. Segall and Rice [1995] modeled this rate-dependence by formulating porosity as a state variable that evolves towards a slip rate-dependent steady-state value and coupled it to pore pressure change; this formulation is widely used in models of earthquake cycles and slow slip events [e.g., Segall et al., 2010; Liu and Rubin, 2010]. Recent developments on gouge dilatancy can be seen in Rice et al. [2014].

Here we build on the above works and construct a dynamic model of gouge deformation incorporating both compaction and dilatancy. We will show that the distinct rheology of fault gouge together with undrained fluid response in dynamic earthquake rupture likely exerts a fundamental control on the strength of mature faults. In particular, large shear stress increase ahead of the rupture front causes gouge to compact (shear-enhanced compaction), which leads to increases in pore pressure and reduction of static friction on the fault (also strength drop). During the rapid breakdown process at the rupture front, strong gouge dilatancy reduces pore pressure and strengthens the fault,

promoting self-healing slip pulses, a slip mode that is thought to operate during earthquakes as inferred from seismic data [Heaton, 1990]. In our model, slip pulse generation can occur at higher background shear stress levels than predicted by the theory of Zheng and Rice [1998]; their theory does not include pore fluid effects. Strong dilatancy and softening in the gouge localize shear strain within a narrow zone in the gouge layer with less generation of inelastic shear strain in the damage zone, which is more consistent with geological observations and high-speed frictional experiments.

With well-developed fault gouge in mature faults we suggest that fault strength is likely controlled by end-cap failure, not Mohr-Coulomb failure; thus, fault strength is significantly less than the prediction by Byerlee's law.

2.2. Constitutive modeling

Compaction of porous rocks has been extensively studied in laboratory experiments [e.g., Wong et al., 1997; Baud et al., 2006; Wong and Baud, 2012]. Results show that when the effective confining pressure is low, brittle failure occurs in shear, which often accompanies strain softening and dilatancy. The failure envelope can be well described by the Mohr-Coulomb or the Drucker-Prager criterion, where shear strength increases linearly with effective confining pressure. At intermediate pressures, shear strength is at a maximum and volumetric strain is low. At relatively high confining pressure the shear strength begins to decrease with increasing confining pressures. In this regime, the material fails by compaction and strain hardening. Graphically, an ellipse fits the high confining pressure portion of the failure envelope. Under this yield criterion, compactant failure can actually occur with the increase of shear stress (shear-enhanced compaction). Stefanov et al. [2011] provides a good review of these different regimes.

The characteristics of fault gouge that allow it to readily compact require a yield criterion other than the Mohr-Coulomb or Drucker-Prager criteria which is commonly used to model the damage zone. As a well-constrained gouge yield strength profile for a range of stress regimes is not available, we seek a yield criterion that is qualitatively similar to the strength envelopes found for porous rock deformation, as described above. The new yield surface needs to close at its end to model yielding under isotropic compression. One example of this type of yield surface is the well-known Cam-clay model [Roscoe et al., 1958], which was the first criterion with such a feature and is widely used in soil mechanics. We use a combined yield criterion where the Mohr-Coulomb criterion (a special case of the Drucker-Prager criterion in plane strain) is used to model brittle shear failure (accompanying strain softening and dilatancy) in the low confining pressure regime. At high confining pressure, an elliptical cap is used to model compaction and strain hardening, where the shear strength decreases with increasing confining pressure. This combined yield surface provides a good fit to the strength of porous rocks as found in experiments [Wong et al., 1997; Wong and Baud, 2012], and has been used to model rock compaction [Andrews et al., 2007; Sleep, 2010; Stefanov et al., 2011]. The combined yield criterion that we use is shown in Figure 3.

The mathematical form of the yield surface is given by:

$$\begin{aligned} &\bar{\tau} = c\cos\phi - \left(\frac{\sigma_{kk}}{3} + P\right)\sin\phi, \qquad -\left(\frac{\sigma_{kk}}{3} + P\right) \le S_0 \\ &\left(\frac{-\frac{\sigma_{kk}}{3} - P - S_0}{a_{CAP}}\right)^2 + \left(\frac{\bar{\tau}}{b_{CAP}}\right)^2 = 1, \quad -\left(\frac{\sigma_{kk}}{3} + P\right) \ge S_0 \end{aligned} \tag{1}$$

where $\bar{\tau}$ is the square root of the second invariant of the deviatoric stress tensor in the Drucker-Prager critierion (or the maximum shear stress over all possible orientations in the Mohr-Coulomb criterion), $\frac{\sigma_{kk}}{3}$ is the mean stress, P is pore pressure, c is cohesion, ϕ is the internal friction angle, and S_0 is the effective mean pressure at the center of the ellipse, and a_{CAP} and b_{CAP} are the major and minor semi-axes of the ellipse, respectively. The continuum mechanics stress convention is used in this paper (i.e., compression is negative). S_0 is the effective mean pressure that coincides with the intersection of the Drucker-Prager line and the elliptical end cap. The pressure S_1 at the right end of the cap denotes yielding with no shear, i.e. the crushing pressure.

Strain hardening associated with compaction is represented by cap expansion. We use a combined hardening rule where the cap expands with both increasing inelastic shear and volumetric strains. Specifically, the cap expands by

$$dS_0 = -h_{S_0} K d\varepsilon_{kk}^p + h_\eta G d\eta \,, \tag{2}$$

$$dS_1 = h_{S_1} dS_0 \,, \tag{3}$$

where G is the shear modulus, K is the drained bulk modulus, $d\varepsilon_{kk}^p$ is the increment of the inelastic volumetric strain (repeated indices indicate summation), $d\eta$ is the equivalent inelastic shear strain increment ($d\eta = \sqrt{\frac{1}{2} d\varepsilon_{ij}^{p'} d\varepsilon_{ij}^{p'}}$, where $d\varepsilon_{ij}^{p'}$ is the increment of the inelastic deviatoric strain), and h_{S_0}, h_{S_1}, h_η are hardening parameters. The parameters used in this work are shown in Table 1.

A simple non-associated plastic flow rule is used when the yield criterion is

violated. In the end-cap regime, the direction of the stress adjustment back to the yield surface, which corresponds to a dilatancy angle θ, is given by the line between the temporary elastically updated stress and a point on the horizontal axis halfway between the temporary elastically updated effective mean stress and the center of the ellipse (Figure 3). The enforcement of this flow rule is an ad hoc consideration, as we are not aware of well-documented plastic flow behavior of fault gouge material. Laboratory studies aiming to quantify this behavior will be useful for more realistic future models. Nevertheless, this flow rule qualitatively reproduces the behavior of porous rock deformation. Namely, that the dilatancy angle is a function of effective mean stress and causes a transition from dilation (in the low-stress Mohr-Coulomb or Drucker-Prager regime) to compaction (in the high-stress end-cap regime), with no inelastic volumetric strain at the intermediate stress region, near S_0 [Wong et al., 1997; Stefanov et al., 2011].

During rapid earthquake rupture, the fluid diffusion time is much longer than the travel time of stress waves; thus the undrained condition applies. In the following, we follow closely Viesca et al. (2008) to implement yielding with undrained fluid response.

During plastic flow, the inelastic strain increment can be written as

$$d\varepsilon_{ij}^{p} = d\eta\left(\frac{s_{ij}^{*}}{2\bar{\tau}^{*}} + \frac{\beta_u}{3}\delta_{ij}\right), \tag{4}$$

where s_{ij} is the deviatoric stress, the superscript * denotes the elastically updated temporary stress, β_u is the undrained dilatancy factor $\beta_u = (1-B)\beta$ (β is the drained dilatancy factor, $\beta = \tan\theta$) that gives the ratio of inelastic volumetric strain to inelastic shear strain, i.e. $d\varepsilon_{kk}^{p} = \beta_u d\eta$, and B is Skempton's coefficient. According to Hooke's

law, for isotropic elastic material the corresponding stress adjustment (equivalent to volume density of seismic moment increment) is

$$dm_{ij} = K_u d\varepsilon^p_{kk}\delta_{ij} + 2G\left(d\varepsilon^p_{ij} - \frac{d\varepsilon^p_{kk}}{3}\right), \tag{5}$$

where K_u is the undrained bulk modulus ($K_u = \frac{K}{1-\alpha\beta}$ and α is Biot's coefficient). We further write isotropic and deviatoric components of the stress adjustment:

$$dm_{kk} = 3K_u d\varepsilon^p_{kk} = 3K_u\beta_u d\eta\,, \tag{6}$$

$$dm'_{ij} = \frac{Gd\eta}{\bar{\tau}^*} s^*_{ij}\,. \tag{7}$$

The adjustment in mean stress and inelastic volumetric strain can cause pore pressure change. This important effect can be calculated by

$$dP = -B\frac{dm_{kk}}{3} - \frac{KB}{\alpha}\beta d\eta\,. \tag{8}$$

To adjust stress back onto the yield surface we substitute equations 6 – 8 into the yield criterion (equation 1) and solve for the only unknown, $d\eta$. For the Drucker-Prager yield criterion this can be written as

$$\sqrt{\frac{1}{2}\left(s^*_{ij} - dm'_{ij}\right)\left(s^*_{ij} - dm'_{ij}\right)} = c\cos\phi - \left(\frac{\sigma^*_{kk} - dm_{kk}}{3} + P^* + B\frac{dm_{kk}}{3} - \frac{KB}{\alpha}\beta d\eta\right)\sin\phi, \tag{9}$$

where P^* denotes the elastically updated temporary pore pressure. We obtain the solution

$$d\eta = \frac{\bar{\tau}^* - \bar{\tau}^{yield}}{G + K_u\beta_u(1-B)\sin\phi + \frac{KB\beta\sin\phi}{\alpha}}\,, \tag{11}$$

where $\bar{\tau}^{yield}$ is the yield stress, which is identical to the solution of Viesca et al. [2008]

except that we ignore the hardening during each inelastic strain increment.

Similarly for the end-cap yield criterion we have

$$\left(\frac{-\frac{\sigma_{kk}^{*}-dm_{kk}}{3}-P^{*}+B\frac{dm_{kk}}{3}-\frac{KB}{\alpha}\beta d\eta-S_0}{a_{CAP}}\right)^2+\left(\frac{\sqrt{\frac{1}{2}\left(s_{ij}^{*}-dm_{ij}^{'}\right)\left(s_{ij}^{*}-dm_{ij}^{'}\right)}}{b_{CAP}}\right)^2=1. \qquad (12)$$

This results in a quadratic equation of $d\eta$. We solve it analytically and the minimum root gives the solution for $d\eta$. A similar derivation can be seen in Stefanov et al. (2011), which, however, only considered the dry case. Once $d\eta$ is obtained the stresses and pore pressure are adjusted by using equations 6 - 8.

To model rate-dependence of gouge dilatancy, we follow the formulation of Segall and Rice [1995] for porosity evolution during frictional sliding. When the stress is within the yield surface, we evolve inelastic volumetric strain via the following equations:

$$\dot{\varepsilon}_{kk}^{p}=-\frac{V_{ev}}{L}\left(\varepsilon_{kk}^{p}-\varepsilon_{kk,ss}^{p}\right), \qquad (13)$$

$$\varepsilon_{kk,ss}^{p}=\zeta\sinh^{-1}\left(\frac{V_{ev}}{2V_0}\right), \text{ and} \qquad (14)$$

$$V_{ev}=\xi V\exp\left(-\frac{y^2}{2\delta^2}\right). \qquad (15)$$

Assuming the solid skeleton has a much lower compressibility, inelastic volumetric strain is equivalent to porosity change [Viesca et al., 2008]. Equation 13 is similar to the slip law for state variable evolution in the rate-and-state friction law (shown in the next section in equation 19). Equation 14 provides an expression for steady-state inelastic

volumetric strain $\varepsilon^p_{kk,ss}$ that is well posed at zero velocity, where V_0 is the reference slip velocity used in the rate-and-state friction law, and V_{ev} is evolution velocity. Evolution velocity V_{ev} (equation 15) is a function of slip velocity, V, and also a Gaussian function of distance from the fault (with y being fault-perpendicular distance and δ the standard deviation). A similar concept was used by Sleep [1997]. Segall and Rice [1995] used slip velocity directly for the porosity evolution. The parameters ζ and ξ control the amount of gouge dilatancy during evolution. In the simulations we choose ζ = 1.5 x 10^{-5}, ξ = 0.1, and δ = 1 cm as the baseline case, and will also discuss the effects of varying these parameters.

For a given inelastic volumetric strain increment ($d\varepsilon^p_{kk}$) during dilatancy evolution, we specify the dilatancy angle to be $\theta = \max\left[\tan^{-1}\left(\frac{0.5\bar{\tau}}{-\frac{\sigma_{kk}}{3} - P}, 5°\right)\right]$ and obtain the inelastic shear strain increment by $d\eta = \frac{d\varepsilon^p_{kk}}{\beta_u} = \frac{d\varepsilon^p_{kk}}{(1-B)\tan\theta}$. We then use equations 6 – 8 to apply the corresponding stress and pore pressure adjustments. This dilatancy angle controls the amount of inelastic shear strain and shear strength reduction (strain softening) for a given inelastic volumetric strain increment; smaller angles lead to larger strain softening. We see that as strain softens, this angle decreases, which is consistent with typical rock failure experiments. A minimum angle of 5° is used to limit the amount of softening. Our introduction of equations 13 – 15 inside the yield surface is different from standard plasticity models in which the region inside the yield surface corresponds

to an elastic regime. Here these equations allow us to kinematically model the effect of gouge dilatancy in a rate-and-state framework.

2.3. Dynamic rupture model

We model dynamic rupture on a 2D planar, right-lateral strike-slip fault embedded in a narrow gouge layer that is surrounded by a damage zone (Figure 4). Off-fault material is poro-elasto-plastic. The gouge layer obeys the combined yield criterion described earlier. The damage zone obeys the standard Mohr-Coulomb criterion only. The width of the gouge layer is chosen 20 cm for most cases to be consistent with geological observations (Figure 1); the effect of varying this parameter will also be shown. The fault length is sufficiently long that the rupture never reaches the end of the fault. Elastic material properties are homogeneous, where P-wave velocity, S-wave velocity, and density are V_P = 6000 m/s, V_S = 3464 m/s, and ρ = 2670 kg/m^3, respectively. An element size of 1 cm is used in all the simulations to ensure a good resolution of the gouge layer.

The regional stress field is homogeneous with the maximum compressive stress oriented at 45° to the fault. Initial stresses on the fault are selected to be representative of conditions at seismogenic depth (~7 km). The initial effective normal stress on the fault is -126 MPa.

Zheng and Rice [1998] defined a critical background stress τ_{pulse} given by the intercept of the radiation damping line that is tangent to the steady-state friction curve. They showed that propagation of crack-like ruptures is not possible when the background shear stress is lower than τ_{pulse}, and pulse-like ruptures are only possible in a narrow

range of initial background stresses around τ_{pulse}. For our chosen parameters, τ_{pulse} is 30.64 MPa. In order to produce a range of slip modes (i.e. arresting rupture, crack-like rupture, and pulse-like rupture), we use a range of background shear stresses on the fault between 30 – 40 MPa. Our stress states are similar to the ones used in Dunham et al. [2011a].

The Mohr-Coulomb parameters are the same in both the fault gouge and the damage zone, assuming zero cohesion and an internal friction of 0.85. Ellipse parameters are set so that the initial stress state brings the gouge close to compactant failure. To satisfy this condition, we define a parameter CF_{CAP}, to be the ratio of the initial shear stress to the shear strength, i.e.,

$$CF_{CAP} = \frac{\bar{\tau}^{init}}{b_{CAP}\sqrt{1-\left(\frac{-\frac{\sigma_{kk}^{init}}{3}-P-S_0}{a_{CAP}}\right)^2}} \tag{16}$$

where the superscript *init* indicates that these are initial stress values. The parameter CF_{CAP} is analogous to the closeness-to-failure parameter CF used in studies with Drucker-Prager plasticity [e.g. Templeton and Rice, 2008]. As we will show that compaction is induced mostly by the shear stress increase ahead of rupture front (with negligible change in normal stress), CF_{CAP} is defined by only considering the relative vertical distance to the yield cap. The initial aspect ratio of the ellipse is chosen to be 2 in all simulations, which is motivated by the data for porous rocks [Wong and Baud, 2012]. With these parameters CF_{CAP} alone completely determines the shape and position of the

elliptical cap. We use CF_{CAP} = 0.95 in the baseline case (we also have results for two other cases, CF_{CAP} = 0.75 and 0.85). Parameterization of compactant strength by this method is justified by the observation that gouge readily compacts at different confining pressures (Figure 2). This implies that the ellipse parameters in this study do not represent actual material parameters, but can be thought of as a means to represent the history of the gouge deformation that has brought the stress state close to failure.

A friction law is necessary to govern evolution of fault strength during rupture. Recently, progress has been made in the development of frictional models for fault gouge that employ flash heating for rapid weakening. Elbanna and Carlson [2014] implemented flash heating and temperature-dependent viscoplasticity into a framework of shear transformation zone theory, which takes into the consideration the granular nature of fault gouge and links microscopic to macroscopic heating processes. Platt et al. [2014] used numerical models of friction in gouge with dilatancy and frictional rate-strengthening to study localization zone thickness. Though these recent models are insightful, we use the rate-and-state friction law with strong velocity weakening which mimics flash heating of microasperities, to facilitate comparison with similar studies of dynamic rupture. We follow closely the formulation of Dunham et al. [2011a] [see also Rice, 2006; Noda et al., 2009; Rojas et al., 2009; and Shi and Day, 2013].

In this formulation, shear stress on the fault is always equal to the strength of the fault

$$\tau = f(-\sigma_n - p) = -f\sigma_n^{'} \tag{17}$$

where σ_n and τ are the total normal stress and shear stress on the fault respectively, p

is on-fault pore pressure, and $\sigma_n^{'}$ is the effective normal stress on the fault.

The friction coefficient, f, on the fault is governed by

$$f(V,\psi) = a\sinh^{-1}\left[\frac{V}{2V_0}\exp\left(\frac{\psi}{a}\right)\right], \tag{18}$$

where V is slip velocity, V_0 is a reference slip velocity, a is the direct effect parameter, and ψ is the state variable that evolves according to the slip law:

$$\dot{\psi} = -\frac{V}{L}\left(\psi - \psi_{ss}\right), \tag{19}$$

$$\psi_{ss} = a\ln\left[\frac{2V_0}{V}\sinh\left(\frac{f_{ss}}{a}\right)\right]. \tag{20}$$

The steady-state state variable ψ_{ss} is a function of the steady-state friction f_{ss} that satisfies

$$f_{ss} = f_w + \left(f_{LV} - f_w\right)\left[1+\left(\frac{V}{V_w}\right)^8\right]^{-\frac{1}{8}}, \text{ and} \tag{21}$$

$$f_{LV} = f_0 - \left(b-a\right)\ln\left(\frac{V}{V_0}\right), \tag{22}$$

where f_{LV} is steady-state value at conventional slow slip velocities, V_w is the weakening velocity beyond which flash heating takes effect, and f_w is the weakened friction parameter. All friction parameters are shown in Table 1 and similar to those in Dunham et al. [2011a].

In this work, we require the pore pressure on the fault (equation 17). Calculation of on-fault pore pressure from pore pressures in the volume is not trivial when there is

inelastic strain [Viesca et al., 2008; Viesca and Rice, 2009]. We assume the on-fault pore pressure to be the average of the pore pressures on both sides of the fault in this work. The implications of this assumption will be discussed later in the paper.

Ruptures are nucleated by applying an instantaneous Gaussian perturbation in shear stress. The standard deviation of the Gaussian function is the characteristic extent of the state-evolution region R_0 (16 cm) and the amplitude is such that the sum of the peak perturbation and the background stress equals $0.7\sigma_n^{'}$ at the center of the fault. Due to the extremely small element size (1 cm) each simulation is run for 10 milliseconds (ms), corresponding to a rupture distance of ~30 m, except for one simulation that we ran for 30 ms (corresponding to a rupture distance of ~90 m) to study the off-fault damage profile after a long propagation distance.

2.4. Results

We show inelastic shear strain, inelastic volumetric strain, and pore pressure change in the medium after 8 ms of rupture propagation in the baseline case (Figure 5). Slip velocity and on-fault pore pressure change curves are superimposed on these figures. The dashed lines show the location of the rupture front. Prior to the arrival of rupture, the fault plane experiences shear stress increase from two contributions, both of which lead to shear-enhanced compaction owing to the condition that fault gouge is close to compactant failure. The first is the arrival of the S-wave, which occurs a few meters ahead of the rupture front. This causes a simultaneous increase in pore pressure and an implicit decrease in shear strength on the fault. Following this, the gouge experiences a much larger increase in shear stress related to the approach of the mode II crack tip, an essential concept in fracture mechanics [Freund, 1998]. This crack tip stress dominates

the pre-rupture shear-enhanced compaction and consequent pore pressure increase; the compaction from the S-wave arrival is minor in comparison.

S-wave compaction generates a plateau in the on-fault pore pressure distribution. Because the fault has not slipped, there is no evolution in inelastic volumetric strain, so the pore pressure stays constant until the arrival of the rupture front. Shortly after the rupture front arrives, the on-fault pore pressure drops rapidly. Gouge starts to dilate due to the evolution of inelastic volumetric strain towards a positive steady-state value (equation 14). Large slip rate during strength drop gives rise to a large evolution velocity (V_{ev}), which leads to rapid dilatancy and increase of inelastic shear strain due to softening. The Gaussian function of evolution velocity (equation 15) limits the dilatancy and inelastic shear strain within three standard deviations to the fault, which can be seen as a narrow localized zone behind the rupture front. Outside this localized zone most of the gouge layer remains compacted because of the negligible evolution effect. The inelastic shear strain outside the localized zone is mostly due to plastic yielding during the pre-rupture compaction by the large stress concentration carried by the rupture front.

The strong gouge dilatancy during strength drop rapidly reduces pore pressure and strengthens the fault, which can be seen in the on-fault shear stress distribution. The strengthening locks the fault, generating slip pulses. The fault strengthening due to undrained dilatancy is in addition to the rate strengthening (equations 19 and 20) and is more efficient to quench slip.

The distribution of inelastic shear strain is distinctly different from what is found in off-fault plasticity models using the Mohr-Coulomb or Drucker Prager yield criteria. We provide one example by modeling rupture in the absence of the gouge (i.e. all parts of

the domain obey only the Mohr-Coulomb yield criterion and on-fault pore pressure remains zero), but with otherwise identical parameters (Figure 6). The damage zone characteristic of previous models emerges when the gouge layer is ignored, where a triangular pattern of inelastic shear strain outlines a damage zone that grows with propagation distance (Figure 6b, c). However, in the case with the gouge layer, we see highly localized shear strain within the gouge layer and slightly less inelastic shear strain in the damage zone (Figure 6a, c). The substantially large amount of shear failure in the gouge in comparison with the damage zone is in agreement with geological observations. The decrease in shear failure in the damage zone itself in comparison with the Mohr-Coulomb model is due to the reduction in strength drop (Figure 7), and is supported qualitatively by the notion that off-fault damage should be small, and shear failure is highly localized to the fault core [e.g. Chester et al., 1993; Sibson, 2003; Rockwell and Ben-Zion, 2007].

We show time histories of slip velocity, shear stress, and on-fault pore pressure at a fault node 15 meters from the hypocenter (Figure 7). We compare the results of our end-cap model with simulations with either elastic or purely Mohr-Coulomb off-fault response and no on-fault pore pressure change. Other than the yield surfaces used (or the lack of a yield surface in the elastic case) and lack of on-fault pore pressure change, the three simulations are identical. In the end-cap model, the initial pore pressure increase from S-wave compaction is visible shortly before 4 ms. Subsequent pore pressure increase from compaction due to the arrival of the rupture front is much more significant. At the rupture front the pore pressure increase is already ~27.2 MPa. The maximum pore pressure increase is 34.94 MPa, because a small amount of continued compaction occurs

on the compressional side of the fault after the rupture front arrives (see Figure 8). The peak frictional strength is 25.53 MPa lower than in the elastic case. This corresponds to a decrease in static friction from ~0.68 in the elastic case to ~0.48 in the end-cap case. The strength drop is reduced by ~25 MPa. This reduction in strength drop in conjunction with the contribution from plastic dissipation reduces both the peak slip velocity and rupture velocity in comparison to both the elastic and Mohr-Coulomb cases.

Stress paths at two points on both sides of the fault provide more clarity on the deformation process (Figure 8). Corresponding time histories are also shown to illustrate details of the stress paths. Three stages of deformation can be recognized (identified as I, II, and III). Stage I encompasses the time span before the rupture front arrives. At this stage, shear stress increase first drives the stress point to move vertically upward in stress space, until the stress state reaches the yield cap. Then, yielding causes compaction and drives the stress to the left of stress space, increasing pore pressure and decreasing the effective mean pressure. The first increase and subsequent drop is the S-wave arrival, and the second corresponds to the large shear stress concentration before the arrival of the rupture front (defined as when slip velocity exceeds 10^{-3} m/s). The cap expands as a result of strain hardening. During this stage, the stress state remains nearly the same on both sides of the fault. Slight deviations between stress paths can be seen because the two points are at 0.5 cm (half the element size) from the fault and there are small radiations by P- and S-waves from the inelastic strain (corresponding to seismic potency) behind the rupture front.

Stage II encompasses the time between the arrival of the rupture front and the moment that shear stress drops to its residual value. This is an extremely brief period of

time in comparison with stages I and III; however, it predictably features the most drastic variations in the stress paths. On the compressional side, the mean stress increases during compression and causes further compaction. On the extensional side, the mean stress is reduced, which causes the stress state to reach the Mohr-Coulomb line, and the gouge experiences shear dilatancy. After these brief surges in mean stress change, both sides of the fault experience a large shear stress drop (coinciding with strength drop on the fault) and elastic mean stress relaxation (compressional side becomes more tensile and extensional side more compressive). The sudden onset of sliding during this period causes strong dilatancy evolution within three standard deviations of the evolution velocity to the fault, which leads to additional adjustments on mean and shear stresses.

Finally in stage III, a period of continued dilatancy evolution and rate strengthening occurs until the cessation of slip on the fault. The evolution of inelastic dilatancy reduces pore pressure and increases the effective mean pressure on both sides of the fault. The plastic flow rule we used corresponds to strain softening inside the yield surface, which is a shear stress decrease. Shear stresses on both sides of the fault also increase due to dilatancy hardening on the fault and rate strengthening in the rate-and-state friction law. The interaction of these effects causes the small oscillations in the stress paths in stage III. The kink in the slip velocity time history marks the start of stage III because the combination of these effects all cause the slip velocity to decay at a different rate. Additional increases in shear stress occur as a result of the elastic reloading that occurs in material that has experienced plastic yielding [Templeton and Rice, 2008].

We compare slip contours, inelastic volumetric strain and pore pressure change distributions for three CF_{CAP} cases (0.75, 0.85, and 0.95) in Figure S1. As expected, the

degree of compaction and the resultant pore pressure elevation are less for the cases with lower CF_{CAP} . Although weakening due to the S-wave arrival is not seen in the two lower CF_{CAP} cases, significant overpressure is present in all three cases due to large shear stress increase ahead of rupture front. On-fault pore pressure, shear stress, and slip velocity time histories for the three cases are similar (Figure S2), suggesting that extreme closeness to failure is not a necessary condition for the pre-rupture compaction weakening to occur. Rupture velocity is the largest for the case CF_{CAP} = 0.95. Higher CF_{CAP} induces a larger amount of fracture energy that should lower rupture velocity, but at the same time the fault is weakened from the elevated pore pressure. In this case pre-rupture weakening by compaction is more effective in facilitating rupture propagation than the tendency of plastic dissipation to limit rupture propagation.

To highlight the importance of gouge dilatancy evolution, we compare cases with different values for the dilatancy parameter ξ, a scaling parameter between evolution velocity (V_{ev}) and slip velocity (equation 15). When $\xi = 0$, V_{ev} is also zero, and ε^p_{kk} does not evolve during sliding. Pore pressure on the fault remains high during and after slip, the fault remains weak, and the rupture is crack-like (Figures 9 and 10). The moderate value of $\xi = 0.01$ allows dilatancy to evolve but not as rapidly as in the baseline case (ξ = 0.1). In this case, the rupture initially appears crack-like but becomes pulse-like in later stages. The baseline case with $\xi = 0.1$ allows a typical pulse-like rupture. When $\xi = 1$, rapid dilatancy prohibits rupture propagation.

The effects of the dilatancy parameter, ζ , are illustrated in Figures S3 and S4. The parameter ζ governs steady-state inelastic volumetric strain ($\varepsilon^p_{kk,ss}$). Increasing ζ

corresponds to evolution towards a more dilatant state. For $\zeta = 0$, $\varepsilon^{p}_{kk,ss}$ does not evolve as severely so the pore pressure remains high and keeps the fault relatively weak during sliding. On-fault pore pressure change remains well above zero even after slip stops (Figure S4). As ζ increases, evolution towards higher dilatancy causes pore pressure to drop more rapidly and towards a lower absolute value. Final pore pressure change is negative in the case with $\zeta = 2.5 \times 10^{-5}$. Cases with larger ζ have shorter slip durations, larger residual strengths, smaller strength drops, slip velocities and slips (Figure S4); these are all manifestations of the larger dilatancy effect. For $\zeta = 3.5 \times 10^{-5}$, strong dilatancy prevents rupture from propagating (Figure S3).

The standard deviation (δ) of the Gaussian function for evolution velocity strongly controls the width of the intense inelastic shear strain zone (Figure S5). The decrease of δ lessens the degree of dilatancy evolution and thus allows a greater stress drop (Figure S6). This causes enhanced weakening, as high stress concentrations from larger stress drops lead to more compaction. The actual slip zone can be as narrow as hundreds of microns (Figure 1). For such narrow shear zones we expect that the large dilatancy parameters that Segall and Rice [1995] used ($\xi = 1$ and $\zeta = 1.7 \times 10^{-4}$) can be used to counteract the extreme weakening, while pulse-like ruptures can still be obtained. These results suggest that extreme strain localization in geological observations, weakness of mature faults, and pulse-like ruptures are likely interrelated. In our model, this interrelation is embodied in the undrained gouge compaction and dilatancy driven by the crack-tip stress field.

Varying gouge layer thickness itself leads to an analogous effect (Figure S7). As

the gouge width becomes narrow, plastic dissipation occurs over a smaller area and allows more enhanced compaction.

Figure 11 shows how background shear stress affects the rupture mode (i.e. crack-like or pulse-like) when undrained gouge compaction and dilatancy operate. For comparison, we show slip contours for cases with background stresses between 32 and 40 MPa and equivalent cases with only Mohr-Coulomb failure and no on-fault pore pressure change. For both simulations, ruptures with background stress below τ_b = 33 MPa are quickly arrested. Ruptures begin to take the form of growing slip pulses at τ_b = 33 MPa. In the Mohr-Coulomb case, rupture mode transitions to crack-like at τ_b = 37 MPa. In contrast, the inelastic models maintain pulse-like ruptures for all background stresses above 33 MPa, with slip distributions maintaining qualitative similarity for all cases. This reflects the capacity of undrained dilatancy to more effectively restrengthen the fault and terminate slip, even for high background stresses.

Dynamic weakening from pre-rupture gouge compaction should allow rupture propagation at even lower background stress levels than τ_b = 33 MPa. However, in our model dilatancy evolution starts immediately when the fault is slipping, which strengthens the fault in the nucleation zone and prevents rupture propagation. This is an artifact in the nucleation. When we reduce the amount of dilatancy in the nucleation region, we do observe rupture propagation at lower background stress levels (results not shown here).

2.5. Discussion

Gouge compaction of varying degrees has been reported in recent high-speed

frictional experiments [e.g., Kitajima et al., 2010; Ujiie and Tsutumi, 2010; Faulkner et al., 2011; Ujiie et al., 2013; French et al., 2014]. Kitajima et al. [2010]'s study may be the most descriptive. Their high-speed rotary shear experiments on ultracataclasite from the surface exposure of the Punchbowl Fault revealed four distinct gouge units that developed under varying amounts of slip and slip rate. Units 1 and 2, developed under low slip and slip rate, are slightly compacted and in some cases foliated, but appear to largely maintain the fabric of the undeformed gouge with low shear strain. Units 3 and 4, formed under higher velocities and greater displacements, consist of a more random fabric, are less compacted, and define regions of highly localized slip. Unit 4 exists only in a very narrow region near the frictional surface, while the rest of the gouge consists of less intensely deformed Units 1 – 3. Overall, those findings suggest a process in which gouge deformation initially (under low strains and strain rates) occurs via distributed compaction throughout the majority of the gouge layer with overall maintenance of the original gouge fabric, followed by a period of intense localized and dilatant shearing which only occurs in the immediate vicinity of the fault discontinuity. The overall deformation features in these experiments are similar to our model results, where a compacted region of little shear strain surrounds an extremely narrow dilatant region of intense inelastic shear strain (Figures 5 and 6).

These laboratory studies do not feature rupture propagation due to their small laboratory scales and experimental configurations. Therefore, they do not allow observation of the resulting weakening effect that we model here, which is due to compaction ahead of a propagating rupture.

In contrast to other dynamic weakening mechanisms, this mechanism lowers the

apparent static friction. Large shear stress concentration associated with the rupture front is a physical concept and must exist. Such stress concentrations are probably the largest stresses that the gouge layer experiences during the entire earthquake cycle, and it should not be surprising that it can cause comminution and compaction although the gouge may be over-consolidated during the interseismic period.

Microstructural observations of comminution in the fault gouge provide evidence that this occurs. Chester et al [1993] wrote: "Because of continual reworking, the ultrafine-grained matrix material of the ultracataclasite rocks may be derived, to a large extent, from recomminution of neomineralized material and alteration products." The implication is that comminution is an occurrence in each successive earthquake, and the currently existing gouge microstructures likely represent only the deformation from the last event, rather than the entire fault history.

Fluid overpressure was observed in the high-speed frictional experiments cited above. Most authors attributed it to thermal pressurization, with the exception of Ujiie and Tsutsumi [2010] who suggested that pore pressurization could be due to shear-enhanced compaction. Our model here does not include thermal pressurization. The weakening is due to gouge compaction ahead of rupture front and flash heating during rapid sliding. We show that strong gouge dilatancy during strength drop and rapid sliding reduces pore pressure and promotes slip pulses. Depending on the relative contribution between thermal pressurization and mechanical effects, dilatancy has the potential to diminish the effect of thermal pressurization.

On-fault pore pressure plays an important role in dynamic fault weakening and strengthening in this model. Rudnicki and Rice [2006] and Dunham and Rice [2008]

show that on-fault pore pressure can be represented by a weighted average between the pore pressures on both sides of the fault, and the weights are given by a function of permeabilities and storage coefficients. In this work, we assume that these hydraulic parameters do not change with inelastic deformation (or change by the same amount). The weighted average reduces to a simple average of the pore pressures on either side of the fault.

This should be a valid assumption at least during the pre-rupture weakening phase of the simulation. Ahead of the rupture front, shear stress increases on both sides of the fault, and normal stress change on the fault is nearly zero. Inelastic strains are nearly identical on both sides of the fault. Permeability and storage coefficient changes due to inelastic strain should be nearly symmetric on both sides of the fault, making our assumption valid. However, after rupture commences the two sides of the fault experience different inelastic deformation. Calculating the inelastic storage coefficient is not trivial, but a solution was given by [Viesca and Rice, 2009]. The change in permeability should be much more significant as small changes in porosity can lead to permeability change by orders of magnitude. For example, assuming that permeability increases with porosity, more dilatant failure on the extensional side of the fault should more heavily weight its pore pressure contribution; we may underestimate the restrengthening effects from dilatancy. A more rigorous approach to dynamically updating hydraulic parameters with plasticity may be a topic of future work; however, this will be difficult due to the complicated nonlinear relationship between stresses, elastic and inelastic strains, and permeability [e.g. Zhu et al., 2007].

The microstructural observations of Chester et al. [1993] along with other

petrological and geochemical findings [e.g., Evans and Chester, 1995; Morton et al., 2013; Colby and Girty, 2013] show that fault zone processes may be intimately involved with fluid flow. Sibson et al. [1988] showed evidence for fault-valving behavior, where low permeability seals are broken during rupture and drive trapped overpressured pore fluids up a fault zone that acts as a conduit. Our model suggests that fluid overpressure can also be generated in the gouge itself, which can drive postseismic fluid flow into the damage zone that is coseismically dilated and more permeable (Figures 5 and 6).

Our model also offers an alternative explanation for the overthrust paradox (Hubbert and Rubey, 1959; Price, 1988). Large thrust sheets can move in a piecemeal fashion with transient fluid overpressure on the fault from gouge compaction driven by the dynamic stress field of the rupture front. Pore pressure needs not to be permanently high in the fault zone although we do not argue against its existence.

Zheng and Rice [1998] showed that the critical background stress, τ_{pulse}, represents a stress level below which it is not possible to host crack-like ruptures. The dynamic rupture models of Dunham et al. [2011a] with Drucker-Prager plasticity support this but showed that the different rupture mode regimes shift to higher background stresses due to plastic dissipation (i.e. maintenance of slip-pulses requires higher background stresses). Conversely, Noda et al. [2009] showed that the inclusion of pore fluid increase via thermal pressurization shifted the regimes to lower background stresses (i.e. maintenance of slip-pulses and transition to crack-like ruptures can occur at lower shear stress). Our results show that pulse-like ruptures can be maintained for a wide range of background stresses. Dynamic restrengthening from undrained dilatancy limits ruptures from becoming crack-like in comparison to the Mohr-Coulomb models. The

weakening ahead of the rupture front by compaction also has the ability to host ruptures at lower background stresses than an equivalent Mohr-Coulomb model.

2.6. Conclusions

Mature fault zones contain a well-developed layer of ultracataclasite gouge. Distinctly different from brittle shear failure of rocks in the surrounding damage zone, gouge readily compacts and exhibits velocity-strengthening behavior under slow loading, but dilates when strain rate is high, showing a strong rate-dependence.

We introduce a combined Mohr-Coulomb and end-cap yield criterion to model gouge compaction and dilatancy. The rate-dependence of gouge dilatancy is incorporated using a formulation similar to that of Segall and Rice [1995], allowing inelastic volumetric strain to evolve towards a steady-state value that depends on slip rate and width of the shear zone. Undrained fluid response is also incorporated in this plasticity framework.

Our dynamic rupture simulations with inelastic gouge deformation and flash heating show that large shear stress increase ahead of the rupture front causes gouge to compact. Compaction increases the pore pressure and reduces static friction. Shortly after the rupture front passes, gouge dilatancy during rapid stress breakdown and sliding quickly relieves the fluid overpressure developed during the pre-rupture compaction and restrengthens the fault, promoting slip pulses. Pulselike rupture mode is possible at background stresses higher than those found in the Mohr-Coulomb case. Undrained compaction weakening also allows growing slip pulses at lower background stresses.

Our model produces highly localized shear deformation. While the gouge layer experiences distributed compaction, the inelastic shear strain is highly localized onto a

narrow zone within the gouge, consistent with geological observations and high-speed frictional experiments. Reduction in strength drop limits the stress concentration outside the gouge layer, generating less inelastic shear strain in the surrounding damage zone. This suggests that dynamic rupture models with Mohr-Coulomb or Drucker-Prager plasticity may overestimate the effect of off-fault failure in the widespread damage zone, while underestimating the degree of damage very close to the fault plane.

The shear zone widths in geological observations (~hundreds microns) are much smaller than the centimeters that we model here. As the shear zone narrows, it limits the strengthening effect from dilatancy hardening, and we expect a larger stress concentration ahead of rupture front and more significant pre-rupture compaction weakening. Similarly, the width of active slipping zone in large earthquakes (~ kilometers or more) is much larger than the meter scale that we model, which can also induce much larger stress concentration ahead of rupture front and cause extreme weakening. Thus with well-developed fault gouge we suggest that the fault strength is likely controlled by the end-cap failure, not the Mohr-Coulomb failure. Therefore the strength of mature faults is significantly smaller than the prediction from the Byerlee's law.

Chapter 2, in full, has been submitted for publication of the material as it may appear in *Journal of Geophysical Research – Solid Earth*: Hirakawa, E. T. and S. Ma, Dynamic Fault Weakening and Strengthening by Gouge Compaction and Dilatancy in a Fluid-Saturated Fault Zone. I was the primary investigator and author of this paper.

References

Andrews, D. J. (2002), A fault constitutive relation accounting for thermal pressurization of pore fluid, *J. Geophys. Res., 107*(B12), 2363, doi:10.1029/2002JB001942.

Andrews, D. J. (2005), Rupture dynamics with energy loss outside the slip zone, *J. Geophys. Res.,* 110(B1), doi:10.1029/2004JB003191.

Andrews, D.J. (2007), Compaction can limit peak vertical velocity at Yucca Mountain, American Geophysical Union, Fall Meeting 2007, abstract #S14C-07.

Brune, J. N., Henyey, T. L., and R.F. Roy (1969), Heat flow, stress, and rate of slip along the San Andreas fault, California, *J. Geophys. Res.,* 74(15), 3821-3827.

Byerlee, J. (1978), Friction of rocks, *Pure Appl. Geophys.*, *116*(4-5), 615-626.

Chester, F. M., and J.S. Chester (1998), Ultracataclasite structure and friction processes of the Punchbowl fault, San Andreas system, California, *Tectonophysics*, 295(1), 199-221, doi: 10.1016/S0040-1951(98)00121-8.

Chester, F. M., and J.M. Logan (1986), Implications for mechanical properties of brittle faults from observations of the Punchbowl fault zone, California, *Pure Appl. Geophys.*, 124(1-2), 79-106.

Chester, F.M, Evans, J.P., and R.L. Siegel (1993), Intemal structure and weakening mechanisms of the San Andreas Fault, *J. Geophys. Res., 98*(B1), 771-786.

Colby, T. A., and G.H. Girty (2013), Determination of volume loss and element mobility patterns associated with the development of the Copper Basin fault, Picacho State Recreation Area, SE California, USA, *J. Struct. Geol.*, *51*, 14-37, doi: 10.1016/j.jsg.2013.03.012.

Di Toro, G., Han, R., Hirose, T., De Paola, N., Nielsen, S., Mizoguchi, K., Ferri, F., Cocco, M. and T. Shimamoto (2011), Fault lubrication during earthquakes, *Nature*, 471(7339), 494-498, doi: 10.1038/nature09838.

Daub, E. G., and J.M. Carlson (2008), A constitutive model for fault gouge deformation in dynamic rupture simulations, *J. Geophys. Res.*, *113*(B12), *B12309, doi:10.1029/2007JB005377*.

Duan, B., and S.M. Day (2008), Inelastic strain distribution and seismic radiation from rupture of a fault kink, *J. Geophys. Res.,* 113(B12), doi:10.1029/2008JB005847.

Dunham, E. M., and J.R. Rice (2008), Earthquake slip between dissimilar poroelastic materials. *J. Geophys. Res.,* 113(B9), B09304, doi:10.1029/2007JB005405.

Dunham, E. M., Belanger, D., Cong, L., and J.E. Kozdon (2011a), Earthquake ruptures with strongly rate-weakening friction and off-fault plasticity, Part 1: Planar faults, *Bull. Seismol. Soc. Am.,* 101(5), 2296-2307, doi:10.1785/0120100075.

Dunham, E. M., Belanger, D., Cong, L., and J.E. Kozdon (2011b), Earthquake ruptures with strongly rate-weakening friction and off-fault plasticity, Part 2: Nonplanar faults, *Bull. Seismol. Soc. Am., 101*(5), 2308-2322, doi:10.1785/0120100076.

Elbanna, A. E., and J. M. Carlson (2014), A two-scale model for sheared fault gouge: Competition between macroscopic disorder and local viscoplasticity, *J. Geophys. Res. Solid Earth, 119*, 4841-4859, doi:10.1002/2014JB011001.

Evans, J. P., and F.M. Chester (1995), Fluid-rock interaction in faults of the San Andreas system: Inferences from San Gabriel fault rock geochemistry and microstructures, *J. Geophys. Res.,* 100(B7), 13007-13020.

Faulkner, D. R., Mitchell, T. M., Behnsen, J., Hirose, T., and T. Shimamoto (2011), Stuck in the mud? Earthquake nucleation and propagation through accretionary forearcs, *Geophys. Res. Lett., 38*(18), L18303, doi: 10.1029/2011GL048552.

French, M. E., Kitajima, H., Chester, J. S., Chester, F. M., and T. Hirose (2014), Displacement and dynamic weakening processes in smectite rich gouge from the Central Deforming Zone of the San Andreas Fault. *J. Geophys. Res., 119*(3), 1777-1802, doi: 10.1002/2013JB010757.

Freund, L. B. (1998), *Dynamic fracture mechanics*. Cambridge University Press.

Fulton, P. M., Brodsky, E. E., Kano, Y., Mori, J., Chester, F., Ishikawa, T., Harris, R. N., Lin, W., Eguchi, N., and S. Toczko (2013), Low coseismic friction on the Tohoku-Oki fault determined from temperature measurements. *Science*, 342(6163), 1214-1217, doi: 10.1126/science.1243641.

Gabriel, A. A., Ampuero, J. P., Dalguer, L. A., and P. M. Mai (2013), Source properties of dynamic rupture pulses with off-fault plasticity. *J. Geophys. Res.,* 118(8), 4117-4126, doi:10.1002/jgrb.50213.

Goldsby, D. L., and T.E. Tullis (2011), Flash heating leads to low frictional strength of crustal rocks at earthquake slip rates. *Science*, 334(6053), 216-218, doi:*10.1126/science.1207902*.

Heaton, T. H. (1990). Evidence for and implications of self-healing pulses of slip in earthquake rupture. *Phys. Earth Planet. Inter., 64*(1), 1-20.

Hubbert, M. K., and W. W. Rubey (1959), Role of fluid pressure in mechanics of overthrust faulting I. Mechanics of fluid-filled porous solids and its application to

overthrust faulting. *Geol. Soc. Am. Bull., 70*(2), 115-166.

Kang, J., and B. Duan (2014), Inelastic response of compliant fault zones to nearby earthquakes in three dimensions, *Tectonophysics*, 612-613: 56-62, doi:10.1016/j.tecto.2013.11.033.

Kitajima, H., Chester, J. S., Chester, F. M., and T. Shimamoto (2010), High-speed friction of disaggregated ultracataclasite in rotary shear: Characterization of frictional heating, mechanical behavior, and microstructure evolution. *J. Geophys. Res.,* 115(B8), doi:10.1029/2009JB007038.

Lachenbruch, A. H., and J.H. Sass (1980), Heat flow and energetics of the San Andreas fault zone. *J. Geophys. Res., (1978–2012)*, *85*(B11), 6185-6222.

Lachenbruch, A. H. (1980), Frictional heating, fluid pressure, and the resistance to fault motion. *J. Geophys. Res., 85*(B11), 6097-6112.

Lapusta and Rice (2003), Low-heat and low-stress fault operation in earthquake models of statically strong but dynamically weak faults, *Eos Trans. AGU*, 84(46) Fall Meet. Suppl., Abstract S51B-02.

Lieou, C. K., Elbanna, A. E., Langer, J. S., and J. M. Carlson (2014), Shear flow of angular grains: Acoustic effects and nonmonotonic rate dependence of volume, *Physical Review E*, *90*(3), 032204.

Liu, Y., and A.M. Rubin, (2010), Role of fault gouge dilatancy on aseismic deformation transients. *J. Geophys. Res.,* 115, B10414, doi:10.1029/2010JB007522.

Ma, S., and D. J. Andrews (2010), Inelastic off-fault response and three dimensional dynamics of earthquake rupture on a strike-slip fault. *J. Geophys. Res.,* 115, B04304, doi:10.1029/2009JB006382.

Ma, S. (2008), A physical model for widespread near-surface and fault zone damage induced by earthquakes, *Geochem. Geophys. Geosyst.*, 9, Q11009, doi:10.1029/2008GC002231.

Marone, C., Raleigh, C. B., and C.H. Scholz (1990), Frictional behavior and constitutive modeling of simulated fault gouge. *J. Geophys. Res.,* 95(B5), 7007-7025.

Morrow, C. A., and J.D. Byerlee (1989), Experimental studies of compaction and dilatancy during frictional sliding on faults containing gouge. *J. Struct. Geol.*, 11(7), 815-825.

Morton, N., Girty, G. H., and T.K. Rockwell (2012), Fault zone architecture of the San Jacinto fault zone in Horse Canyon, southern California: A model for focused

post-seismic fluid flow and heat transfer in the shallow crust. *Earth Planet. Sc. Lett.,* 329, 71-83, doi:10.1016/j.epsl.2012.02.013.

Noda, H., Dunham, E. M., and J. R. Rice (2009), Earthquake ruptures with thermal weakening and the operation of major faults at low overall stress levels. *J. Geophys. Res.,* 114(B7), B07302, doi:10.1029/2008JB006143.

Platt, J. D., Rudnicki, J. W., and J. R. Rice (2014), Stability and localization of rapid shear in fluid-saturated fault gouge: 2. Localized zone width and strength evolution, *J. Geophys. Res., 119*, 4334-4359, doi:10.1002/2013JB010711.

Price, R. A. (1988), The mechanical paradox of large overthrusts, *Geol. Soc. Amer. Bull.*, 100, 1898-1908.

Rempe, M., T. Mitchell, J. Renner, S. Nippress, Y. Ben-Zion, and T. Rockwell (2013), Damage and seismic velocity structure of pulverized rocks near the San Andreas Fault, *J. Geophys. Res. Solid Earth*, 118, 2813–2831, doi:10.1002/jgrb.50184.

Rice, J. R., Sammis, C. G., and R. Parsons (2005), Off-fault secondary failure induced by a dynamic slip pulse. *Bull. Seismol. Soc. Am., 95*(1), 109-134, doi:10.1785/0120030166, 2005.

Rice, J. R., Rudnicki, J. W. and J. D. Platt (2014), Stability and Localization of Rapid Shear in Fluid-Saturated Fault Gouge, 1. Linearized stability analysis, *J. Geophys. Res.*, 119, doi:10.1002/2013JB010710.

Rice, J. R. (2006), Heating and weakening of faults during earthquake slip. *J. Geophys. Res.,* 111(B5), B05311, doi:10.1029/2005JB004006.

Rockwell, T. K., and Y. Ben-Zion (2007), High localization of primary slip zones in large earthquakes from paleoseismic trenches: Observations and implications for earthquake physics, *J. Geophys. Res., 112*, B10304, doi:10.1029/2006JB004764.

Rojas, O., Dunham, E. M., Day, S. M., Dalguer, L. A., and J. E. Castillo (2009), Finite difference modelling of rupture propagation with strong velocity-weakening friction. *Geophys. J. Int.*, *179*(3), 1831-1858, doi: doi:10.1111/j.1365-246X.2009.04387.x.

Roscoe, K. H., Schofield, A., and C. P. Wroth (1958), On the yielding of soils, *Geotechnique*, *8*(1), 22-53.

Rudnicki, J. W., and J. R. Rice (2006), Effective normal stress alteration due to pore pressure changes induced by dynamic slip propagation on a plane between dissimilar materials. *J. Geophys. Res.,* 111(B10), B10308, doi:10.1029/2006JB004396.

Scholz, C. H. (2006), The strength of the San Andreas Fault: A critical analysis, in Earthquakes: Radiated Energy and the Physics of Faulting (eds. R. Ambercrombie, A. McGarr, .G Di Toro and H. Kanamori), American Geophysical Union, Washington, D.C. doi: 10.1029/170GM30.

Scott, D. R., Lockner, D. A., Byerlee, J. D., and C.G. Sammis (1994), Triaxial testing of Lopez fault gouge at 150 MPa mean effective stress. *Pure Appl. Geophys.*, *142*(3-4), 749-775.

Segall, P., Rubin, A. M., Bradley, A. M., and J. R. Rice (2010), Dilatant strengthening as a mechanism for slow slip events. *J. Geophys. Res.*, *115*(B12), B12305, doi:10.1029/2010JB007449.

Segall, P., and J. R. Rice (1995), Dilatancy, compaction, and slip instability of a fluid-infiltrated fault. *J. Geophys. Res., 100*(B11), 22155-22171.

Shi, Z., and S. M. Day (2013), Rupture dynamics and ground motion from 3-D rough-fault simulations, *J. Geophys. Res. Solid Earth, 118*, doi:10.1002/jgrb.50094.

Sibson, R. H. (1973), Interactions between temperature and pore-fluid pressure during earthquake faulting and a mechanism for partial or total stress relief. *Nature*, *243*(126), 66-68.

Sibson, R. H., Robert, F., and K. H. Poulsen (1988), High-angle reverse faults, fluid-pressure cycling, and mesothermal gold-quartz deposits. *Geology*, 16(6), 551-555.

Sibson, R. H. (1975), Generation of pseudotachylyte by ancient seismic faulting. *Geophys. J. Int.*, *43*(3), 775-794.

Sibson, R. H. (2003), Thickness of the seismic slip zone. *Bull. Seismol. Soc. Am., 93*(3), 1169-1178.

Sleep, N. H., and M. L. Blanpied (1992), Creep, compaction and the weak rheology of major faults. *Nature*, 359(6397), 687-692.

Sleep, N. H. (1997), Application of a unified rate and state friction theory to the mechanics of fault zones with strain localization. *J. Geophys. Res.,* 102(B2), 2875-2895.

Sleep, N. H. (2010), Sudden and gradual compaction of shallow brittle porous rocks. *J. Geophys. Res.,* 115(B8), B08210, doi:10.1029/2009JB006719.

Stefanov, Y. P., Chertov, M. A., Aidagulov, G. R., and A.V. Myasnikov (2011), Dynamics of inelastic deformation of porous rocks and formation of localized compaction zones studied by numerical modeling. *J. Mech. Phys. Solids*, 59(11),

2323-2340.

Suppe, J. (2007), Absolute fault and crustal strength from wedge tapers. *Geology*, 35(12), 1127-1130.

Templeton, E. L., and J.R. Rice (2008), Off-fault plasticity and earthquake rupture dynamics: 1. Dry materials or neglect of fluid pressure changes. *J. Geophys. Res.,* 113(B9), B09306, doi:10.1029/2007JB005529.

Townend, J., and M. D. Zoback (2000), How faulting keeps the crust strong. *Geology*, *28*(5), 399-402.

Townend, J., and M. D. Zoback (2004). Regional tectonic stress near the San Andreas fault in central and southern California. *Geophys. Res. Lett.,* 31(15), L15S11, doi:10.1029/2003GL018918.

Townend, J. (2006), What do faults feel? Observational constraints on the stresses acting on seismogenic faults, in Earthquakes: Radiated Energy and the Physics of Faulting, Geophys. Monogr. Ser., vol. 170, edited by R. Abercrombie et al., pp. 313–327, AGU, Washington, D. C.

Ujiie, K., and A. Tsutsumi (2010), High-velocity frictional properties of clay-rich fault gouge in a megasplay fault zone, Nankai subduction zone. *Geophys. Res. Lett.,* 37(24), L24310, doi:10.1029/2010GL046002.

Ujiie, K., Tanaka, H., Saito, T., Tsutsumi, A., Mori, J. J., Kameda, J., Brodsky, E., Chester, F. M., Eguchi, N. and S. Toczko (2013), Low coseismic shear stress on the Tohoku-Oki megathrust determined from laboratory experiments. *Science*, *342*(6163), 1211-1214, doi: 10.1126/science.1243485.

Van der Elst, N. J., Brodsky, E. E., Le Bas, P. Y., and P. A. Johnson (2012), Auto□ acoustic compaction in steady shear flows: Experimental evidence for suppression of shear dilatancy by internal acoustic vibration, *J. Geophys. Res., 117*(B9), *B09314, doi:10.1029/2011JB008897.*

Viesca, R. C., Templeton, E. L., and J. R. Rice (2008), Off-fault plasticity and earthquake rupture dynamics: 2. Effects of fluid saturation. *J. Geophys. Res.,* 113(B9), B09307, doi:10.1029/2007JB005530.

Viesca, R. C., and J. R. Rice (2009), Modeling slope instability as shear rupture propagation in a saturated porous medium, in Submarine Mass Movements and Their Consequences, (eds. D. C. Mosher, R.C. Shipp, L. Moscardelli, J. D. Chaytor, C. D. P. Baxter, H. J. Lee, and R. Urgeles), Springer-Verlag, New York, pp. 215-225, 2010.

Wong, T. F., David, C., and W. Zhu, (1997), The transition from brittle faulting to cataclastic flow in porous sandstones: Mechanical deformation. *J. Geophys. Res., (1978–2012)*, 102(B2), 3009-3025.

Wong, T. F., and P. Baud (2012), The brittle-ductile transition in porous rock: A review. *J. Struct. Geol.*, 44, 25-53.

Xu, S., and Y. Ben-Zion (2013), Numerical and theoretical analyses of in-plane dynamic rupture on a frictional interface and off-fault yielding patterns at different scales. *Geophys. J. Int.*, 193, 304-320, doi: 10.1093/gji/ggs105.

Zheng, G., and J. R. (1998), Conditions under which velocity-weakening friction allows a self-healing versus a cracklike mode of rupture. *Bull. Seismol. Soc. Am.,* 88(6), 1466-1483.

Zoback, M. D., Zoback, M. L., Mount, V. S., Suppe, J., Eaton, J. P., Healy, J. H., Oppenheimer, D., Reasenberg, P., Jones, L., Raleigh, B., Wong, I. G., Scotti, O. and C. Wentworth (1987), New evidence on the state of stress of the San Andreas Fault system. *Science*, 238(4830), 1105-1111.

Table 2.1. Calculation parameters in the baseline case

Density	ρ	2700 kg/m3
P-wave velocity	V_P	6000 m/s
S-wave velocity	V_S	3464 m/s
Gouge width	w	20 cm
Skempton's coefficient	B	0.6
Biot's coefficient	α	0.45
Off- and on-fault normal stresses	$\sigma_{xx} = \sigma_{yy} = \sigma_n$	-126 MPa
Off- and on-fault shear stresses	$\sigma_{xy} = \tau_b$	35 MPa
Direct effect parameter	a	0.016
State variable evolution parameter	b	0.2
State variable evolution distance	L	1.3717×10^{-4} m
Reference friction	f_0	0.7
Reference slip velocity	V_0	1.0 μm/s
Weakened friction coefficient	f_w	0.13
Weakening velocity	V_w	0.17 m/s
Initial state variable	ψ_0	0.4367
Characteristic state-evolution region	R_0	$16\,\Delta x$
Internal friction	$\tan\phi$	0.85
Cohesion	c	0 MPa
Mohr-Coulomb dilatancy angle	θ	$\tan^{-1}(0.5\sin\phi)$
Closeness to cap failure	CF_{CAP}	0.95
Ellipse aspect ratio	a_{CAP} / b_{CAP}	2
Ellipse hardening parameters	h_{S_0}, h_{S_1}, h_η	0.5, 3.0, 0.2
Steady state dilatancy factor	ζ	1.5×10^{-5}
Dilatancy evolution velocity factor	ξ	0.1
Velocity evolution standard deviation	δ	1 cm
Element Size	Δx	1 cm
Time step	Δt	1.25 μs
Calculation time		10 ms

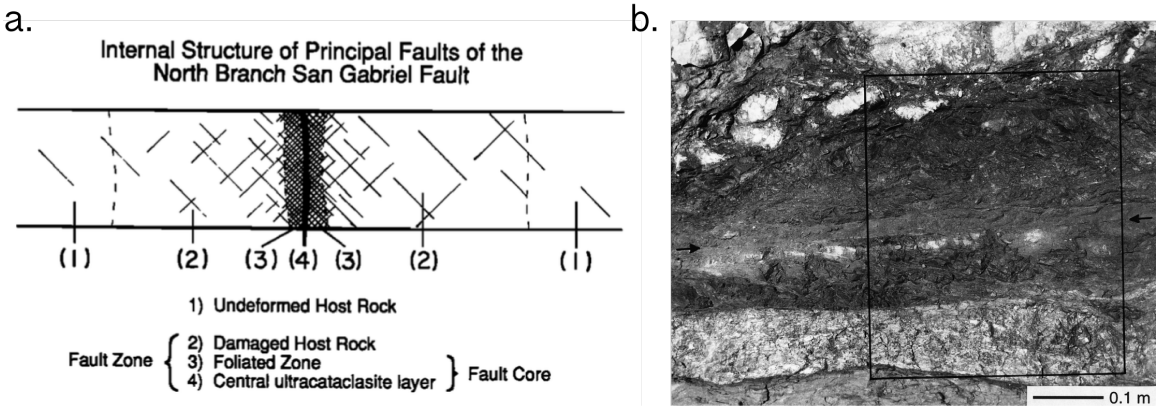

Figure 2.1 (a) Schematic diagram of architecture for the North Branch San Gabriel Fault, representative of mature fault zones (from Chester et al., 1993) and (b) a photo of the ultracataclasite gouge (from Chester and Chester, 1998). Fracture density increases towards the fault core, which consists of a foliated cataclasite and a central layer of ultracataclasite gouge. Slip is highly localized into the gouge and even further on extremely narrow fracture surfaces (marked by black arrows).

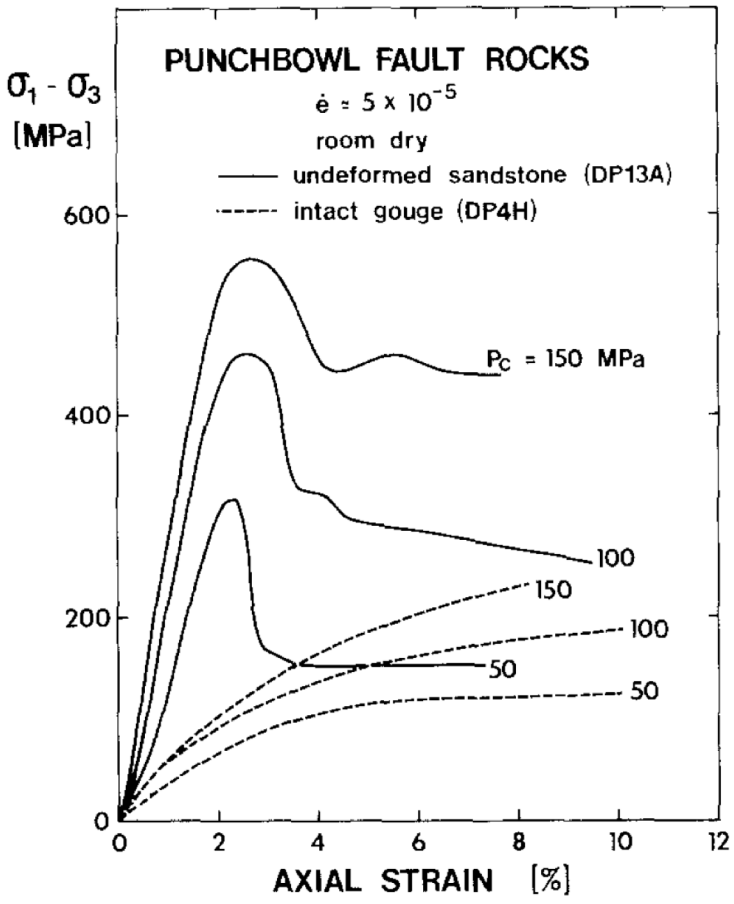

Figure 2.2. Comparison of deformation characteristics in triaxial experiments for rocks from the Punchbowl Fault under different confining pressures (from Chester and Logan, 1986). The sandstone from the damage zone experiences typical brittle failure, while intact gouge compacts during the entire experiment. The strength increase is due to strain hardening. Gouge compaction is an important characteristic that we consider in this study.

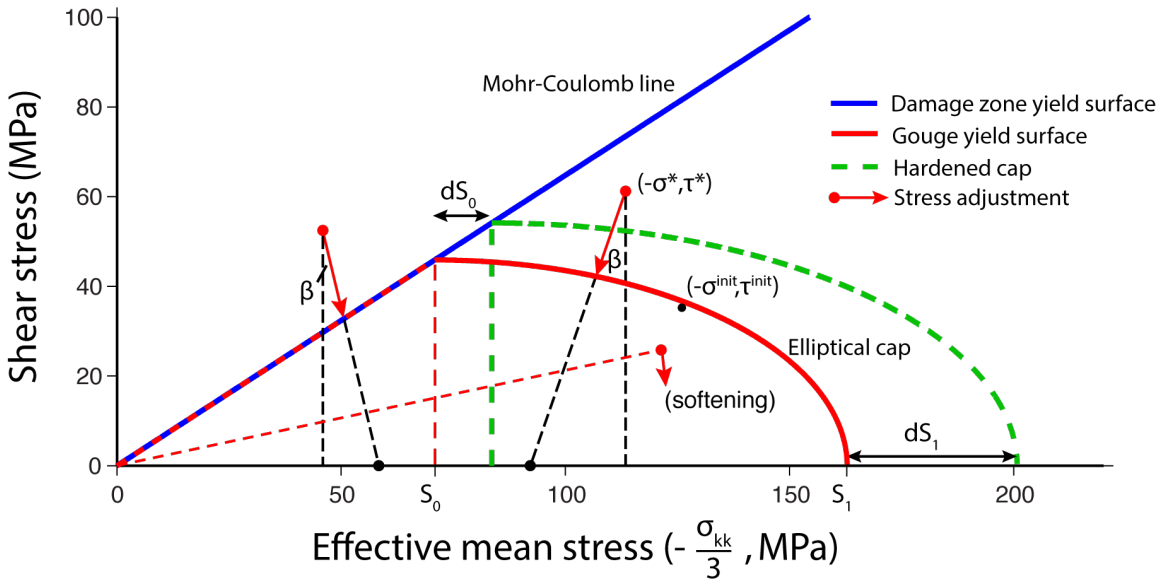

Figure 2.3. A combined Mohr Coulomb – end cap yield criterion is used to model the deformation of fault gouge. Gouge material obeys the Mohr-Coulomb criterion up to a transition pressure (S_0), above which an elliptical end cap defines the material strength. Damage zone material obeys only the Mohr-Coulomb criterion. The two rheologies are identical up to the transition pressure S_0. Red arrows outside the yield surface denote the direction of stress adjustment during plastic flow. The dashed green line shows the hardened yield cap. The red arrow inside the yield surface depicts the stress adjustment from dilatancy evolution (see the text for details). The initial stress is chosen close to the end cap because gouge readily compacts.

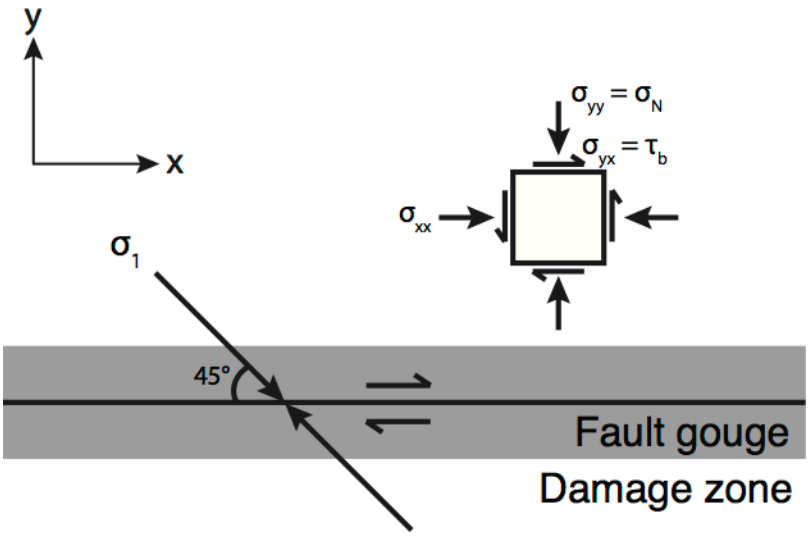

Figure 2.4. Model geometry. A right-lateral strike-slip fault is embedded in a narrow layer of fault gouge, which obeys the combined Mohr Coulomb – end cap yield criteria (Figure 2.3). The surrounding damage zone obeys the Mohr-Coulomb criterion only. A constant dilatancy angle is used in the damage zone, $\theta = \tan^{-1}(0.5\sin\phi)$. Maximum principal stress is oriented at 45° to the fault.

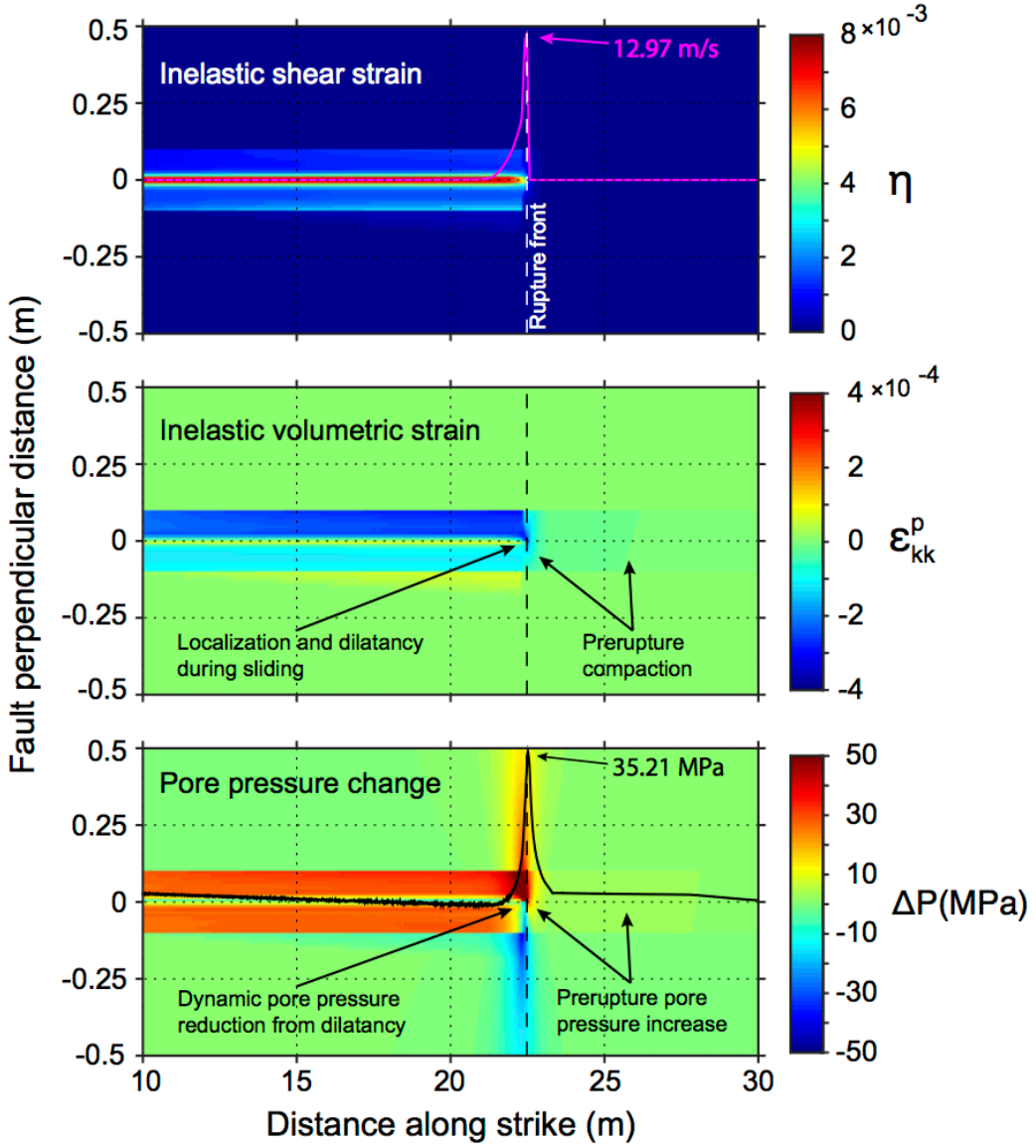

Figure 2.5. Snapshot of inelastic shear strain, inelastic volumetric strain, and pore pressure change is mapped for the gouge end-cap model at 8 ms simulation time. Slip velocity (magenta curves) and on-fault pore pressure change (solid black curves) on the fault are superimposed on the top and bottom figures, respectively. The numbers next to the arrows at the top right of these subplots give the peak values of these curves. The portion shown is a region near the rupture front to the right of the nucleation point (distance along strike in the x axis is in meters from the nucleation point). The white dashed lines mark the location of the rupture front. The combination of the S-wave and the intense shear stress in front of the crack tip cause compaction prior to slip, because the fault gouge is on the verge of shear enhanced compaction. This increases the pore pressure before rupture arrives. When the fault begins sliding, dilatancy evolution begins to take place, and the gouge becomes dilated and pore pressure is reduced. This leads to a narrow zone of dilated, highly strained gouge (see also Figure 6).

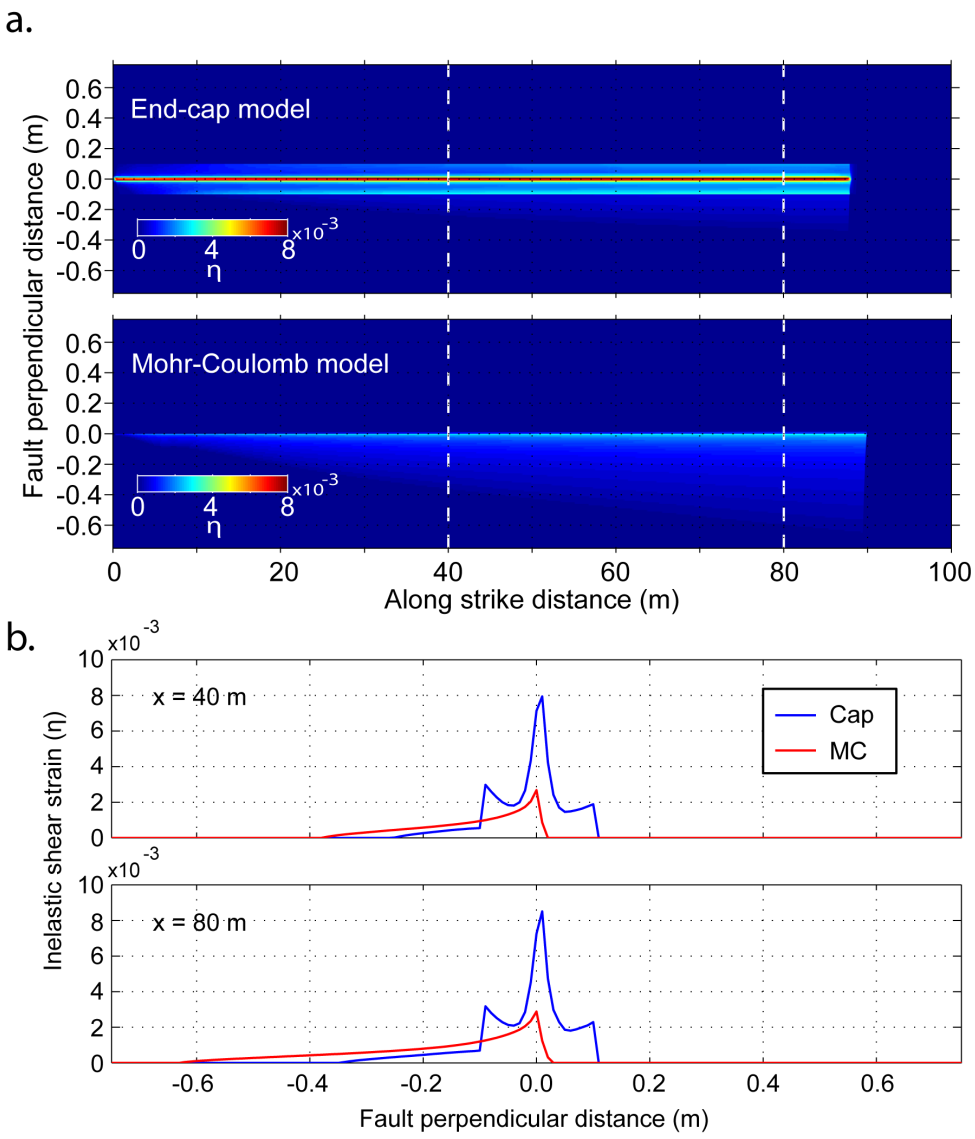

Figure 2.6. (a) Comparison of inelastic shear strain distributions between our end-cap model (top) and a Mohr-Coulomb (MC) model. The MC model shows a typical triangular region of damage, while the end-cap model has most deformation occurring in the gouge with highly localized failure near the fault. (b) Plots of inelastic shear strain are shown in cross sections at two distances along the fault strike. The MC case has more damage outside of the gouge but far less damage inside of the gouge zone.

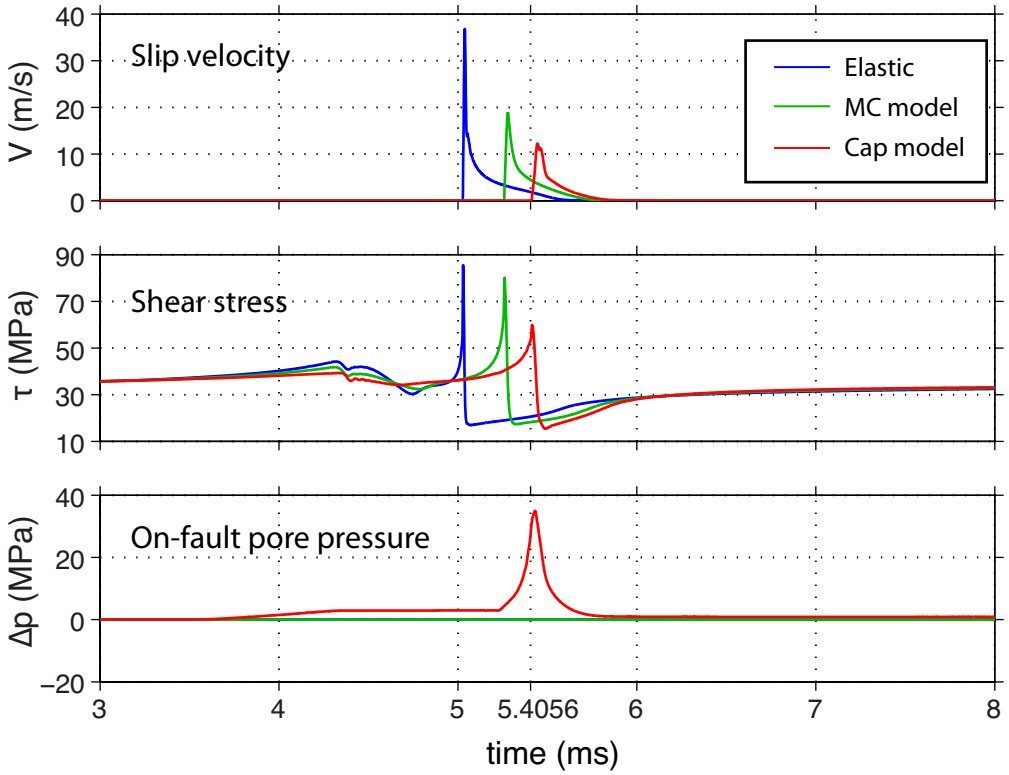

Figure 2.7. Time histories at x = 15 m for an elastic case, a case with only the Mohr-Coulomb criterion, and a case with the Mohr Coulomb – end cap model. All three cases are identical except for the yield surface used (or lack of yield surface for the elastic case) and the on-fault pore pressure calculation. The dashed line at 5.4056 ms marks the rupture front for the end-cap case. With the cap model, on-fault pore pressure increase due to pre-rupture compaction lowers static friction and strength drop, resulting a smaller slip velocity. Pore pressure decrease and dilatancy strengthening can also be clearly seen.

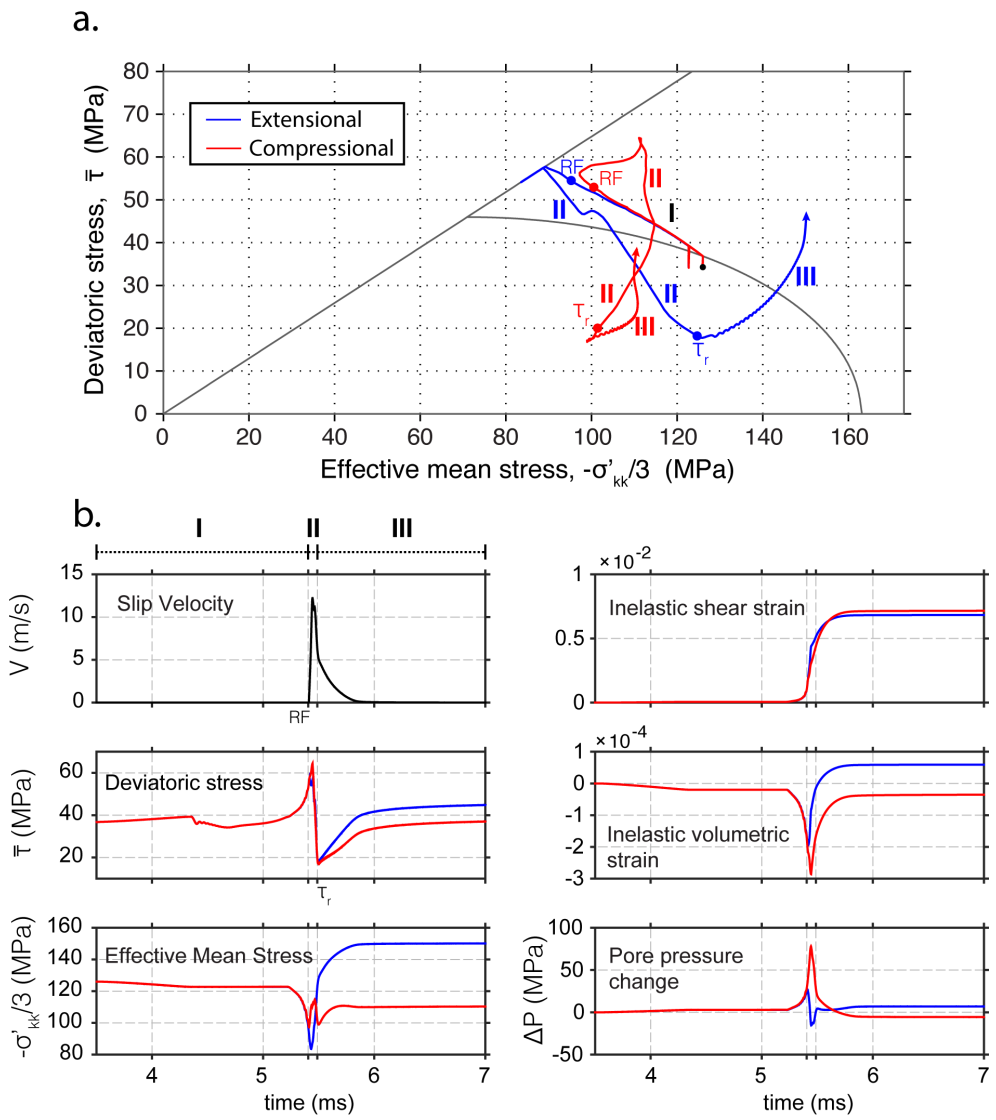

Figure 2.8. a) Stress paths at two points (x = 15.5 cm) on either of the fault, located at half the element size away from the fault plane. Three stages of deformation can be identified, marked as I, II, and III on stress paths and time histories. The black dot marks the initial stress state. The red and blue dots marked as RF are the stress states at the rupture front arrival, which mark the start of stage II. The red and blue dots marked τ_r show the stress state at the time when shear stress on the fault reaches its minimum value (the residual shear stress). This marks the start of stage III. b) Relevant time histories are plotted at the same points. The three stages are noted as well.

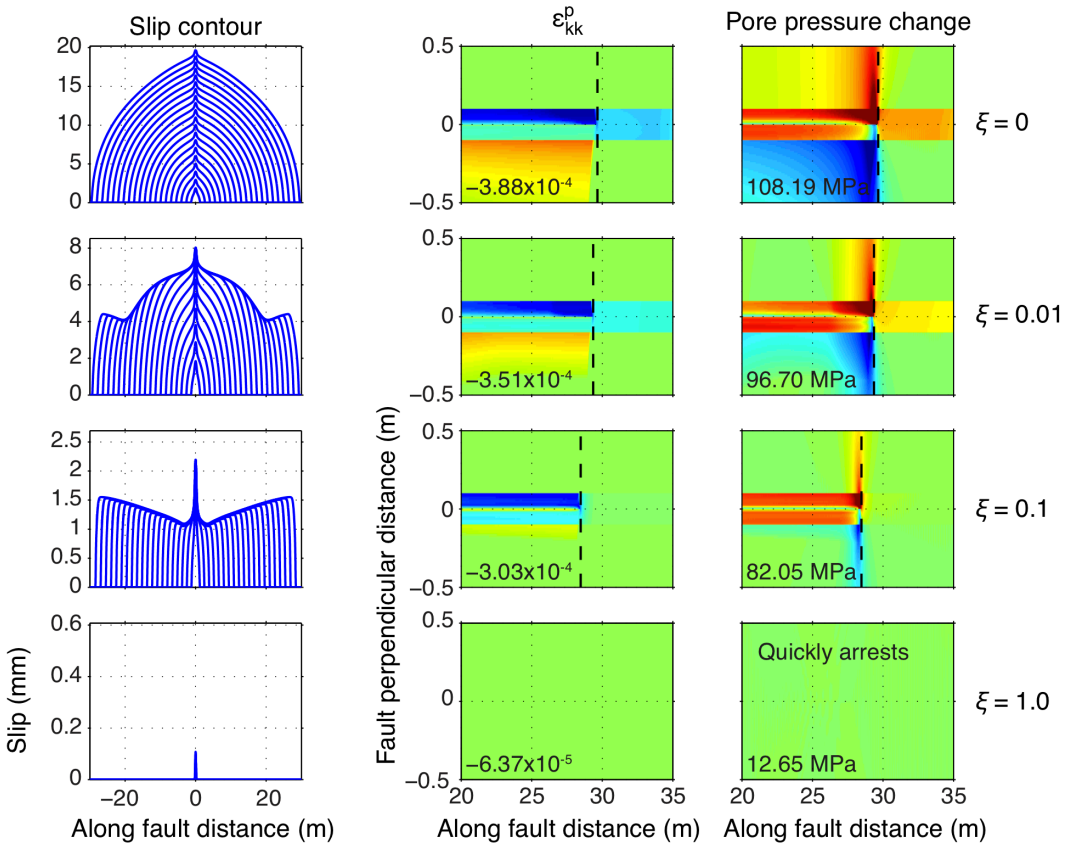

Figure 2.9. Comparison of results for cases with varying dilatancy parameter ξ. Slip contours every 0.5 ms (left column), snapshots of inelastic volumetric strain at 8 ms (middle column), and pore pressure distribution at 8 ms (right column) are illustrated. The color scales are the same as in Figure 5. The number in each panel denotes the peak value in the medium. When $\xi = 0$, the gouge does not experience dilatancy evolution during sliding, so the pore pressure remains relatively high. The narrow zone that appears to have lower pore pressure is due to elastic reloading (more compression) after experiencing inelastic failure [Templeton and Rice, 2008]. This causes the fault to remain weak, and fault rupture is crack-like. As ξ increases, dilatancy during sliding becomes strong and begins to make rupture more pulse-like, until it does not allow rupture at large values.

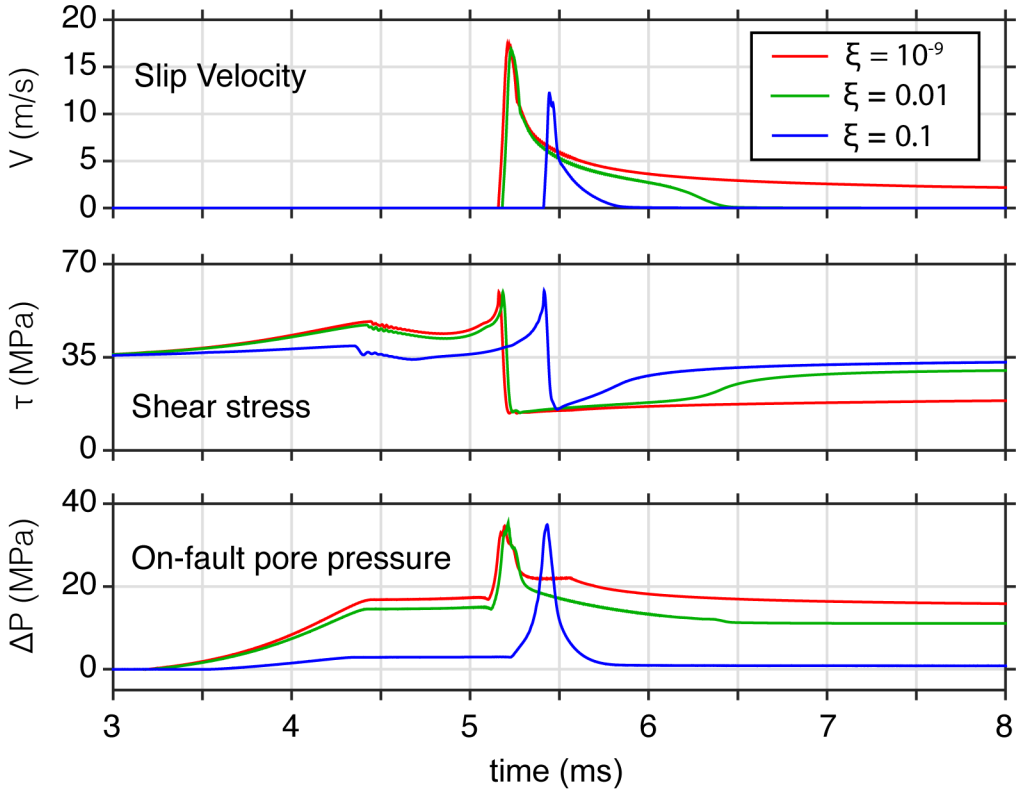

Figure 2.10. Time histories of slip velocity, shear stress, and on-fault pore pressure at x = 15 m are plotted for the three cases shown in Figure 2.9. For the case with $\xi = 0.1$, gouge dilatancy causes a reduction in pore pressure after slip initiates. This restrengthens the fault and causes a pulse-like rupture. The case with $\xi = 10^{-9}$ experiences negligible dilatancy, which keeps the pore pressure high and the fault weak. This leads to a crack-like rupture. The case with $\xi = 0.01$ is an intermediate case, where the pulse with is longer than with $\xi = 0.1$ but eventually arrests.

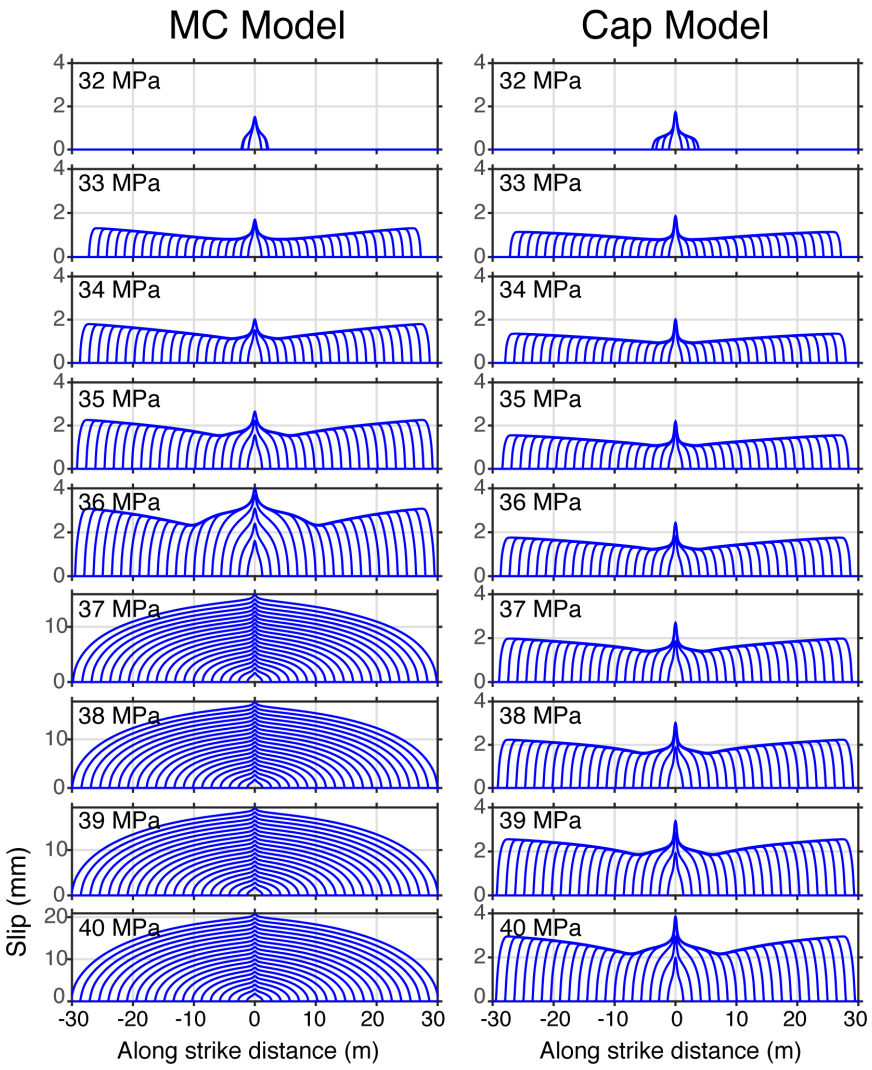

Figure 2.11. Comparisons of slip contours in Mohr-Coulomb and end-cap cases for a range of background stress levels. Undrained dilatancy allows pulselike ruptures at higher stress levels where Mohr-Coulomb cases show cracklike ruptures. At low background stress levels rupture does not propagate in both cases. This is, however, an artifact of rupture nucleation in the end-cap simulation. Undrained dilatancy starts immediately when fault is slipping in the nucleation zone, which prevents rupture from propagating. The weakening from our mechanism allows rupture nucleation at lower background stress levels than those in the elastic case if dilatancy in the nucleation is removed.

Chapter 3

Undrained Gouge Plasticity and Rupture Dynamics of Rough Faults

Abstract

Observations of faults as geometrically complex surfaces have led to recent modeling studies of dynamic rupture on rough faults. Fault profiles are usually modeled as fractal surfaces. Geometrical irregularities lead to spatially varying fault tractions, and can have a significant effect on rupture propagation, leading to observations of rupture arrest, supershear rupture, fluctuations in rupture velocity, and high frequency ground motions. Current rough fault models are lacking physical considerations that should not be ignored in future models. These include the consideration of a heterogeneous off-fault stress state generated by previous fault slip, the allowance of inelastic volumetric strains due to large changes in mean stress at fault bends, and the effect of dynamic pore pressure changes on fault strength. Here, we consider all three of these effects on rough fault rupture propagation. We generate the heterogeneous off-fault stress field by first kinematically applying uniform slip to the fault. This causes more compressive stresses at restraining bends and more extensional stresses at releasing bends. The model contains fault gouge constitutive behavior as formulated in Hirakawa and Ma [2016], which consists of a combined Mohr-Coulomb (MC) and end-cap surface and allows compaction and dilatancy with undrained pore pressure changes. The heterogeneous initial stress state can cause the off-fault material to be close to MC failure, close to end-cap failure, or

relatively far from both, in the middle of the elastic regime. Compaction causes at restraining bends causes large pore pressure increase and allows rupture to propagate through segments that arrest rupture in the case with purely MC failure. Strengthening by undrained dilatancy at releasing bends limits supershear rupture from the MC case. Slip distributions become much more uniform than in the MC case due to the stabilizing tendency of the pore fluids. The tendency for ruptures to accelerate and decelerate at releasing and restraining bends respectively is reversed; however, extreme closeness to failure and large amounts of inelastic strain cause rupture velocity to fluctuate much more than the MC case.

3.1. Introduction

Crustal faults are geometrically complex at a variety of length scales, and are often modeled as self-similar (fractal) surfaces [e.g. Brown and Scholz, 1985; Aviles et al., 1987; Okubo and Aki, 1987; Power and Tullis, 1991; Renard et al., 2006; Candela et al., 2009; Candela et al., 2012]. Early models of earthquake physics considered rupture on a flat, planar fault. However, more recent studies have found that it is increasingly necessary to consider geometrical complexities of fault surfaces, and their influence on rupture dynamics. Studies such as this (commonly referred to as 'rough faults' in the literature) have become common and have recently begun to be employed in providing more realistic models of rupture dynamics and earthquake ground motions.

Bends in a fault trace cause a homogeneous regional stress field to be resolved onto the fault plane as locally heterogeneous tractions. Locations where stresses become more compressional or tensional are referred to as restraining and releasing bends respectively. These heterogeneous initial tractions have a significant effect on dynamic earthquake ruptures when compared with ruptures on a flat fault, as the initial friction ratio ($\frac{\tau}{\sigma_N}$, where τ is shear stress and σ_N is normal stress) becomes closer or further from the static friction level depending on the type of bend. Dunham et al. [2011b] provided a pioneering work on rough fault rupture dynamics with a 2D model and showed that fault roughness causes the rupture front to accelerate and decelerate. This process gives rise to higher-frequency seismic radiation and a heterogeneous final slip distribution on the fault in comparison with a flat fault model. Shi and Day [2013] extended this work to 3D to further investigate the influence of roughness on fault

rupture. They also found that ground motions resulting from such rough fault models seem to match the mean and variability of recorded ground motions in a wide period range (0.1 – 3 s), and increased the power of the higher frequency portion of the ground motion spectrum.

From a compilation of over a thousand realizations of dynamic rupture on rough faults, Fang and Dunham [2013] suggested fault roughness as a means of introducing an additional resistance to slip ("roughness drag"). This provides a simple explanation for observations that mature faults likely operate at low shear stresses while immature faults operate at high stresses, and provided a physical basis by which dynamically propagating ruptures arrest at restraining bends. Bruhat et al. [2016] used this same suite of models and showed that at higher background stresses, fault roughness can lead to highly complex rupture patterns that include supershear rupture propagation, brief supershear to sub-Rayleigh transients, rupture jumps, and rerupture of previously ruptured fault segments.

Though these early works spearheaded the study of rough fault rupture dynamics and have contributed greatly to our understanding of more realistic earthquake processes, there are a few notable oversimplifications that have been made. They generally do not take into account complex heterogeneous stress states that arise in the off-fault medium as a result of the fault roughness, they use only simple plastic rheologies and lack more detailed deformational behavior during inelastic failure of the fault zone rock, and they do not consider the influence of dynamic pore pressure variations on fault strength. In the current study, we aim to provide new insight into rough fault rupture dynamics by considering these overlooked aspects.

Current rough fault models require that the off-fault material experience inelastic failure at some yield stress. This is generally prescribed as a means of limiting extreme stress concentrations or tensile stresses. A simple brittle-shear failure law, typically the Drucker-Prager yield criterion, enforces this. However, a more precise description of the relationship between rough fault rupture dynamics and inelastic off-fault deformations is warranted.

Most faults are surrounded by a layer of fault gouge: a highly deformed, extremely fine-graind material, which forms as a result of repeated attritition and comminution of fault zone rocks [Chester et al., 1993]. Gouge layers typically have a thickness on the centimeters to tens of centimeters scale. Gouge has been found to readily compact and deform in a ductile manner in laboratory experiments [Chester and Logan, 1986; Scott et al., 1994]. This is in stark contrast to the typical elastic-brittle behavior of rocks from the damage zone, which can be described well by the Mohr-Coulomb or Drucker-Prager yield criteria. Drawing on this observation, Hirakawa and Ma [2016] (also Chapter 2 in this dissertation) developed a continuum model for gouge deformation, where gouge readily compacts and raises pore pressure when in an undrained state. This was done by the inclusion of an elliptical end-cap to the traditional Mohr-Coulomb surface. This combined yield surface has been shown to fit the strength of porous rocks from laboratory experiments [Wong et al., 1997]. Large shear stress concentrations carried by the rupture front causes shear-enhanced compaction ahead of the rupture, which increases pore pressure and preweakens the fault prior to rupture. This results in a dynamic reduction in static strength, an aspect that represents an advantage over other dynamic weakening mechanisms that require slip to initiate. This model revealed the

complex but important relationship between inelastic failure, pore pressure, and rupture dynamics.

When considering complex yielding behavior, the initial stress state is of extreme importance. Current modeling studies have typically assumed spatially uniform off-fault prestresses. This allows for the initial conditions to be easily defined by a single stress tensor throughout the whole volume and requires only that background stresses are resolved as tractions onto the varying fault strike. However, it must be acknowledged that coseismic, postseismic, and interseismic slip on faults with geometric irregularities can significantly alter the off-fault stress field, with the possibility of severe concentrations of stress change near the sharpest geometrical features. In other words, it may not be sufficient to neglect the slip history of a fault. The consequence of this spatially varying stress state is that rock in certain locations will be situated closer to failure than in the average regional stress field; i.e., they may be subjected to higher Coulomb stresses.

The fault step over problem is very similar to the rough fault or bending fault problems. Segall and Pollard [1980] obtained a solution for the static stress field due to slip on two echelon cracks. Their results implied that secondary fractures might be more prevalent in extensional step overs, where the mean stress is greatly reduced. Extensional fractures that develop there may allow possible linkage through the two echelon fault segments and allow slip to be transmitted through the step. The opposite is true of compressional step overs, where the compressional stress is such that the stress path is taken further from the failure, and thus through going slip may be impeded.

Sibson [1986] describes geologic observations that suggest this quasi-static behavior may actually be reversed dynamically, where extensional fault step overs may

actually be greater impediments to transmission of slip than compressional step overs. Extreme tensile stress states may cause opening mode fractures, and cause a severe reduction in pore pressure and an increase effective mean stress. This leads to the development of a suctional force, which strengthens the fault system, and prohibits through going rupture. In compressional step overs, the increase in total mean stress increases the pore pressure, and causes the fault system to be weakened. Harris and Day [1993] verified this effect with a dynamic rupture model, by showing that in comparison with a dry case, the presence of undrained pore fluids could actually inhibit ruptures from jumping extensional step overs. However, they used only an elastic model and did not require the opening of extensional fractures as Sibson [1986] suggested. The mechanics of fault step overs are analogous to fault bends; since faults are self-similar, the same behavior should be present at all length scales and thus at the short-wavelength bends of rough faults.

Here, we incorporate a heterogeneous initial off-fault stress state, the plastic rheology of fault gouge as formulated by Hirakawa and Ma [2016], and dynamic pore pressure changes into a dynamic rupture model on a self-similar rough fault. We find that in comparison with a reference case using only the Mohr-Coulomb yield criterion and no pore pressure changes, our model leads to final slip distribution is more homogeneous, longer extent of rupture, and a reversal in the correlation between rupture velocity and fault slope. Overall, this model demonstrates that the undrained deformation of fault gouge has a stabilizing effect on rough fault rupture dynamics.

3.2. Model

We use the method described by Shi and Day [2013] to generate a 2D self-similar

rough fault profile. A set of complex numbers is randomly generated where the real and imaginary parts are independent normal variables. The complex numbers are then multiplied by a power law function. The resulting random set of complex numbers corresponds to wavenumber representation of the self-similar rough fault. A low-pass filter is applied to remove short wavelength contributions to the rough fault, such that there are 30 grid points per minimum wavelength. The rough fault profile itself is obtained by applying the inverse Fourier transform to this array of complex numbers. The particular rough fault profile we use here was generated using an amplitude-to-wavelength ratio of $\alpha = 0.01$ (Figure 1), which represents a relatively high roughness. See Dunham et al. [2011b] or Shi and Day [2013] for a definition of α.

As the rough fault profiles generated by this method are random, simply changing the seed of the random number generator can lead to an infinite amount of fault realizations. By doing this, some authors have shown that by using many different fault profiles in dynamic rupture simulations, statistical descriptions of rupture characteristics will emerge for certain sets of rough fault parameters [Fang and Dunham, 2013; Trugman and Dunham, 2014; Bruhat et al., 2016]. In this study, we simply choose one rough fault profile that exhibited characteristics seen in previous studies, and use this for all simulations. A thorough test of several different rough fault profiles is not necessary here as we are only seeking to investigate general qualitative rupture characteristics. Similarly, we only use one roughness, α, since the main systematic effect of increasing or decreasing α is qualitatively similar to decreasing or increasing background shear stress respectively.

In this model, off-fault material has a poroelastoplastic response. We consider the

fault plane to be surrounded by a layer of fault gouge. Since gouge readily compacts in laboratory experiments, a yield criterion other than the commonly employed Mohr-Coulomb or Drucker-Prager criteria are required. We model inelastic behavior of fault gouge with the plastic rheology developed by Hirakawa and Ma [2016]. We will briefly summarize that model here.

The yield criterion is a combined surface, which consists of the Mohr-Coulomb yield criterion at low stresses, and an elliptical end-cap at stresses above a certain mean stress, S_0. The mathematical expression for the surface is

$$\begin{aligned} &\bar{\tau} = c\cos\phi - \left(\frac{\sigma_{kk}}{3} + P\right)\sin\phi, \quad -\left(\frac{\sigma_{kk}}{3} + P\right) \le S_0 \\ &\left(\frac{-\frac{\sigma_{kk}}{3} - P - S_0}{a_{CAP}}\right)^2 + \left(\frac{\bar{\tau}}{b_{CAP}}\right)^2 = 1, \quad -\left(\frac{\sigma_{kk}}{3} + P\right) \ge S_0 \end{aligned} \tag{1}$$

In the simulation, stresses are first updated elastically. If they violate the yield condition, they need to be adjusted back to the yield surface. We use a non-associated flow rule to adjust the temporary elastically updated stresses. The direction of the stress adjustment back to the yield surface is given by the line connecting the temporary elastically updated stress, (where is the stress tensor and the superscript * denotes the elastically updated temporary stress) and a point on the horizontal axis halfway between the temporary elastically updated effective mean stress and the center of the ellipse, S_0 (Figure 2). As described Hirakawa and Ma [2016], this is an ad hoc consideration, as we are not aware of well-documented plastic flow behavior of fault gouge. In laboratory experiments, porous rocks behave differently under certain stress

regimes. At low confining stresses, failure occurs in a brittle manner and is accompanied by dilatancy and strain softening. At higher confining stresses, shear strength decreases with pressure, and compaction and strain hardening accompany failure. At intermediate stresses, strength is at a maximum, and inelastic volumetric strain is at a minimum. Note that our plastic flow behavior qualitatively reproduces this behavior, where failure on the Mohr-Coulomb part of the yield surface leads to dilatancy, failure at or near the mean stress S_0 requires the highest shear stresses and is accompanied by close to zero volumetric strain, and failure on the yield cap leads to compaction. Lastly, strain hardening during compaction is represented by cap expansion. See Hirakawa and Ma [2016] for details of this implementation.

In Hirakawa and Ma [2016], the selection of the elliptical cap parameters was based on the initial stress state. This was relatively simple in that model since the flat fault model contained a homogeneous initial stress state. However, in this model, we wish to consider a heterogeneous initial stress state due to slip on the rough fault. We use a static finite element method to calculate the stress change due to uniform slip on the fault assuming elastic response. Slip is prescribed kinematically as a displacement boundary condition on the fault; tractions are continuous across the fault. The resulting stress field represents the static stress perturbation due to past earthquakes and interseismic slip, and serves as an initial condition for the dynamic rupture model. The on-fault stress field that arises from this produces a further complication on the initial conditions, thus we neglect this contribution.

The perturbed stress state from the static stress calculation is a result of kinematically imposed fault slip that can have arbitrary amplitude. During the static stress

perturbation calculation, stresses are linearly elastic; no yielding is considered. However, when added to the background stresses in the dynamic rupture model, the resulting perturbed stresses may be in violation of the yield surface (equation 1). Due to the assumption of linear elasticity in the static stress calculation, these stresses can be scaled by a constant factor, which is equivalent to changing the amount of input slip into the static stress calculation.

The total initial stress tensor is given by

$$\sigma_{ij} = \sigma_{ij}^0 + Ad\sigma_{ij}^{pert} \tag{2}$$

where σ_{ij}^0 is the unperturbed background stress ($\sigma_{xx}^0 = \sigma_{yy}^0 = -126$ in all simulations, $\sigma_{xy}^0 = \tau_b$ varies and is referred to as the background stress in Section 3), $d\sigma_{ij}^{pert}$ is the stress perturbation obtained from the static calculation, and A is a scalar we wish to use to ensure the perturbed stress state is not in violation of the yield surface.

The location of the end-cap is adjustable, as we show in a following paragraph, however the location of the Mohr-Coulomb line is constant (we use a constant internal friction and zero cohesion everywhere in the medium). Thus, we use the Mohr-Coulomb line as a limiting factor for scaling the elastic stress perturbation. We choose to scale the stress perturbations so that when added to the background stress, the stress at the location with the maximum Coulomb stress (*MCS*; we define this location as X^{MCS}) has a closeness-to-failure on the Mohr-Coulomb line of $CF_{MC} = 0.90$ where

$$CF_{MC}(X^{MCS}) = \left(-\sigma_m(X^{MCS})\sin(\phi) + c\cos(\phi)\right)^{-1} \bar{\tau}(X^{MCS}) \ . \tag{3}$$

This follows the definition of CF defined by Templeton and Rice [2008]. The mean stress at this location after adding the stress perturbation is

$$\sigma_m(X^{MCS}) = \sigma_m^0 + Ad\sigma_m^{pert}(X^{MCS}) = \left(\frac{\sigma_{xx}^0 + \sigma_{yy}^0}{2}\right) + A\left(\frac{d\sigma_{xx}^{pert}(X^{MCS}) + d\sigma_{yy}^{pert}(X^{MCS})}{2}\right)$$

(4)

The second invariant of the deviatoric stress tensor at this location is then given by

$$\bar{\tau}(X^{MCS}) = \left[\left(\sigma_{xy}^0 + Ad\sigma_{xy}^{pert}(X^{MCS})\right)^2 + \left(0.5\left[\sigma_{xx}^0 - \sigma_{yy}^0 + Ad\sigma_{xx}^{pert}(X^{MCS}) - Ad\sigma_{yy}^{pert}(X^{MCS})\right]\right)^2\right]^{0.5}$$

(5)

Setting $CF_{MC} = 0.90$ and combining equations 3, 4, and 5, we solve the resulting expression for A and scale the stress tensor throughout the entire domain by this value. A portion of the resulting stress field for one case is shown in Figure 3. Each point is plotted in stress space in Figure 4 with gray dots. The stress point $\left(\sigma_m(X^{MCS}), \bar{\tau}(X^{MCS})\right)$ for one particular case is shown by the green dot on Figure 4b.

In Hirakawa and Ma [2016], the flat fault used allowed the assumption of a homogeneous stress state in the medium. The end-cap parameters were actually defined by the stress state's initial closeness-to-cap failure

$$CF_{CAP} = b_{CAP}^{-1}\left[1 - \left(\frac{-\frac{\sigma_{kk}^{init}}{3} - P - S_0}{a_{CAP}}\right)^2\right]^{-0.5} \bar{\tau}^{init} \qquad (6)$$

where the superscript on the stresses indicates that these are initial values. Thus, the cap parameters were spatially homogeneous as well. The introduction of a heterogeneous initial stress state leads to a spatially variable set of cap parameters. Actual values for the parameters in the elliptical end-cap expression are not well known. The determination of

these parameters from setting the value for CF_{CAP} is done to illustrate the condition that gouge is initially very close to failure. In this study, the assumption is that the location and size of the end-cap is representative of the stressing history of the gouge, rather than any real material properties.

We seek the condition where locations with high relative mean stresses are close to cap failure, while locations with low relative mean stresses are far from cap failure. To obtain this, the following adjustment for S_0^{pert} based on the initial stress state is applied

$$S_0^{pert} = S_0^0 + \kappa\left(\sigma_m^0 - \sigma_m\right) \tag{7}$$

where σ_m^0 is the background (unperturbed) mean stress, S_0^0 is the unperturbed value for S_0 calculated with σ_m^0 in equation 6, and κ is a chosen parameter. For all cases shown here, we use $\kappa = 1$.

Figure 4 illustrates a few examples of the resulting yield caps. The gray dots represent all stress points after adding the static stress perturbation field. For the reference stress (the unperturbed stress), we set CF_{CAP} = 0.70, and S_0^0 is calculated from equation 6 (Figure 4a). At mean stresses lower than σ_m^0, S_0 obtains a higher value (Figure 4b). This means that the end-cap is moved away from current stress point, and the current stress point is likely much closer to the Mohr-Coulomb line than the cap. At mean stresses higher than σ_m^0, S_0 is moved to a lower value and the stress point becomes closer to cap failure than in the initial state (Figure 4c). For the point shown in Figure 4c, CF_{CAP} is around 0.92. However, notice that if this method is used for even moderately high values of mean stress, the stress point quickly finds itself outside of the end-cap, which

corresponds to an unrealistic initial violation of the elastic condition (Figure 4d). To avoid this situation, we set a maximum $CF_{CAP} = 0.95$. If $CF_{CAP} > 0.95$ (note that it will be > 1 if it is outside the cap), we reject the value of S_0 calculated by equation 7 and set a new value of S_0 for $CF_{CAP} = 0.95$ by using equation 6 (Figure 4d).

Pore pressure in the medium is affected by a combination of the elastic stresses and inelastic volumetric strain [Viesca et al., 2008]. Pore pressure change has an important effect on rock strength (for example, see equation 1). Pore pressure can be changed by very large amounts due to stress and inelastic strain concentrations at geometric irregularities on the rough fault. Calculation of pore pressure change in the medium was shown in Hirakawa and Ma [2016], and consists of both elastic and inelastic contributions.

We also model gouge dilatancy during sliding, which occurs after the stress state has fallen below the yield surface. We use the formulation of Hirakawa and Ma [2016], which was adapted from that of Segall and Rice [1995] to model porosity evolution. See equations 13 – 15 in Hirakawa and Ma [2016]. Dilatancy evolution corresponds to an increment in inelastic volumetric strain, and thus has the effect that it reduces the pore pressure. Hirakawa and Ma [2016] showed that this was able to restrengthen the fault during sliding, giving rise to pulse-like ruptures.

We model dynamic rupture on the rough 2D right-lateral strike slip fault (Figure 1). The fault is embedded in a 20 cm thick layer of fault gouge, which obeys the combined yield criterion described previously (Figure 2). The total fault length is 60 meters; the rupture is nucleated in the middle of the fault so that it propagates for 30

meters in each direction. A velocity strengthening region begins at +/- 25 meters from the hypocenter in order to arrest rupture at the fault boundary. Elastic material properties are homogeneous, where P-wave velocity, S-wave velocity, and density are V_P = 6000 m/s, V_S = 3464 m/s, and ρ = 2670 kg/m^3, respectively. An element size of 1 cm is used in all the simulations to ensure a good resolution of the gouge layer.

We use rate-and-state friction with strong velocity weakening, which mimics flash heating. The implementation and parameters used are exactly the same as in Hirakawa and Ma [2016], which closely followed the method outlined by Dunham et al. [2011a] [see also [see also Rice, 2006; Noda et al., 2009; Rojas et al., 2009; and Shi and Day, 2013]. This formulation has the requirement of an initial background velocity. We set this to be constant and use it to calculate the initial state variable. However, note that the initial state variable varies spatially, since its expression includes fault tractions, which change with the rough fault's strike (see for example equation 18 in Hirakawa and Ma [2016]).

A calculation of the pore pressure on the fault is required. We assume that on-fault pore pressure is the average of the pore pressure on both sides of the fault. The true pore pressure on the fault should be a weighted average of these, where the weights depend on the permeability and storage coefficient of the rock [Rudnicki and Rice, 2006; Dunham and Rice, 2008]. Our simple average assumes that these hydraulic parameters are initially the same and do not change with inelastic strain; however, this assumption should be refined in future models as permeability and storage coefficient can be significantly effected by inelastic strain [Zhu et al., 2007; Viesca and Rice, 2009].

Our rupture nucleation procedure is identical to the one used in Hirakawa and Ma

[2016]. In that study, the flat fault allows nucleation at an arbitrary location. However, here we require nucleation at a point that will ensure initiation of rupture propagation. If the nucleation is located near an unfavorably oriented segment, rupture will lose momentum early in the simulation and will quickly arrest. We find a location that has a high initial friction ($\frac{\tau}{\sigma_N}$) over a wide stretch, so that rupture is allowed to propagate initially without obstruction from unfavorably oriented segments (Fang and Dunham [2013] used a similar method for finding the nucleation location). At this location, an instantaneous Gaussian perturbation in shear stress is applied. The standard deviation of the Gaussian function is the characteristic extent of the state-evolution region R_0 and the amplitude is such that the sum of the peak perturbation and the background stress equals $0.7\sigma_N$ at the peak of the Gaussian.

3.3. Results

Figure 5 shows inelastic shear strain (top), inelastic volumetric strain (middle), and pore pressure change off the fault (bottom) in a segment between x = 0 – 20 meters. The total rupture length is much longer than this segment (between x = -30 – 30 meters). The narrow 20 cm layer of high inelastic shear strain clearly outlines the boundary of the gouge layer. Inelastic strain outside of this layer indicates failure in the damage zone, and qualitatively resembles the results from other studies that have modeled plasticity near rough faults [e.g. Dunham et al., 2011b].

The bends in the fault clearly affect concentrations of shear strain in the fault gouge. This particular segment of the fault contains broad releasing and restraining bends (for example the large restraining bend from x = ~10 – 14 m, and the large releasing bend

from the nucleation point to x = ~ 4 m); however, the distribution of inelastic strain shows that the shortest roughness wavelengths dominate the stress field. Gouge in restraining bends clearly experiences a large amount of compaction (indicated by negative ε_{kk}^{p} in Figure 5). A notable example can be seen at x = ~7 m. This leads to large increases in pore pressure at these restraining bends. At releasing bends, a large amount of dilatancy occurs in the fault gouge (indicated by positive ε_{kk}^{p}), which greatly reduces the pore pressure. Notable examples of this can be seen at x = ~3 m and x = ~18 m.

Fang and Dunham [2013] showed that when rupture propagates onto a fault segment with unfavorable orientation for rupture propagation (i.e. at a restraining bend), the low initial stress ratio (τ / σ_N) renders continued rupture propagation more difficult. They showed that rupture tended to arrest at restraining bends. However, they did not consider the effects of dynamic pore pressure changes on fault strength. In order to make a comparison with our model, we ran models with purely Mohr-Coulomb plasticity off the fault, and with no dynamic pore pressure change (i.e. Skempton's coefficient is zero). This is similar to the condition in most current dynamic rupture models on rough faults, such as that of Fang and Dunham [2013].

The findings of our Mohr-Coulomb models are similar to theirs: at low background stresses, rupture quickly arrests at restraining bends. This is seen in Figure 6, which shows slip contours for a number of cases with varying intial background shear stress, τ_b. The contour interval is 0.5 ms. Rupture propagation distance decreases at low background stresses; rupture arrest occurs at restraining bends in these cases. For example, in the case with τ_b = 40 MPa, the rupture arrested at the restraining bend

centered around x = ~-10 m in the leftward propagating direction, and x = ~10 in the rightward propagating direction (Figure 1). Rupture arrested before reaching the fault boundary for all Mohr-Coulomb cases below 45 MPa.

When the undrained gouge layer is included, the large variations in pore pressure dramatically affect the fault strength when resolved onto the fault plane. The extreme increases in pore pressure at restraining bends weaken the fault plane, and allow rupture to continue past these bends that arrested rupture previously. Propagation distance was further than in the corresponding Mohr-Coulomb models for all cases in which rupture did not propagate to the fault boundary. Hence, the rough fault is capable of hosting rupture at much lower background stresses than the case with strictly Mohr-Coulomb material behavior.

Notice also that the effect of the undrained gouge behavior is manifest in the final slip distribution when comparing the two material models. In the Mohr-Coulomb cases, the final slip is much lower at restraining bends. Notable restraining bends are centered on x = ~-18 m, x = ~-10, x = 10 m, and x = ~20 m (Figure 1). At higher background stresses, even though rupture is not arrested, propagation through these locations is more difficult due to their unfavorable orientation, and slip is at a local minimum. Conversely, in the case with the undrained gouge end-cap model, pore fluid increase due to compaction provides a stabilizing effect on the rupture behavior, and allows the slip distribution to become much uniform.

The final slip distribution for the Mohr-Coulomb model with τ_b = 50 MPa is particularly noteworthy. Figure 7 provides clarity in what occurred in this simulation by showing slip velocity time histories along the fault. The Mohr-Coulomb case with τ_b =

50 MPa experienced rerupture of a fault segment due to the complicated dynamic stress state on the rough fault. This secondary rupture then propagated in the leftward direction at sub-Rayleigh velocity. Next, at around x = -10 m, a daughter crack developed which initiated a supershear rupture. Note then that at certain locations (e.g. x = -15 m) the fault slipped in three separate episodes: first the primary sub-Rayleigh rupture, followed by the supershear phase of the secondary rupture, and finally the sub-Rayleigh phase of the secondary rupture.

Bruhat et al. [2016] revisited the suite of simulations from Fang and Dunham [2013], and found many cases with similar behavior. They found that overall, rough faults can generate a range of interesting behavior at high background stresses, that include supershear transtions, short supershear transients, rupture jumps, and rerupture of previously ruptured segments. Here, we show that the effect of the compaction and dilatancy occurring in the gouge with the end-cap model is to stabilize these highly unpredictable effects. Large dynamic stress variations that lead to chaotic rupture behavior are limited by the dynamic pore pressure changes. Also note that at certain locations in the Mohr-Coulomb model, restraining bends cause the rupture velocity to decrease (notably at ~12 m in the case with τ_b = 42.5 MPa and ~20 m in the case with τ_b = 45 MPa), but the weakening via undrained compaction in the gouge model is able to rupture through this region at a more constant velocity.

The specific effect of gouge dilatancy and compaction on rupture velocity can be seen in Figure 8. The black curve shows the fault slope, blue and red curves show normalized rupture velocities for the cases with strictly Mohr-Coulomb material behavior and the end-cap gouge material respectively, where τ_b = 45. For this plot, rupture

velocities are demeaned and normalized by the shear wave speed.

As suggested by the behavior seen in Figures 6 and 7, propagation through poorly oriented or more favorably oriented fault segments in the Mohr-Coulomb case will affect the rupture process, making it relatively more difficult or easy to propagate through these segments. Because of this, rupture velocities tend to also either increase or decrease at releasing and restraining bends respectively. This led previous authors to show that rupture velocity was negatively correlated with fault slope [Dunham et al., 2011b; Trugman and Dunham, 2014] (this condition arises because the right-lateral nature of the fault means that releasing bends have a negative slope, restraining bends have a positive slope). The correlation coefficient for the fault slope and the rupture velocity is -0.28 for the Mohr-Coulomb case; the sign of the correlation coefficient is in agreement with those previous models.

For the end-cap case, this behavior is reversed. Due to the large increases in pore pressure, the rupture is actually able to accelerate around restraining bends as the fault becomes weakened prior to the rupture front arrival. This occurs because the stress state in the gouge is very close to the end-cap at these bends, and the large shear stress concentration ahead of the rupture front allows the static friction to be reduced. This reduction in static friction was one of the main findings of Hirakawa and Ma [2016] in a flat fault model. At releasing bends, the stress state may be very close to the Mohr-Coulomb line initially (Figure 4); thus, an analogous effect may take place, where dilatancy and pore pressure reduction prior to rupture dynamically increases the static friction at releasing bends. This renders it more difficult for rupture to propagate through these bends in comparison with the Mohr-Coulomb case, and lowers the rupture velocity

at those bends. For both cases, the correlation coefficient is not nearly as large as those reported in previous studies [Dunham et al., 2011b; Trugman and Dunham, 2014].

Though the sign of the correlation coefficient is reversed with the end-cap model in comparison with the Mohr-Coulomb case, the amplitude of the velocity fluctuations is actually larger. This is qualitatively noticeable by examining the two curves, and is quantified by computing the variance of the rupture velocity curves. The variance is slightly larger for the end-cap model. This occurs because the closeness-to-failure is higher in the gouge near the end-cap, and is also closer to failure on the Mohr-Coulomb line in some locations. Because of this, more inelastic strain develops in the immediate vicinity of the fault plane; the plastic dissipation is known to have a large effect on rupture velocity [Andrews, 2005].

Variations in rupture velocity are known to increase the power of the high-frequency components part of the seismic wave spectrum. Dunham et al. [2011b] showed that large fluctuations in rupture velocity on rough faults did increase the high-frequency part of the acceleration spectrum. We show one seismogram for fault parallel velocity (V_x) at a station located at x = -10 m, and 2.5 meters from the fault in the direction perpendicular to the mean fault plane. From the time series, it appears that the large fluctuations in rupture velocity cause a significant addition to the waveform at high frequencies. We plot the Fourier amplitude spectrum of fault parallel velocity, averaged over 20 stations at the same perpendicular distance to the fault (y = y(f) + 2.5 m). The amplitude spectrum appears to be higher in the end-cap case at high frequencies. More rigorous analysis needs to be done in order to determine whether this is statistically significant; however, this outlines the potential for gouge behavior to influence ground

motions.

3.4. Discussion

With such a model, a large number of assumptions must be made, and may lead to some oversimplifications. We have assumed that the gouge width is constant throughout the whole domain. However, results of this study and other similar ones [e.g. Dunham et al., 2011b] show that large stress concentrations near fault bends cause the inelastic strain field to be heterogeneous. As gouge is thought to be a product of this kind of attritional brecciation [Chester et al., 1993], it is likely that gouge width should vary with fault roughness. The assumption that the gouge boundary itself follows the same geometry as the rough fault profile may be inaccurate as well; in fact, Chester et al. [2004] showed that on the Punchbowl Fault the roughness of the principal fracture surface is much less than on the boundary of the ultracataclasite gouge and the damage zone. It is unclear whether inclusion of these details would affect inelastic gouge deformation, pore pressure changes, and consequent rupture dynamics. Presumably, they may have little effect, as rupture is most effect by compaction and dilatancy in the elements closest to the fault surface.

The consideration of rupture propagation at different length scales is important as well. As faults are self-similar, these types of rough fault models can traditionally be non-dimensionalized, as roughness and resulting fault physics should be analogous at all length scales. However, the inclusion of a 20 cm gouge layer introduces a length scale. Thus, the question arises of whether the behavior shown here at the 10's of meters propagation length scale will still be important at length scales characteristic of observable earthquakes. As we have shown (along with others, e.g. Dunham et al.

[2011b]; Shi and Day [2013]), the rupture is mostly affected by the shortest roughness wavelengths, so it is likely that this will still be a significant factor. For example, propagating cracks in a dry crase that have difficulty nucleating and are immediately arrested may become large earthquakes if under the influence of the mechanism we presented here. However, the effects on ground motion frequency content (as demonstrated in Figure 9) may not be as important, since the spectrum shown there is at the kilohertz band level.

As mentioned in the introduction, the rough fault problem (or fault bend problem) is similar to fault stepovers. In a model without dynamic pore pressure variations, rupture propagation through a releasing bend is much easier than through a restraining bend [Segall and Pollard, 1980]. Harris and Day [1993] showed that the behavior is reversed when dynamic pore pressure changes are included. The inclusion of inelastic material behavior with inelastic volumetric strain may enhance this effect. Large stepover faults may be up to several kilometers apart, thus the compaction and dilatancy of gouge cannot be employed here. However, geologic observations by Sibson [1984] suggest the development of implosion breccia and distributed crush breccia, in extensional and compressional stepovers respectively, develop in relation to a pore fluid phase. This inelastic deformation can further enhance the pore pressure changes and affect rupture jump between branches.

Improvements to the calculation of the initial static stress field can be made. As of now this is an elastic calculation, which allows us to scale the stress field for a desired initial stress state that does not violate the yield surface. Using plasticity during this stage may severely distort the initial stress concentrations. Compaction, hardening, and shear

failure during this interseismic loading could allow an improved calculation of the end-cap parameters. If preseismic compaction occurred over short enough time scales (shorter than the fluid diffusion time), increases in pore pressure could weaken the fault significantly in certain locations. In combination with inclusion of the on fault shear stresses from the interseismic stress calculation (which we neglected in this study), this could provide a means of earthquake nucleation via gouge compaction and pore pressure increase. This would only be possible with a rough fault model, where stresses and strains become concentrated in certain locations.

3.5. Conclusion

Current dynamic rupture models on rough faults require the use of plasticity to limit extreme stress concentrations. However, the simple brittle failure criteria typically used (i.e. the Mohr-Coulomb or Drucker Prager criteria) may be overly simplistic, and do not capture the interesting behavior of fault gouge. Gouge has the property that it readily compacts under increases in shear (shear-enhanced compaction), and if undrained, has the potential to increase pore pressure and reduce rock strength. Conversely, pore pressure decrease during dilatancy can cause restrengthening.

We include the constitutive relation developed for fault gouge, used by Hirakawa and Ma [2016] into a rough fault, and found that many of the properties of rough faults as described by previous authors where diminished or reversed. At restraining bends, large amounts of compaction increase the pore pressure and allow rupture to propagate past bends that arrested rupture in the case with purely Mohr-Coulomb material behavior. Gouge dilatancy and the resultant pore pressure decrease stabilize rupture, and limit complex behaviors of rupture at high background stresses, that include reruptured

segments and supershear rupture. Rather than causing increases and decreases in rupture velocity at releasing and restraining bends respectively, gouge dilatancy and compaction reverses this behavior and causes a rupture velocity increase at restraining bends and a decrease at releasing bends. This leads to a positive correlation coefficient between rupture velocity and fault slope. Overall, the somewhat chaotic behavior observed in current rough fault models is stabilized by the combination of realistic gouge deformation and pore fluid effects.

Chapter 3, in part is currently being prepared for submission for publication of the material. Hirakawa, E. T. and S. Ma, Undrained Gouge Plasticity and Rupture Dynamics of Rough Faults. I was the primary investigator and author of this paper.

References

Andrews, D. J. (2005), Rupture dynamics with energy loss outside the slip zone, *J. Geophys. Res.,* 110(B1), doi:10.1029/2004JB003191.

Aviles, C. A., Scholz, C. H., and Boatwright, J. (1987). Fractal analysis applied to characteristic segments of the San Andreas fault. *Journal of Geophysical Research: Solid Earth*, *92*(B1), 331-344.

Brown, S. R., and Scholz, C. H. (1985). Broad bandwidth study of the topography of natural rock surfaces. *J. geophys. Res*, *90*(B14), 12575-82.

Bruhat, L., Z. Fang, and E. M. Dunham (2016), Rupture complexity and the supershear transition on rough faults, *J. Geophys. Res. Solid Earth*, *121*, doi:10.1002/2015JB012512.

Candela, T., Renard, F., Bouchon, M., Brouste, A., Marsan, D., Schmittbuhl, J., and Voisin, C. (2009). Characterization of fault roughness at various scales: Implications of three-dimensional high resolution topography measurements. *Pure and Applied Geophysics*, *166*(10-11), 1817-1851.

Candela, T., F. Renard, Y. Klinger, K. Mair, J. Schmittbuhl, and E. E. Brodsky (2012), Roughness of fault surfaces over nine decades of length scales, J. Geophys. Res., 117, B08409, doi:10.1029/2011JB009041.

Chester, F. M., and J.M. Logan (1986), Implications for mechanical properties of brittle faults from observations of the Punchbowl fault zone, California, *Pure Appl. Geophys.*, 124(1-2), 79-106.

Chester, F. M., Chester, J. S., Kirschner, D. L., Schulz, S. E., and Evans, J. P. (2004). Structure of large-displacement, strike-slip fault zones in the brittle continental crust. *Rheology and Deformation in the Lithosphere at Continental Margins*, *1*, 223-260.

Chester, F.M, Evans, J.P., and R.L. Siegel (1993), Intemal structure and weakening mechanisms of the San Andreas Fault, *J. Geophys. Res., 98*(B1), 771-786.

Dunham, E. M., and J.R. Rice (2008), Earthquake slip between dissimilar poroelastic materials. *J. Geophys. Res.,* 113(B9), B09304, doi:10.1029/2007JB005405.

Dunham, E. M., Belanger, D., Cong, L., and J.E. Kozdon (2011a), Earthquake ruptures with strongly rate-weakening friction and off-fault plasticity, Part 1: Planar faults, *Bull. Seismol. Soc. Am.,* 101(5), 2296-2307, doi:10.1785/0120100075.

Dunham, E. M., Belanger, D., Cong, L., and J.E. Kozdon (2011b), Earthquake ruptures with strongly rate-weakening friction and off-fault plasticity, Part 2: Nonplanar

faults, *Bull. Seismol. Soc. Am., 101*(5), 2308-2322, doi:10.1785/0120100076.

Fang, Z., and E. M. Dunham (2013), Additional shear resistance from fault roughness and stress levels on geometrically complex faults, J. Geophys. Res. Solid Earth, 118, 3642–3654, doi:10.1002/jgrb.50262.

Harris, R.A., and S. M. Day (1993), Dynamics of fault interaction: Parallel strike-slip faults. Journal of Geophysical Research, 98, 4461-4472.

Hirakawa, E.T. and S. Ma (2016), Dynamic Fault Weakening and Strengthening by Gouge Compaction and Dilatancy in a Fluid-Saturated Fault Zone, submitted to Journal of Geophysical Research, September 8, 2015.

Noda, H., Dunham, E. M., and J. R. Rice (2009), Earthquake ruptures with thermal weakening and the operation of major faults at low overall stress levels. *J. Geophys. Res.,* 114(B7), B07302, doi:10.1029/2008JB006143.

Okubo, P. G., and Aki, K. (1987). Fractal geometry in the San Andreas fault system. *Journal of Geophysical Research: Solid Earth*, *92*(B1), 345-355.

Power, W. L., and Tullis, T. E. (1991). Euclidean and fractal models for the description of rock surface roughness. *Journal of Geophysical Research: Solid Earth*, *96*(B1), 415-424.

Renard, F., C. Voisin, D. Marsan, and J. Schmittbuhl (2006), High resolution 3D laser scanner measurements of a strike-slip fault quantify its morphological anisotropy at all scales, Geophys. Res. Lett., 33, L04305, doi:10.1029/2005GL025038.

Rojas, O., Dunham, E. M., Day, S. M., Dalguer, L. A., and J. E. Castillo (2009), Finite difference modelling of rupture propagation with strong velocity-weakening friction. *Geophys. J. Int.*, *179*(3), 1831-1858, doi: doi:10.1111/j.1365-246X.2009.04387.x.

Rudnicki, J. W., and J. R. Rice (2006), Effective normal stress alteration due to pore pressure changes induced by dynamic slip propagation on a plane between dissimilar materials. *J. Geophys. Res.,* 111(B10), B10308, doi:10.1029/2006JB004396.

Scott, D. R., Lockner, D. A., Byerlee, J. D., and C.G. Sammis (1994), Triaxial testing of Lopez fault gouge at 150 MPa mean effective stress. *Pure Appl. Geophys.*, *142*(3-4), 749-775.

Segall, P., and Pollard, D. D. (1980). Mechanics of discontinuous faults. *Journal of Geophysical Research: Solid Earth*, *85*(B8), 4337-4350.

Segall, P., and J. R. Rice (1995), Dilatancy, compaction, and slip instability of a fluid-

infiltrated fault. *J. Geophys. Res., 100*(B11), 22155-22171.

Shi, Z., and S. M. Day (2013), Rupture dynamics and ground motion from 3-D rough-fault simulations, J. Geophys. Res. Solid Earth, 118, doi:10.1002/jgrb.50094.

Sibson, R. H. (1986). Brecciation processes in fault zones: inferences from earthquake rupturing. *Pure and Applied Geophysics*, *124*(1-2), 159-175.

Templeton, E. L., and J.R. Rice (2008), Off-fault plasticity and earthquake rupture dynamics: 1. Dry materials or neglect of fluid pressure changes. *J. Geophys. Res.,* 113(B9), B09306, doi:10.1029/2007JB005529.

Trugman, D. T., and Dunham, E. M. (2014). A 2D pseudodynamic rupture model generator for earthquakes on geometrically complex faults. *Bulletin of the Seismological Society of America*, *104*(1), 95-112.

Viesca, R. C., Templeton, E. L., and J. R. Rice (2008), Off-fault plasticity and earthquake rupture dynamics: 2. Effects of fluid saturation. *J. Geophys. Res.,* 113(B9), B09307, doi:10.1029/2007JB005530.

Viesca, R. C., and J. R. Rice (2009), Modeling slope instability as shear rupture propagation in a saturated porous medium, in Submarine Mass Movements and Their Consequences, (eds. D. C. Mosher, R.C. Shipp, L. Moscardelli, J. D. Chaytor, C. D. P. Baxter, H. J. Lee, and R. Urgeles), Springer-Verlag, New York, pp. 215-225, 2010.

Wong, T. F., David, C., and W. Zhu, (1997), The transition from brittle faulting to cataclastic flow in porous sandstones: Mechanical deformation. *J. Geophys. Res., (1978–2012)*, 102(B2), 3009-3025.

Zhu, W., L. G. J. Montesi, and T. Wong (2007), A probabilistic damage model of stress-induced permeability anisotropy during cataclastic flow, J. Geophys. Res., 112, B10207, doi:10.1029/2006JB004456.

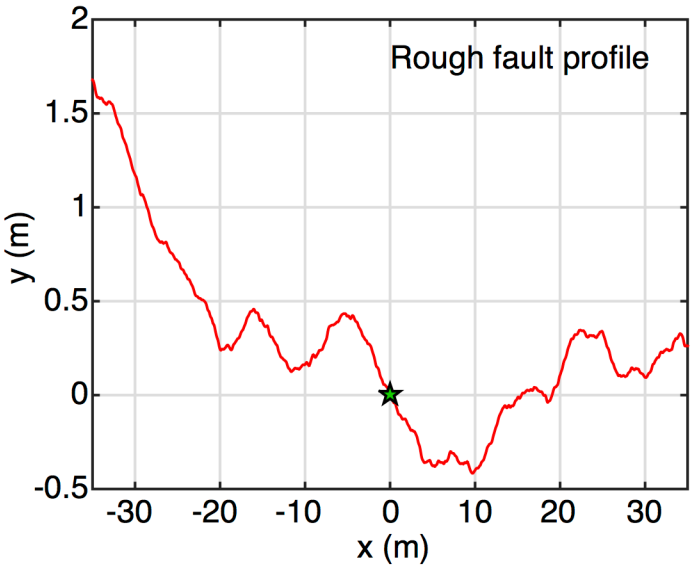

Figure 3.1. Fault profile used for all simulations in this study. The self-similar fault is generated by the method outlined by Shi and Day [2013]. A random set of complex numbers is generated and multiplied by a power-law function, representing the fault in the Fourier domain. A low-pass filter is used to obtain a band-limited fault profile with a minimum roughness wavelength of 30 grid points. The fault profile shown is obtained by taking the inverse Fourier transform of this. We use an amplitude-to-wavelength ratio of 0.01.

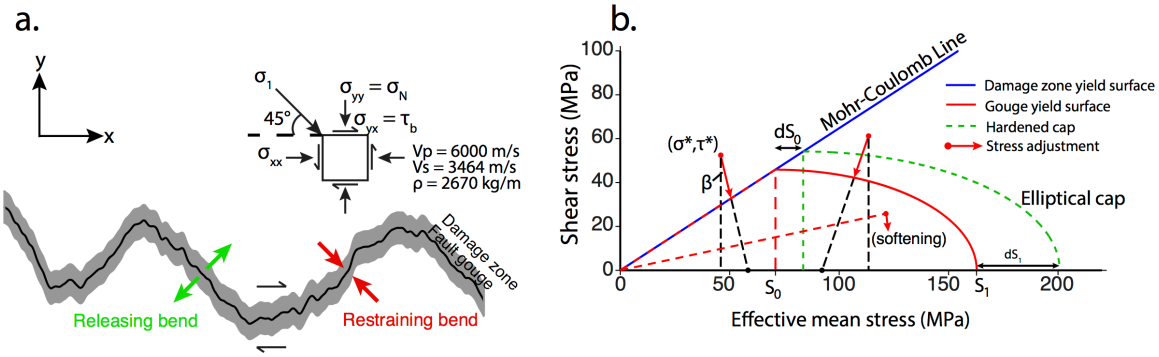

Figure 3.2. a) Domain geometry for a hypothetical portion of the fault. The rough fault shown in Figure 1 is surrounded by a layer of gouge. The gouge follows the topography of the fault and is 20 cm thick along the entire fault. Regional background stresses are set so that the maximum principal stress is oriented at 45° to the fault plane; however, local stress state is heterogeneous (see Figures 3 and 4).
b) Combined Mohr-Coulomb – End-cap yield surface used in this study. The model was developed in Hirakawa and Ma [2016], who described it thoroughly. At low confining stresses, the yield surface used is a Mohr-Coulomb yield criterion. At high yield stresses (above mean stress S_0), an elliptical cap models deformation under mean stress increase or shear. The plastic flow rule is such that failure on the Mohr-Coulomb surface causes dilatancy, while failure on the end-cap causes compaction. The gouge obeys this combined surface, while the damage zone obeys strictly the Mohr-Coulomb surface; they coincide at stresses below S_0.

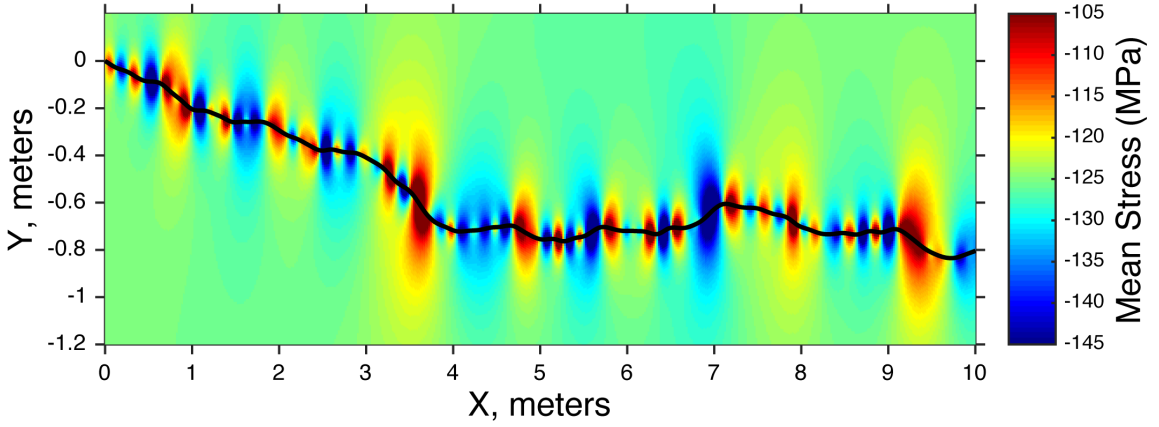

Figure 3.3. Mean stress on one part of the fault obtained by the static stress calculation, which may represent stress buildup from a history of interseismic, coseismic, and postseismic slip. This stress field is used as an initial condition in the dynamic rupture model. Mean stresses are negative in compression. Restraining bends lead to more compressive initial stress states; releasing bends lead to less compressive initial stress states.

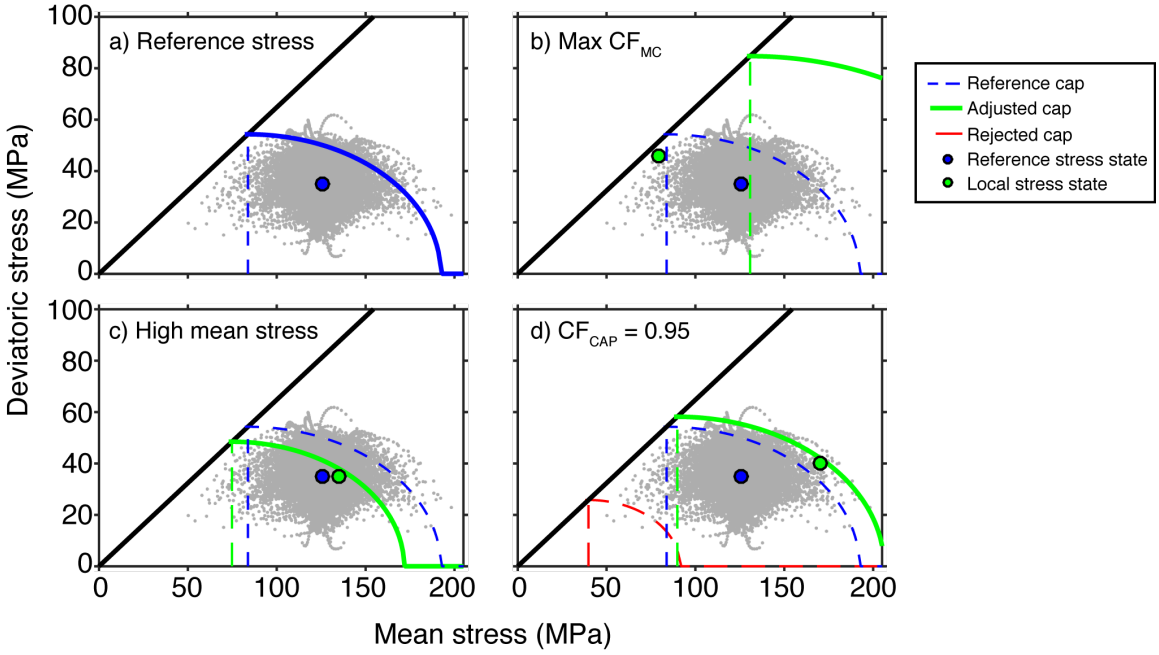

Figure 3.4. Illustration of the adjustment of the ellipse center, S_0, due to the heterogeneous initial stress state. Gray dots show stress at every location in the domain. The blue dot shows the unperturbed (reference) stress state. a) The reference value of S_0 is calculated with the initial unperturbed stress via equation 6, with $CF_{CAP} = 0.70$. b) If perturbed mean stress is lower than the unperturbed stress, S_0 shifts to higher values (via equation 7), and the stress point is much closer to Mohr-Coulomb failure than end-cap failure. c) If mean stress is higher than the unperturbed stress, the cap shifts closer to the stress point; however, this can cause the stress point to be outside of the cap (d). If this is the case we reject that cap and set S_0 based on a maximum value of CF_{CAP} in equation 6, which we choose to be 0.95.

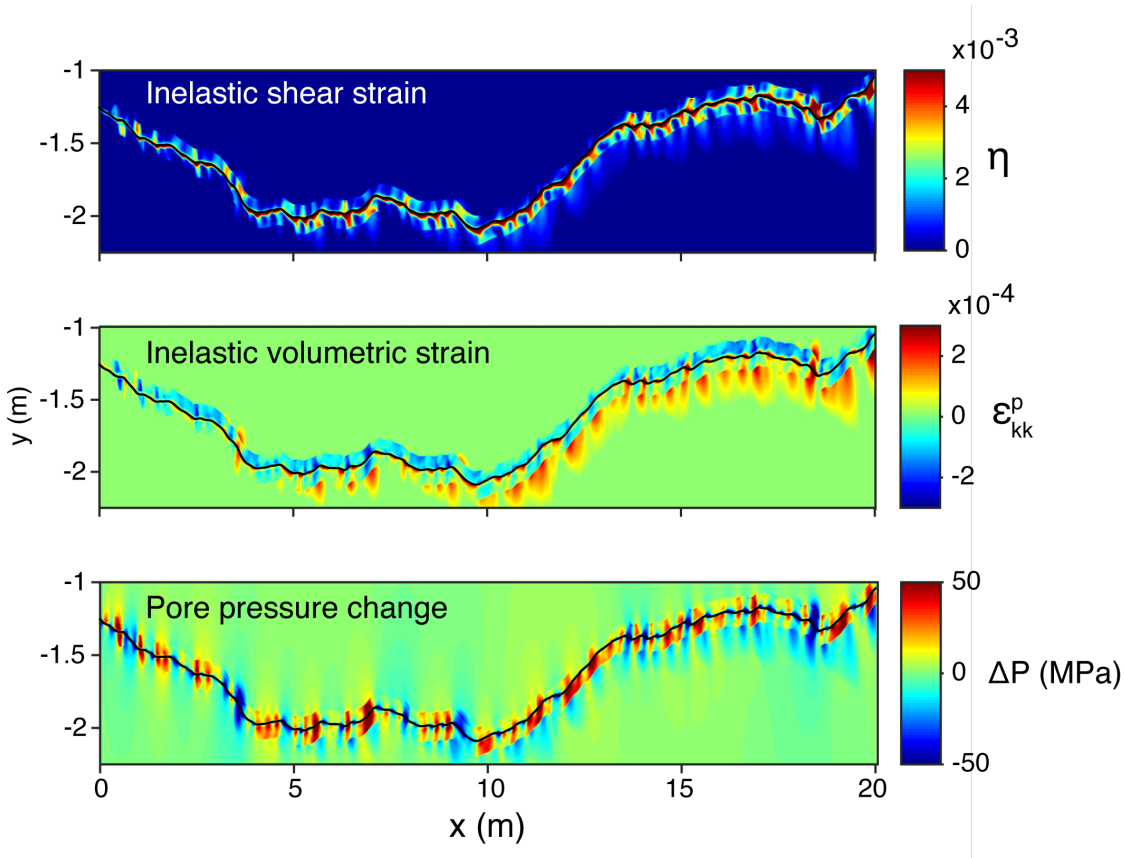

Figure 3.5. Inelastic shear strain (top), inelastic volumetric strain (middle), and off-fault pore pressure change (bottom). The rough fault trace is shown by a black line. The narrow region of highly strained material around the fault trace outlines the fault gouge. Large amounts of compaction (inelastic volumetric strain is negative in compaction) and consequent pore pressure increases develop in restraining bends, while dilatancy and pore pressure reduction develop in releasing bends.

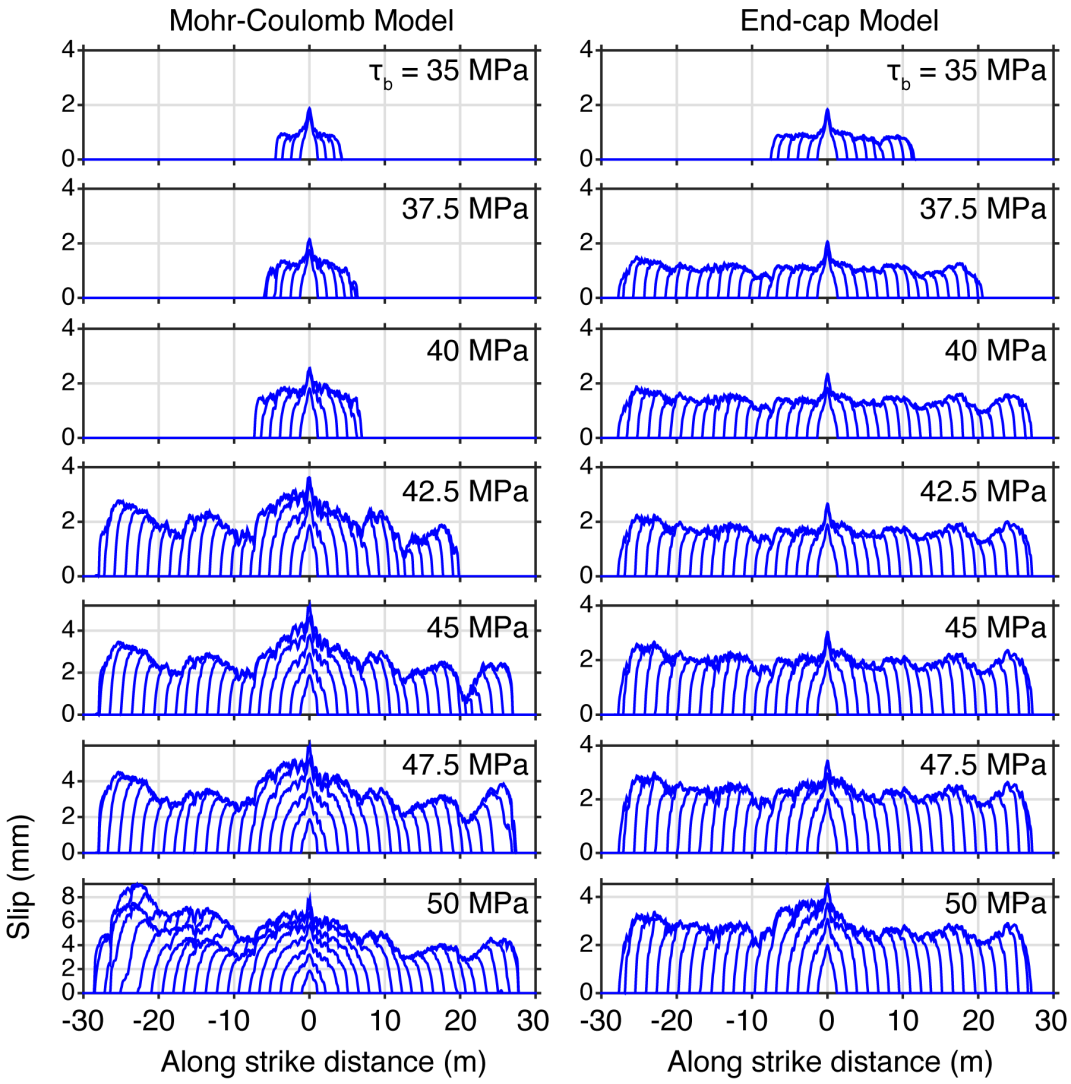

Figure 3.6. Slip contours for cases with varying background stresses, τ_b, comparing cases with only Mohr-Coulomb (MC) failure and no pore pressure change (left panels), with the cases of our undrained gouge model (right panels). The contour interval is 0.5 milliseconds. At low τ_b, rupture arrests quickly in the MC models at restraining bends, while in the models with gouge behavior, rupture is able to propagate farther. At high τ_b, highly irregular final slip distributions in the MC case are smoothed by the undrained gouge behavior.

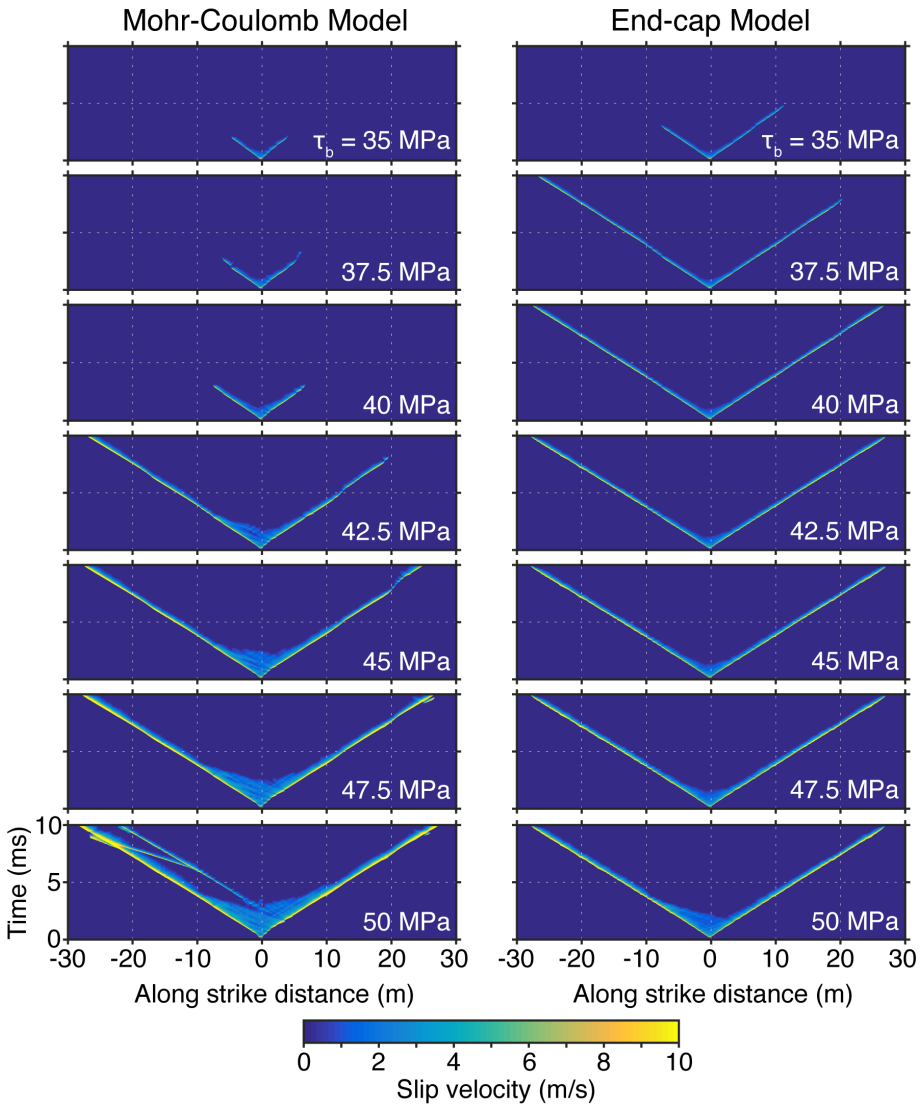

Figure 3.7. Slip velocity time histories for the cases shown in Figure 3.6. The color scale is slip velocity, the y-axis is time, the x-axis is distance along strike. At certain locations in the MC model, restraining bends cause the rupture velocity to decrease (notably at ~12 m in the case with τ_b = 42.5 MPa and ~20 m in the case with τ_b = 45 MPa), but the gouge model is able to rupture through at a more constant velocity. The seemingly chaotic behavior in the MC case at τ_b = 50 MPa has been shown to be characteristic of rough faults at high background stresses [Bruhat et al., 2016], but the compaction and dilatancy in the gouge model has a stabilizing effect on this behavior.

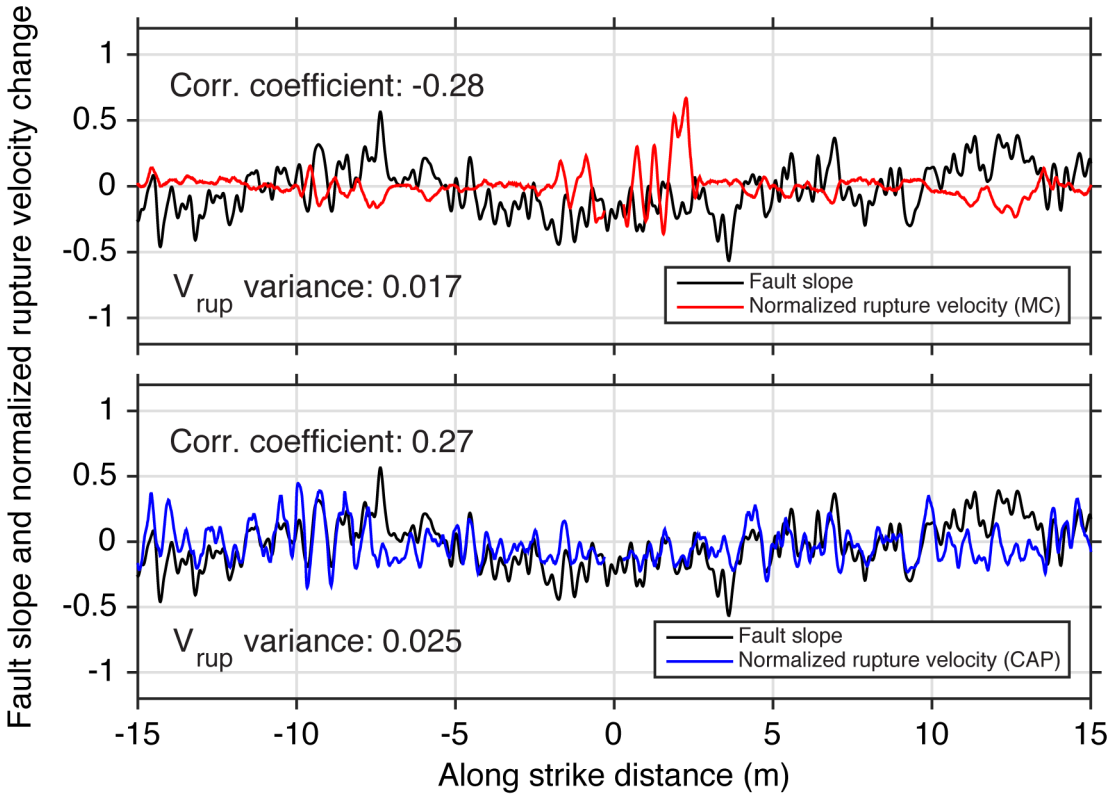

Figure 3.8. Comparison of rupture velocity changes with fault slope. The rupture velocities are demeaned and normalized by the shear wave speed. A negative correlation coefficient between rupture velocity and fault slope is calculated for the MC case, in agreement with previous studies. A positive correlation coefficient is obtained for the case with the end-cap gouge model. Rupture velocity has a larger variance in the gouge model, due to the large amounts of inelastic shear strain owing to the initial closeness-to-failure.

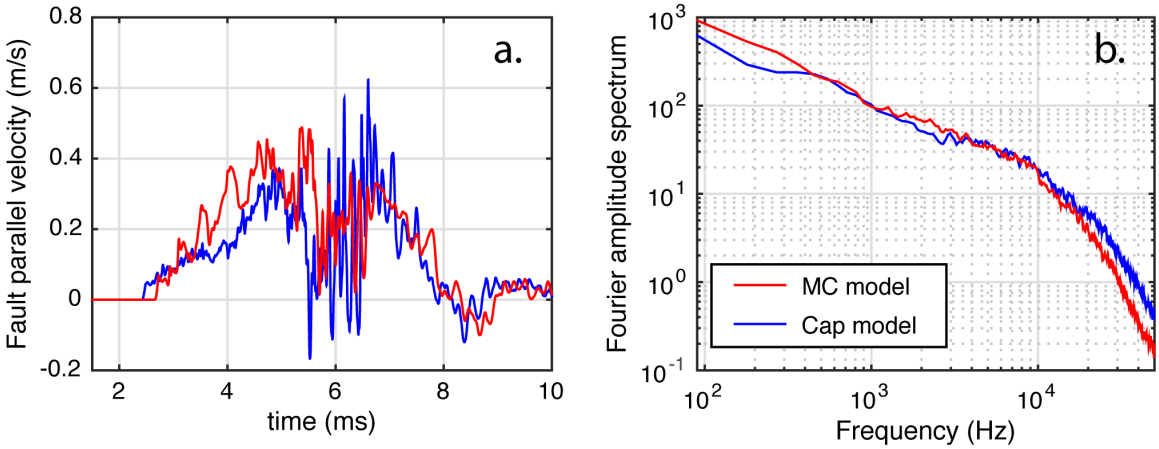

Figure 3.9. a) Time series of fault parallel velocity at x = -10 m, and 2.5 meters from the fault. Notice the high frequency component to the waves in the cap model in comparison with the MC model. This leads to a slightly higher Fourier amplitude (b) at high frequencies. The spectrum shown is averaged over 20 stations at 2.5 meters from the fault. These signals are on the order of kilohertz due to the small scale of the problem.

Chapter 4

Coseismic Strengthening of the Shallow Plate Interface Further Enhances Inelastic Wedge Failure and Tsunami Generation

Abstract

Subduction zone faults host the world's largest earthquakes. They show a range of behaviors that can lead to catastrophic earthquakes and large tsunamis. It is thought that subduction zone megathrusts are partitioned into different regimes. A deep, seismogenic section governed by velocity weakening friction hosts very large earthquakes. In comparison, the shallow updip portion of subduction zone megathrusts is thought to slip aseismically, in response to velocity strengthening friction. However, this latter region of the fault has been found to occasionally rupture coseismically in anomalous events known as 'tsunami earthquakes' [Kanamori, 1972]. Occasionally, large events such as the M_w 9.0 Tohoku-oki earthquake appear to rupture the entire megathrust, and result in catastrophic tsunamis. A unifying theory to explain the wide range of megathrust behavior has been difficult to obtain. Ma and Hirakawa [2013] introduced inelastic failure into the subduction zone wedge, and showed that large amounts of inelastic failure promote more vertical uplift that may enhance tsunamigenesis, and lead to seismic radiation characteristic of tsunami earthquakes.

Here we build on the model of Ma and Hirakawa [2013] by including a velocity strengthening region to the shallow portion of the subduction zone fault. Earthquakes are nucleated on a deeper portion of the fault, below the inelastic wedge. Propagation from

depth causes a large amount of failure as the rupture enters the inelastic wedge. If fault friction is governed by velocity weakening for the entire updip portion, a moderate amount of plastic failure develops, but slip is still high near the trench. If the updip portion of the fault is governed by velocity strengthening behavior, slip on the fault is limited as rupture reaches shallow depths, and energy is redirected into the wedge. This causes more inelastic failure in comparison to the equivalent velocity weakening model, and enhances some of the effects described by Ma [2012] and Ma and Hirakawa [2013]. This model provides insight into a range of observed earthquake behaviors, and physics on different regimes of the megathrust fault.

4.1. Introduction

Large subduction zone megathrusts host some of the world's most destructive earthquakes; yet, they are still poorly understood. Deeper portions of megathrusts (from 15 – 55 km below sea level) experience earthquakes with large total slip and radiate large amounts of coherent high-frequency energy, while the shallowest portion (0 – 15 km below sea level) are usually characterized by either aseismic slip or tsunami earthquakes [Lay et al., 2012]. Physical models are required to address the mechanics leading to this span of behaviors.

The aseismic slip behavior of the shallow region is generally thought to be due to the presence of velocity strengthening frictional properties [e.g. Byrne et al., 1988]. However, the occasional observation of coseismic slip in this region during tsunami earthquakes makes the physics of this region puzzling. Tsunami earthquakes are a special class of earthquakes that are especially tsunamigenic (in relation to their small moment magnitudes), occur over a relatively long duration and have slow rupture velocity, produce weak-high frequency seismic radiation, and consist of low energy-to-moment ratios [e.g. Kanamori, 1972; Newman and Okal, 1998; Lay et al., 2012].

In extreme rare events, unusually large earthquakes occur on subduction zone megathrusts that rupture both of these zones. Recent examples of this are the 2004 Mw9.2 Sumatra earthquake or the 2011 Mw 9.0 Tohoku-oki earthquake. Both of these events caused devastating tsunamis; however, they are not classified as tsunami earthquakes because of their large moment magnitude. Nevertheless, they did exhibit the additional characteristic that energy radiated from their deeper portions was much high frequency than the shallow portion [Lay et al., 2012]. A unifying theory that relates

behaviors of the deep and shallow portions of the megathrust is desired.

Currently, the most popular hypothesis for the long rupture duration and slow rupture velocity of shallow subduction zone earthquakes is the presence of a thin layer of subducted sediments in the fault zone [e.g. Polet and Kanamori, 2000]. However, the low velocity nature of this material alone likely does not lead to the anomalous observations. Dynamic rupture models incorporating a low-velocity fault zone show that the presence of low rigidity materials do not necessarily slow rupture velocity, and actually lead to a more pulse-like rupture [e.g. Harris and Day, 1997]. This inevitably enhances high-frequency radiation, which contradicts the observation of a lack of energy on this part of the spectrum during these earthquakes.

The properties of the subducted material may have the described effect on rupture mechanics if it has velocity-strengthening behavior. Laboratory studies on unconsolidated clay-rich sediments obtained from subduction zone trenches often exhibit this property [e.g. Saffer et al., 2012; Saffer and Marone, 2003]. However, in order for slip to propagate to the trench in extremely large earthquakes such as the 2011 Mw 9.0 Tohoku-oki earthquake, the tendency for this velocity strengthening behavior to arrest rupture needs to be overcome. Recently, developments have been made that suggest that while certain clays exhibit velocity strengthening behavior at low strain rates, they experience sudden velocity weakening at high slip rates [Kitajima et al., 2011; French et al., 2014]. This has led some researchers to believe that earthquakes can propagate through velocity strengthening regions if allowed to gain enough momentum during nucleation in a velocity weakening region [Faulkner et al., 2011; Noda and Lapusta, 2013].

Such complicated slip-rate dependent behavior may be not necessary, as rupture

still may be able to propagate through entirely velocity strengthening regions if driven by a large enough downdip rupture. Kozdon and Dunham [2013] modeled the 2011 Mw 9.0 Tohoku-oki earthquake with deep rupture on a velocity weakening segment, propagating into a shallow velocity strengthening segment. They showed that after accounting for depth dependent material properties and complex geometry of the fault and seafloor, large stress changes are transmitted to the shallow velocity strengthening portion of the fault by amplifications of trapped waves in the shallow wedge, that originate from downdip rupture. This allows rupture to be driven to the trench.

Dynamic rupture models of subduction zone earthquakes can be improved with more realistic physical behavior. Most models consider the off-fault material to be linearly elastic. However, geologic observations suggest that inelastic failure of accretionary wedges is an intrinsic part of the earthquake cycle. Critical taper theory [Davis et al., 1983; Dahlen, 1984] considers accretionary wedges to be analogous to wedges of deforming soil or snow that form in front of a moving bulldozer. The actively accreting wedge attains a critical taper, which corresponds to an internal stress state that is on the verge of material failure throughout the entire wedge.

Wang and Hu [2006] clarified that the classic critical taper models must only be thought of as an end member scenario, which describes an ‘average’ state over the life cycle of an accretionary wedge, which is necessary to explain the movement of such a thrust sheet with the observed geometry. They postulated that the actively deforming updip portion of the wedge (referred to as the outer wedge) overlies a velocity strengthening portion of the fault, while the less deformed inner wedge overlies a velocity-weakening seismogenic zone. During the interseismic period, the outer wedge

need not be on the verge of failure. Earthquakes nucleating in the velocity-weakening portion of the fault can propagate into the updip velocity-strengthening portion of the fault. They showed that the increase in basal friction during velocity strengthening pushes the outer wedge into a critical state coseismically. Hu and Wang [2008] used a static finite element model to model this stress transfer between the different regimes, and found that the theory of Wang and Hu [2006] can explain the geometry of a number of subduction zone wedges.

Recently, ideas from critical taper theory have been incorporated into dynamic rupture models. Ma [2012] showed that by considering wedge inelasticity and the condition that the initial stress state is on the verge of failure, large amounts of inelastic deformation in the accretionary wedge cause more vertical uplift than a comparable elastic model. Dynamic increases in pore pressure from the compressive stress state in the wedge further weaken the off-fault material. The large amount of vertical uplift should enhance tsunamigenesis, without relying on huge slips near the trench as required by elastic models. Ma and Hirakawa [2013] extended this dynamic rupture model to show that other anomalous observations from shallow subduction zone earthquakes can be explained by extensive wedge failure, including slow rupture propagation, deficiency in high frequency energy, and reduced energy-to-moment ratios.

In this study, we wish to combine the ideas from these models. We model rupture propagation on a large subduction zone megathrust. Rupture is nucleated on a velocity weakening portion below the accretionary wedge, a shallow updip portion of the fault has velocity strengthening friction. As in Ma [2012] and Ma and Hirakawa [2013], the accretionary wedge can experience inelastic failure. This is described by the Mohr-

Coulomb yield criterion. Extensive failure develops in the wedge as rupture propagates to shallower depths. If velocity strengthening is included, continued rupture on the fault becomes unfavorable; this redirects energy into the wedge and causes more off-fault inelastic deformation than in cases with only velocity weakening. The results are in qualitative agreement with the quasistatic analysis of Wang and Hu [2006], in that an increase in basal friction by velocity strengthening will drive the wedge closer to failure. We show that this results in more uplift than the case with only velocity weakening, can possible cause larger tsunamis, and may have implications for the development of splay faults in accretionary wedges.

4.2. Methods

We model dynamic rupture on a 2D dipping fault, which represents a large subduction zone megathrust in plane strain (Figure 1). Certain aspects of this model are very similar to those of Ma [2012] and Ma and Hirakawa [2013], thus only a brief overview of those are summarized here. We use two geometries: 1) a 10° dipping fault with a 5° continental slope, giving a wedge with a 15° taper; and 2) a 6° dipping fault with a 4° continental slope, giving a wedge with a 10° taper. Elastic properties of all models are homogeneous, where density, P-wave velocity, and S-wave velocity are ρ = 2700 kg/m^3, V_p = 6000 m/s, and V_s = 3464 m/s.

The material is poroelastic and considered to be undrained. Pore pressure changes are calculated from mean stress changes in the undrained condition as

(1)

where ΔP is pore pressure change, B is skempton's coefficient, and $\Delta\sigma_m$ is mean stress change.

We define the inelastic wedge as the region above the fault, extending from the trench to the location where the vertical distance between the fault and the continental slope is 15 kilometers. Beyond this region, the off-fault material behaves elastically, and the surface slope is zero (Figure 1). The material strength in the wedge is governed by the Mohr-Coulomb failure criterion, given by

$$\bar{\tau} = c\cos\phi - (\sigma_m + P)\sin\phi \tag{2}$$

where $\bar{\tau}$ is the second invariant of the deviatoric stress tensor, c is cohesion, and ϕ is the internal friction angle. Stresses are first updated elastically by our finite element model, and evaluated for the yield condition. If the yield surface is violated, stresses are adjusted back to the yield surface; this adjustment corresponds to an increment in seismic moment and inelastic strain. Failure occurs only via shear in this model (inelastic volumetric strain is zero). Note that the Mohr-Coulomb equation is identical to the Drucker-Prager yield criterion in plane strain. A more complete description of the poroplastic behavior employed here can be found in Ma and Hirakawa [2013].

The initial stress state in the wedge is calculated from the solution of Dahlen [1984] (or similarly from Wang and Hu [2006]), which gives the equations for stress in a critically tapered wedge of an assumed surface slope. Overburden stress increases with depth and is one of the principal stresses. In light of the critical taper theory, we first calculate the stress state such that the wedge at the point of failure (i.e. the stress point is at the Mohr-Coulomb yield criterion). In a cohesionless wedge, this stress state is given by

$$0.5(\sigma_{zz} - \sigma_{xx}) = \frac{-\sigma_{zz}^{eff}}{\csc\phi\sec 2\Psi - 1} \tag{3}$$

$$\sigma_{xz} = \frac{-\tan 2\Psi \sigma_z^{eff}}{\csc\phi \sec 2\Psi - 1} \tag{4}$$

where $\sigma_z^{eff} = \sigma_z + P$, and Ψ is the angle between the maximum principal stress and the x-axis. However, the use of these stresses as an initial condition in our model require that initial stresses are not at the state of failure. To account for this, we adjust the value of cohesion in equation 2 accordingly so that a desired closeness-to-failure (CF) is obtained. Closeness-to-failure (CF) is defined by

$$CF = \frac{\bar{\tau}^{init}}{c\cos\phi - \sigma_m^{init}\sin\phi} \tag{5}$$

[e.g. Templeton and Rice, 2008; Ma, 2012; Ma and Hirakawa, 2013], where the superscript *'init'* shows that it is an initial value. Note that since the stresses increase with depth, and the only adjustable parameter to maintain constant CF is the cohesion, cohesion is depth dependent as well in equation 2.

Earthquake rupture is modeled using the split node method [e.g. Andrews, 1977; Day et al., 1982]. On-fault effective normal stress σ_N^{eff} is defined by $\sigma_N^{eff} = \sigma_N(1-\lambda)$ where λ is a fluid pressure ratio [e.g. Hubbert and Rubey, 1959]. On the portion of the fault below the wedge, normal stress σ_N and shear stress τ are defined by the stress state in equations 3 and 4 resolved onto the fault plane. Beyond the wedge (at more negative x-values), σ_N is held at the constant value equivalent to its magnitude at the bottom of the wedge. The fluid pressure ratio λ is set so that shear stress is equal to $0.6\sigma_N^{eff}$ everywhere. Below the wedge, λ is smoothly ramped to a higher value so σ_N^{eff} is reduced 40 MPa. Initial shear stress on the fault is always equal to $0.6\sigma_N^{eff}$. The fluid

overpressure at depth and resulting reduction in effective normal stress is done to limit extremely high stress drops on this portion of the fault, and does not reflect any physical properties in real subduction zones at depth. Kozdon and Dunham [2013] used a similar stress profile. Our depth dependent stress profile is shown in Figure 2.

Velocity dependent friction is modeled using rate-and-state friction with state variable evolution governed by the slip law. During non-negligible sliding velocity, friction evolves towards a slip rate dependent steady-state value, $f_{ss}(V)$, given by

$$f_{ss}(V) = f_0 - (b-a)\ln\left(\frac{V}{V_0}\right) \tag{6}$$

where f_0 is a reference friction coefficient at sliding velocity V_0, a is the direct effect parameter, and b is a state variable evolution parameter. The sign of the term ($b - a$) determines whether the system is velocity weakening or velocity strengthening. Positive values correspond to velocity weakening, negative values correspond to velocity strengthening. Figure 3 shows the values for a and b as a function of depth that we use in this study. In all simulations, the hypocenter is located in a velocity weakening region. The state variable evolution parameter b is held at a constant value of 0.014 along the entire fault; the direct effect parameter a is adjusted to control whether the fault is velocity strengthening or velocity weakening. A downdip region of velocity strengthening begins at a distance 10 kilometers from the downdip end of the fault, where the direct effect parameter a is increased to 0.05. In our models with velocity strengthening in the updip region, a increases to 0.018 at the fault location where the wedge thickness (i.e. the vertical distance from the fault to the continental slope) is 5 kilometers.

The element size on the fault and in the wedge is dx = 100 meters. Rupture is nucleated by applying an instantaneous perturbation in shear stress on the fault, given by a Gaussian function in space. The standard deviation of the Gaussian is 1500 meters (15dx), and its amplitude is equal to 0.25 times the effective stress on the fault. The time step used in our finite element algorithm is 0.0025 seconds. For the cases with a wedge taper of 15°, the simulation time is 130 seconds. The fault is longer in the cases with a wedge taper of 10°, and thus require more simulation time. For these cases, the simulation time is 150 seconds.

4.3. Results

Figure 4 shows a comparison between two cases with a wedge taper of 15° with either velocity weakening friction or velocity strengthening friction at the updip portion of the fault (left and right panels respectively); snapshots are shown of an interesting part of the rupture process. These cases both had an initial closeness-to-failure CF = 0.90. Snapshots from the moments before rupture encounters the velocity strengthening region are shown, which correspond to the conditions at the time indicated at the lower right corner of each subplot. Each snapshot shows the upper portion of the fault (beginning with the leftmost terminus of the wedge; the fault is shown with a solid white line), a plot of slip velocity along that portion in the fault at that point in time (magenta curve) and a plot of the friction change along the fault at that point in time (i.e. $\Delta[\tau/\sigma_N^{eff}]$: the change from the initial friction value of 0.6; the curve is plotted such that zero change, or initial friction, coincides with the fault line; this is shown by the green curve). The color scale shows the log of the inelastic shear strain η. Red arrows show surface displacement vectors; the number near the peak of each set of vectors indicates the peak surface uplift

(U_z).

Prior to the first snapshots shown here (at t = 20 seconds), rupture propagated from the lower reaches of the fault where the material response is elastic (see Figure 6e,f for the slip velocity time history for this case). By t = 20 seconds, the rupture has advanced into the section of the fault underlying the inelastic wedge, and damage has begun to accumulate. The location of the rupture front can be inferred by the sudden jump in slip velocity; fault friction drops towards the value governed by equation 6 behind the rupture front since this is the velocity weakening section in both cases. Large stresses carried by surface waves combined with the low strength of materials at the low confining stresses cause damage to first appear in the shallow parts of the continental slope, near the surface.

At t = 25 seconds, the rupture begins to approach the updip velocity strengthening transition in the right panels of Figure 4, but both cases are roughly identical up to this point. The peak slip velocity is lower as more inelastic strain begins to develop, and the slip pulse has a secondary maximum indicating a prolonged slip duration at this point (this slip velocity profile was referred to as a 'snail-like' rupture by Ma and Hirakawa [2013] due to the curve's resemblance to a snail's body). Ma and Hirakawa [2013] showed that this slip mode led to a reduction in high-frequency energy in relation to an elastic case.

After this, the rupture propagates to the trench in the case with only velocity weakening. Ma [2012] and Ma and Hirakawa [2013] both showed that even with slip weakening friction up to the trench, a large development of inelastic strain was able to arrest the rupture, and limit the slip to near zero at the trench. However, here we see that

slip velocity is still relatively high, and large amounts of slip are allowed at the trench (see also Figure 6). The difference between this model and the previous ones is the use of a different friction law (velocity weakening vs. slip weakening) and the fact that here, rupture is driven from much greater depths and is able to gain significantly more momentum. The friction change ratio $\Delta[\tau/\sigma_N^{eff}]$ is negative up to the trench due to velocity weakening.

This part of the rupture is different in the case with velocity strengthening in the updip portion. Here, the negative value of (b – a) causes friction to increase during non-negligible sliding velocity. This dynamic strengthening of the fault causes continued rupture to be more unfavorable, and requires more energy to drive rupture further. Instead, slip velocity diminishes to zero and energy is redirected into the wedge, which is allowed to deform inelastically. This huge concentration of stress causes a larger amount of inelastic strain in the wedge. Note that the surface displacement vectors are more vertical due to velocity strengthening, in comparison to the velocity weakening case where the displacement vectors are more fault-parallel. Fault parallel surface displacements reflect the fact that they are mainly caused by slip on the fault; while more vertical displacements are caused by extensive off-fault failure [Ma, 2012], which causes larger peak vertical uplift.

In Figure 5, the final inelastic strain distribution and surface displacement fields are shown for a number of cases with taper angle 15° and varying initial closeness-to-failure CF. The amount of inelastic failure is governed by the initial CF value (indicated at the bottom right corner of each subplot). An elastic case is obtained by essentially setting CF = 0.0 (top row in Figure 5). Also shown are the maximum vertical uplifts and

their locations, and a ratio of off- and on-fault potency contributions. The left panels are models with velocity weakening friction everywhere; the right panels have velocity strengthening friction in the updip portion.

A ratio of normalized uplifts is provided for reach row of subplots. The value marked ‘Scaled uplift ratio’ is a ratio of the maximum uplifts for each case scaled by their respective moments. The value marked ‘Scaled uplift volume ratio’ is a ratio of the volume of uplift for each case (i.e. the integral of positive vertical displacement) scaled by their respective moments. The ratio is taken by dividing the value for the velocity strengthening model with that of the corresponding velocity weakening model, for a given CF value.

In the elastic case, the moment-scaled uplift ratio is 0.97, indicating that the uplift efficiency is less in the velocity strengthening case. This should be predictable, as the rupture is prohibited from reaching the shallowest reaches of the fault, and elastic deformation is overall lower from the reduction in slip. The opposite is true of all inelastic cases (CF > 0.0). As seen in Figure 4, when the rupture encounters a velocity strengthening region, continued rupture becomes difficult on the fault and energy is redirected into the wedge. This causes more inelastic failure than in the corresponding velocity weakening cause, and causes a larger amount of vertical uplift. This also manifests as a higher off- to on-fault potency ratio. Scaled uplift volume appears to higher for all velocity strengthening cases; however, no systematic trend is apparent.

More clarity on the fault’s rupture time history and slip profile is provided in Figure 6, where slip velocity time histories along the fault are provided for the cases shown in Figure 5. The vertical axis is simulation time; the horizontal axis is distance

from the trench. The red curves superimposed on these plots are the final slip distributions along the fault. The dashed white lines are located at the downdip distance to the wedge terminus (around ~56 kilometers) and the edge of the velocity strengthening region (around ~20 kilometers).

In the elastic case, both the velocity weakening and velocity strengthening models allow rupture to the trench. The rupture velocity becomes supershear at shallow depths, and the strong breakout phase when the rupture reaches the free surface is evident. The case with CF = 0.70 has little inelastic shear, and thus these rupture aspects are qualitatively similar to the elastic case. When CF = 0.90, large amounts of inelastic deformation limit the rupture even in the velocity weakening model, and supershear rupture is largely prevented (a small supershear transition can be noticed, but this phase is quickly terminated). In the velocity strengthening model with CF = 0.90, the dynamic increase in basal friction limits the rupture such that there is nearly zero slip at the trench (this is the case shown in Figure 4). When CF = 0.95, rupture is already severely limited in the velocity weakening model by the time the rupture approaches the trench; however slip velocity is still nonzero and leads to around 18 meters of slip at the free surface. In comparison, rupture arrests very soon after encountering the velocity strengthening portion when CF = 0.95. Figures 7 and 8 are similar to Figures 5 and 6, but for the cases with a 10° taper. From Figure 7, we see that with a 10° taper and increasing values of CF, the moment-scaled uplift and uplift volume becomes significantly higher with velocity strengthening.

For both tapers (Figures 5 and 7), a large concentration of localized inelastic shear strain is evident in the cases with CF = 0.95 and velocity strengthening. This is also

noticeable by the abrupt change in the uplift pattern, where a rather discontinuous uplift trend indicates the surface exposure of this localization and a sharp increase in uplift. Here the extreme closeness-to-failure, the increase in basal friction from velocity strengthening, and the large redirection of stresses into the wedge combine to produce a large shear strain localization. The orientation of the localization likely represents the optimally oriented failure plane, as energy is redirected off the unfavorable fault plane. Inelastic shear localizations in accretionary wedges can be thought of as splay faults [Hirakawa and Ma, 2013].

4.4. Discussion and Conclusion

Our results agree with the idea postulated by Wang and Hu [2006]. As ruptures that originate in a velocity weakening region enter a velocity strengthening region, the sudden increase in basal friction causes the accretionary wedge to become closer to failure. In our model, this leads to a significant increase in off-fault inelastic deformation in relation to the case without velocity strengthening; however, damage is still widespread in that case. Thus, the requirement from previous models [e.g. Ma and Hirakawa, 2013] of incipient failure (CF = 0.99) may be relaxed.

Kozdon and Dunham [2013] used an elastic model of a large subduction zone earthquake to simulate the Mw 9.0 Tohoku event. They found that velocity strengthening in the shallow portion of the megathrust did not prohibit rupture to the trench, if driven by a large enough rupture downdip. Their preferred model produced around ~25 - 30 meters of slip at the trench. Rupture propagation to the trench and large slip is desired in respect to the observations of extremely large (~50 m) slip at the trench in the Tohoku earthquake [Fujiwara et al., 2011]. In this model, we did not aim to rigorously model the

Tohoku event; this is a hypothetical subduction zone model. However, our results from the elastic case are similar to those of Kozdon and Dunham [2013]: where even with velocity strengthening on the shallow portion of the fault, strong rupture nucleated on a velocity weakening segment at depth allowed propagation to the trench and caused a large amount of slip (~45 m in our elastic models).

The critical taper theory of Davis et al. [1983] applies mostly to accretionary wedges. However, the Japan Trench is an erosional wedge, where very little accretion takes place [Von Huene, 1982]. Thus, the concept of incipient failure and the conclusions of Ma [2012] and Ma and Hirakawa [2013] may not apply to the Tohoku event. Even though large stresses from such a huge earthquake should cause at least some irreversible damage, it is questionable whether the Tohoku earthquake may have caused extensive inelastic failure in the wedge. Our model may provide insight into the other end member scenario: actively accreting wedges that are described by the critical taper theory, where a large amount of inelastic deformation likely occurs and the entire wedge may be pushed into failure during large events. Subduction zones along the Barbados Ridge, off Southern Mexico, the Nankai margin, and the Alaska margin accommodate active accretion [Westbrook and Smith, 1983; Moore et al., 1983a,b; Wang and Hu, 2006].

Splay faults are a key feature of accretionary wedges and may occasionally rupture coseismically. Notable examples of coseismic splay fault activation were observed with the 1964 Alaska earthquake [Plafker, 1965], the 1944 Tonankai earthquake [Park et al., 2002; Moore et al., 2007], and possibly the 2004 Sumatra earthquake [Sibuet et al., 2007]. As noted in the two cases with CF = 0.95 and velocity strengthening, strong concentration of stresses in a material that is initially close to failure generated a shear

localization. This can be thought of as a splay fault in a subduction zone model. However, localizations in numerical models are highly irregular, and it has been shown that their locations do not converge when the grid size is refined [e.g. Templeton and Rice, 2008].

In an unpublished work, Hirakawa and Ma [2013] used the model setup of Ma [2012] and Ma and Hirakawa [2013], and studied the development of splay faults in an accretionary wedge. It was found that splay faults developed both when CF was very high, and when Skempton's coefficient (B) was low. This second observation is related to the fact that larger values for Skempton's coefficient decrease the hardening parameters required to limit localization [Viesca et al., 2008]. However, in that study it was found that the location of splay fault development did not converge under varying grid size and parameter selection, in verification with Templeton and Rice [2008]; thus, their use in a deterministic tectonic model may be difficult to justify. Here we show that the location of the splay fault at least coincides with the location of the velocity strengthening transition, and there is a physical explanation for its development and location. The pursuit of a detailed splay fault generation model as a result of shear localization may be the focus of a following work.

The use of velocity strengthening to varying degrees in subduction zone models with off-fault plasticity may explain a range of behaviors. Models with low CF lead to very little inelastic failure and thus may represent models at erosive or non-accreting margins, leading to large slip at the trench. Models with high CF will cause extensive failure in the wedge, and lead to characteristics of tsunami earthquakes [Ma, 2012; Ma and Hirakawa, 2013]. In the latter case, when rupture enters a velocity strengthening

region, these features are enhanced, and under certain conditions may lead to localization of shear and rupture of splay faults. This dynamic model is in agreement with the modified critical taper theory of Wang and Hu [2006], which was a quasi-static analytical model.

Chapter 4, in part is currently being prepared for submission for publication of the material. Hirakawa, E. T. and S. Ma, Coseismic Strengthening of the Shallow Plate Interface Further Enhances Inelastic Wedge Failure and Tsunami Generation. I was the primary investigator and author of this paper.

References

Andrews, D. J. (1976). Rupture velocity of plane strain shear cracks. *Journal of Geophysical Research*, *81*(32), 5679-5687.

Byrne, D. E., Davis, D. M., and Sykes, L. R. (1988). Loci and maximum size of thrust earthquakes and the mechanics of the shallow region of subduction zones. *Tectonics*, *7*(4), 833-857.

Dahlen, F. A. (1984). Noncohesive critical Coulomb wedges: An exact solution. *Journal of Geophysical Research: Solid Earth*, *89*(B12), 10125-10133.

Davis, D., Suppe, J., and Dahlen, F. A. (1983). Mechanics of fold‐and‐thrust belts and accretionary wedges. *Journal of Geophysical Research: Solid Earth*, *88*(B2), 1153-1172.

Day, S. M. (1982). Three-dimensional simulation of spontaneous rupture: the effect of nonuniform prestress. *Bulletin of the Seismological Society of America*, *72*(6A), 1881-1902.

Faulkner, D. R., T. M. Mitchell, J. Behnsen, T. Hirose, and T. Shimamoto (2011), Stuck in the mud? Earthquake nucleation and propagation through accre- tionary forearcs, *Geophys. Res. Lett.*, 38, L18303, doi:10.1029/ 2011GL048552.

French, M. E., H. Kitajima, J. S. Chester, F. M. Chester, and T. Hirose (2014), Displacement and dynamic weak- ening processes in smectite-rich gouge from the Central Deforming Zone of the San Andreas Fault, *J. Geophys. Res. Solid Earth*, *119*, 1777–1802, doi:10.1002/2013JB010757.

Fujiwara, T., Kodaira, S., Kaiho, Y., Takahashi, N., and Kaneda, Y. (2011). The 2011 Tohoku-Oki earthquake: Displacement reaching the trench axis. *Science*, *334*(6060), 1240-1240.

Harris, R. A., and Day, S. M. (1997). Effects of a low-velocity zone on a dynamic rupture. *Bulletin of the Seismological Society of America*, *87*(5), 1267-1280.

Hirakawa, E. T. and S. Ma (2013), Strain Localization in the Coulomb Wedge and the Stabilizing Role of Fluids: A New Splay Faulting Model in the Shallow Subduction Zone, *SCEC Meeting Abstract, September 2013*.

Hu, Y., and K. Wang (2008), Coseismic strengthening of the shallow portion of the subduction fault and its effects on wedge taper, *J. Geophys. Res*., 113, B12411, doi:10.1029/2008JB005724.

Hubbert, M. K., and Rubey, W. W. (1959). Role of fluid pressure in mechanics of

overthrust faulting I. Mechanics of fluid-filled porous solids and its application to overthrust faulting. *Geological Society of America Bulletin*, *70*(2), 115-166.

Kanamori, H. (1972). Mechanism of tsunami earthquakes. *Physics of the earth and planetary interiors*, *6*(5), 346-359.

Kitajima, H., F. M. Chester, and J. S. Chester (2011), Dynamic weakening of gouge layers in high‐speed shear experiments: Assessment of temperature‐dependent friction, thermal pressurization, and flash heating, *J. Geophys. Res.*, 116, B08309, doi:10.1029/2010JB007879.

Kozdon, J. E., and Dunham, E. M. (2013). Rupture to the trench: Dynamic rupture simulations of the 11 March 2011 Tohoku earthquake. *Bulletin of the Seismological Society of America*, *103*(2B), 1275-1289.

Lay, T., H. Kanamori, C. J. Ammon, K. D. Koper, A. R. Hutko, L. Ye, H. Yue, and T. M. Rushing (2012), Depth-varying rupture properties of subduction zone megathrust faults, *J. Geophys. Res.*, 117, B04311, doi:10.1029/2011JB009133.

Ma, S. (2012), A self-consistent mechanism for slow dynamic deformation and tsunami generation for earthquakes in the shallow subduction zone, *Geophys. Res. Lett.*, 39, L11310, doi:10.1029/2012GL051854.

Ma, S., and Hirakawa, E. T. (2013). Dynamic wedge failure reveals anomalous energy radiation of shallow subduction earthquakes. *Earth and Planetary Science Letters*, *375*, 113-122.

Moore, G. F., Bangs, N. L., Taira, A., Kuramoto, S., Pangborn, E., and Tobin, H. J. (2007). Three-dimensional splay fault geometry and implications for tsunami generation. *Science*, *318*(5853), 1128-1131.

Moore, J. C., Watkins, J. S., Shipley, T. H., McMILLEN, K. J., Bachman, S. B., and Lundberg, N. (1982). Geology and tectonic evolution of a juvenile accretionary terrane along a truncated convergent margin: Synthesis of results from Leg 66 of the Deep Sea Drilling Project, southern Mexico. *Geological Society of America Bulletin*, *93*(9), 847-861.

Moore, J. C., Biju-Duval, B., Bergen, et al. (1982). Offscraping and underthrusting of sediment at the deformation front of the Barbados Ridge: Deep Sea Drilling Project Leg 78A. *Geological Society of America Bulletin*, *93*(11), 1065-1077.

Newman, A. V., and Okal, E. A. (1998). Teleseismic estimates of radiated seismic energy: The E/M~ 0 discriminant for tsunami earthquakes. *Journal of Geophysical Reserch, 103*, 26-885.

Noda, H., and Lapusta, N. (2013). Stable creeping fault segments can become destructive as a result of dynamic weakening. *Nature*, *493*(7433), 518-521.

Park, J. O., Tsuru, T., Kodaira, S., Cummins, P. R., and Kaneda, Y. (2002). Splay fault branching along the Nankai subduction zone. *Science*, *297*(5584), 1157-1160.

Plafker, G. (1965). Tectonic Deformation Associated with the 1964 Alaska Earthquake The earthquake of 27 March 1964 resulted in observable crustal deformation of unprecedented areal extent. *Science*, *148*(3678), 1675-1687.

Polet, J., and Kanamori, H. (2000). Shallow subduction zone earthquakes and their tsunamigenic potential. *Geophysical Journal International*, *142*(3), 684-702.

Saffer, D. M., and Marone, C. (2003). Comparison of smectite-and illite-rich gouge frictional properties: application to the updip limit of the seismogenic zone along subduction megathrusts. *Earth and Planetary Science Letters*, *215*(1), 219-235.

Saffer, D. M., D. A. Lockner, and A. McKiernan (2012), Effects of smectite to illite transformation on the frictional strength and sliding stability of intact marine mudstones, *Geophys. Res. Lett.*, 39, L11304, doi:10.1029/2012GL051761.

Sibuet, J. C., Rangin, C., Le Pichon, X., Singh, S., Cattaneo, A., Graindorge, D., ... and Schneider, J. L. (2007). 26th December 2004 great Sumatra–Andaman earthquake: co-seismic and post-seismic motions in northern Sumatra. *Earth and Planetary Science Letters*, *263*(1), 88-103.

Templeton, E. L., and J. R. Rice (2008), Off-fault plasticity and earthquake rupture dynamics: 1. Dry materials or neglect of fluid pressure changes, *J. Geophys. Res.*, 113, B09306, doi:10.1029/2007JB005529.

Viesca, R. C., E. L. Templeton, and J. R. Rice (2008), Off-fault plasticity and earthquake rupture dynamics: 2. Effects of fluid saturation, *J. Geophys. Res.*, 113, B09307, doi:10.1029/2007JB005530.

von Huene, R., Langseth, M., Nasu, N., and Okada, H. (1982). A summary of Cenozoic tectonic history along the IPOD Japan Trench transect. *Geological Society of America Bulletin*, *93*(9), 829-846.

Wang, K., and Y. Hu (2006), Accretionary prisms in subduction earthquake cycles: The theory of dynamic Coulomb wedge, *J. Geophys. Res.*, 111, B06410, doi:10.1029/2005JB004094.

Westbrook, G. K., and Smith, M. J. (1983). Long decollements and mud volcanoes: Evidence from the Barbados Ridge Complex for the role of high pore-fluid pressure in the development of an accretionary complex. *Geology*, *11*(5), 279-283.

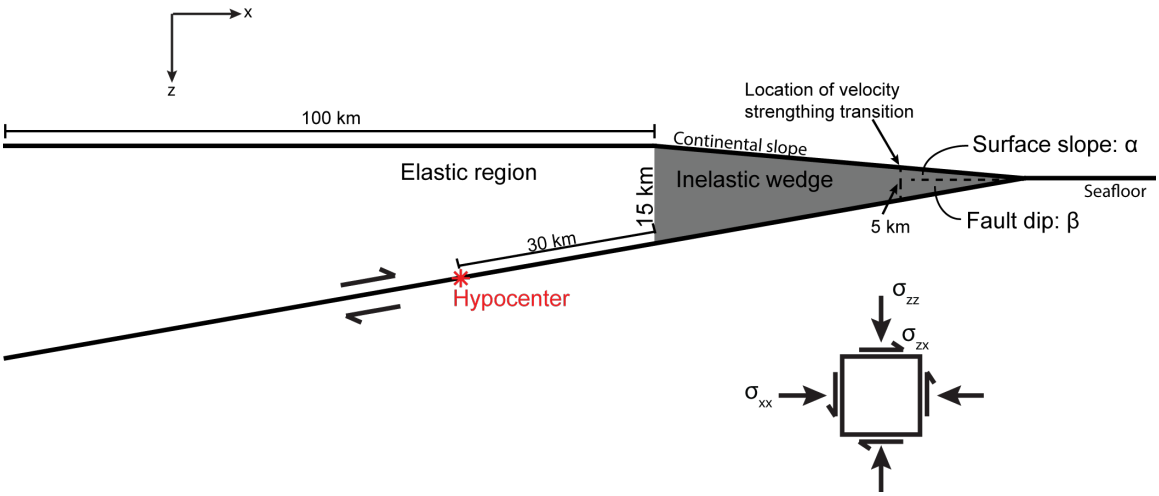

Figure 4.1. Model geometry. A dipping fault (either 10° or 15° dip) is embedded in a homogeneous half space. The inelastic wedge is allowed to deform inelastically (gray region), via the Mohr-Coulomb yield criterion. The rest of the domain is elastic. The red star indicates the hypocenter, which is 30 km from the terminus of the wedge for both fault dips. In some models, the updip portion of the fault is governed by velocity strengthening friction, beginning at a location on the fault below the part of the wedge that has 5 km thickness.

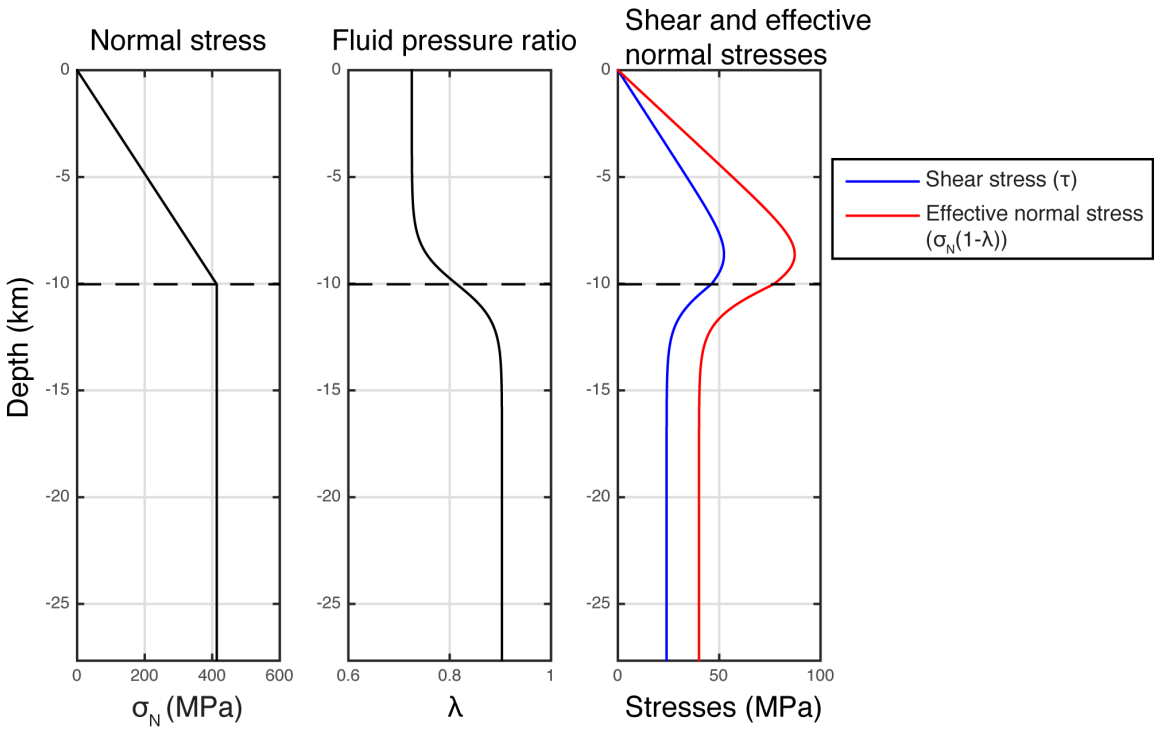

Figure 4.2. On fault stress profile with depth. Total normal stress increases linearly due to overburden until the part of the fault at the left most terminus of the wedge; normal stress is held constant after this value. Normal stress is multiplied by (1 - λ), where λ a fluid pressure ratio, so that the strength of the fault governed by an effective stress. Shear stress is set to be 0.6 times the effective normal stress along the entire fault.

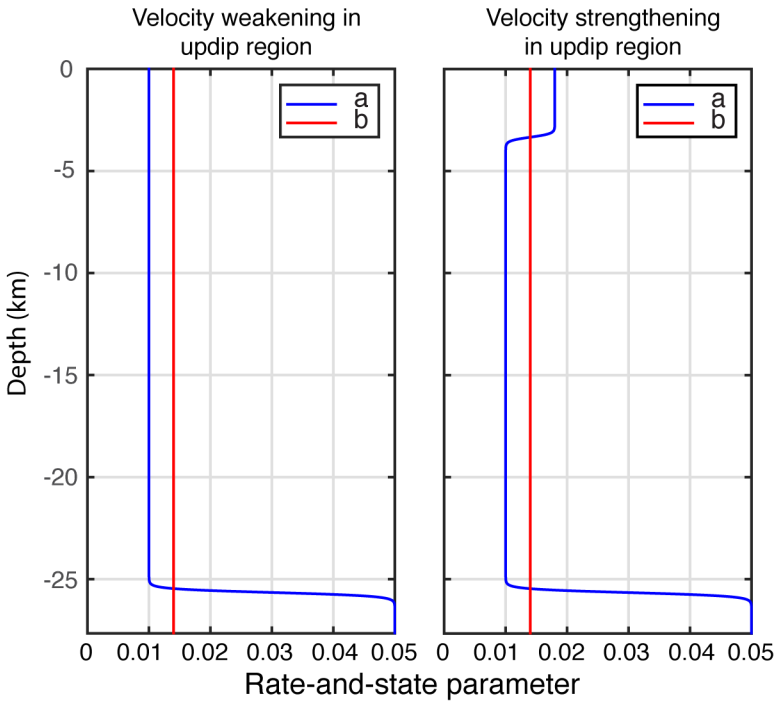

Figure 4.3. Rate-and-state friction parameters as a function of depth. The direct effect parameter *a* is depth dependent; the state variable evolution parameter *b* is held a constant value of 0.014 along the entire fault. In the cases with velocity weakening in the updip portion of the fault, *a* is held at 0.01 up to the trench. In the case where the shallow portion of the fault is velocity strengthening, *a* increases to 0.018. At a location 10 km from the downdip end of the fault, *a* increases to 0.05 in both cases, to arrest rupture at this deep boundary.

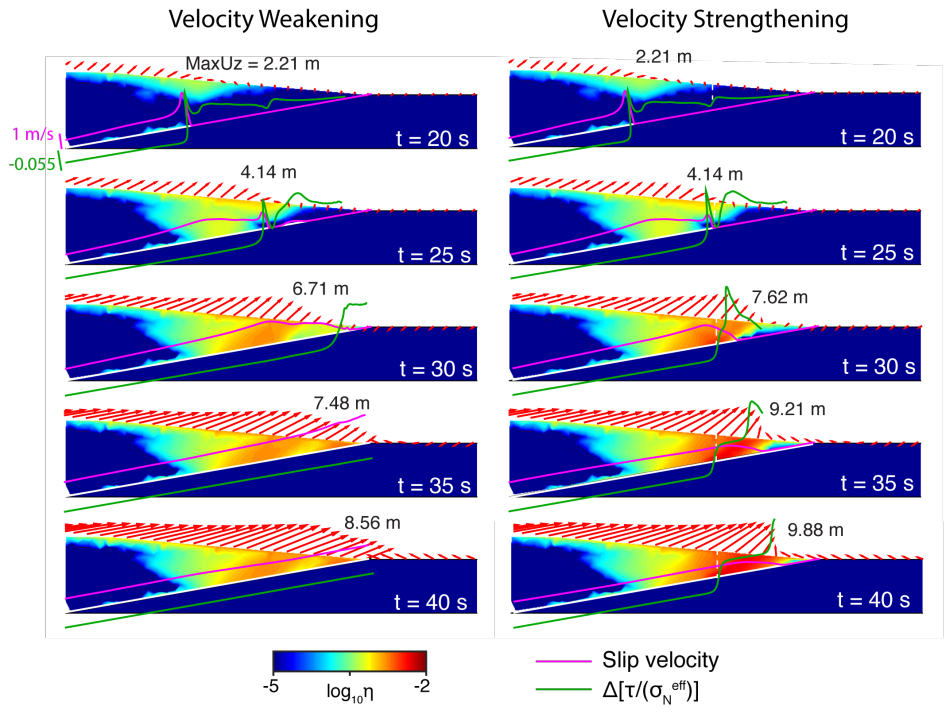

Figure 4.4. Snapshots of the accretionary wedge centered around the time that the rupture enters the velocity strengthening portion of the fault (right panels) in comparison with the equivalent model with only velocity weakening (left panels). The time of each snapshot is indicated. The fault is shown by a solid white line. The color scale shows the log of inelastic shear strain. The magenta curve is slip velocity, the green curve is the change from initial friction, $\Delta[\tau/\sigma_N^{eff}]$. The red arrows show the surface displacement vectors, the maximum value of vertical uplift is indicated by the number next to these arrows. The rupture is mostly identical until the rupture reaches the shallow portion of the trench (at t = 30 s), where slip is terminated in the velocity strengthening model but ruptures to the trench in the velocity weakening model. A large increase in basal friction in the velocity strengthening model causes more failure in that case.

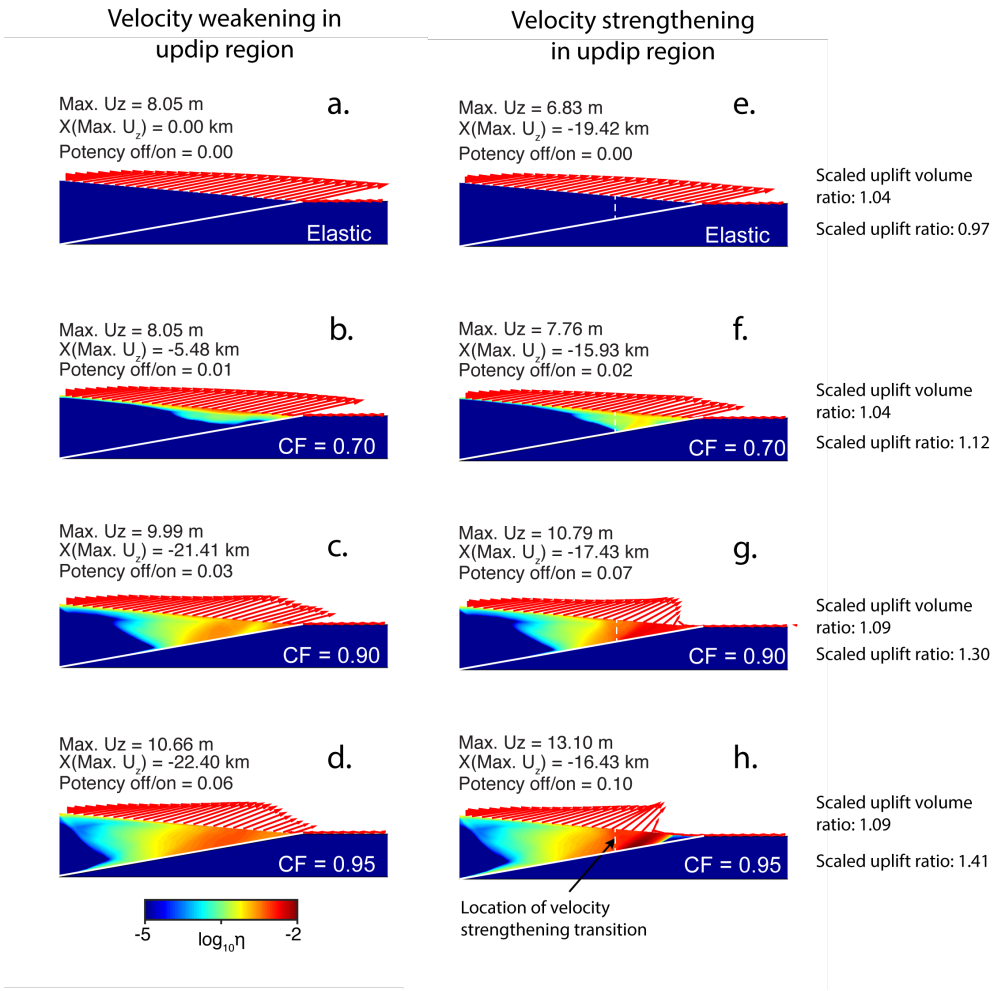

Figure 4.5. Comparison of final inelastic strain and surface displacements between cases with 15 ° taper and either velocity weakening (a-d) or velocity strengthening (e-h), with different values of CF. 'Max. Uz' is the maximum vertical uplift, 'X(Max. Uz)' is the x-value for the location of Max. Uz, 'Potency off/on' is the ratio of off- to on-fault potency, 'Scaled uplift volume ratio' is the ratio between the velocity strengthening and weakening cases of volume normalized by respective moment, and 'Scaled uplift ratio' is a similar ratio but for just the peak value of vertical uplift. Cases with velocity strengthening clearly have more inelastic failure in the wedge in comparison to their corresponding velocity weakening cases. This leads to overall higher uplift, especially when CF is high.

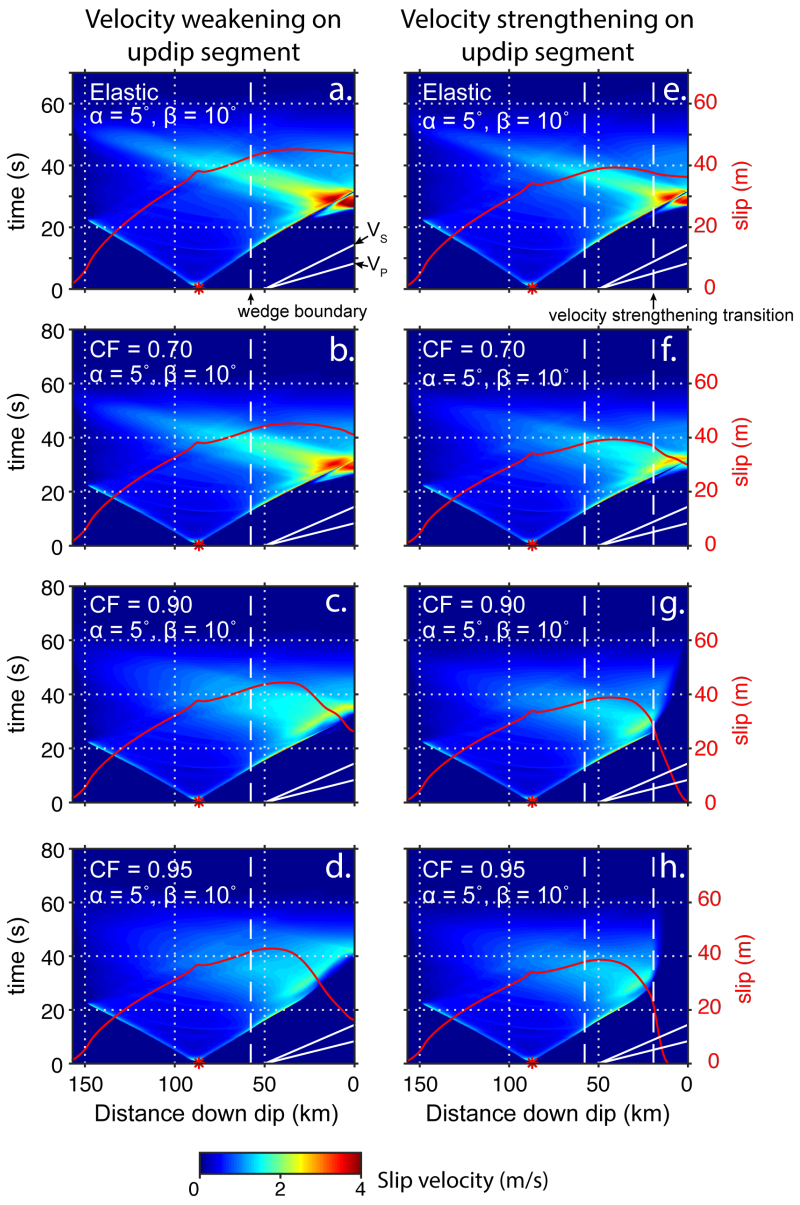

Figure 4.6. Slip velocity time histories for the cases shown in Figure 4.5. The color scale is slip velocity, the red curve indicates the final slip distribution. White dashed lines indicate the along fault location of the left end of the wedge and the beginning of the velocity strengthening region. The P- and S- wave time distance curves are shown. Overall, velocity strengthening diminishes rupture and leads to little to zero slip, especially when CF is high.

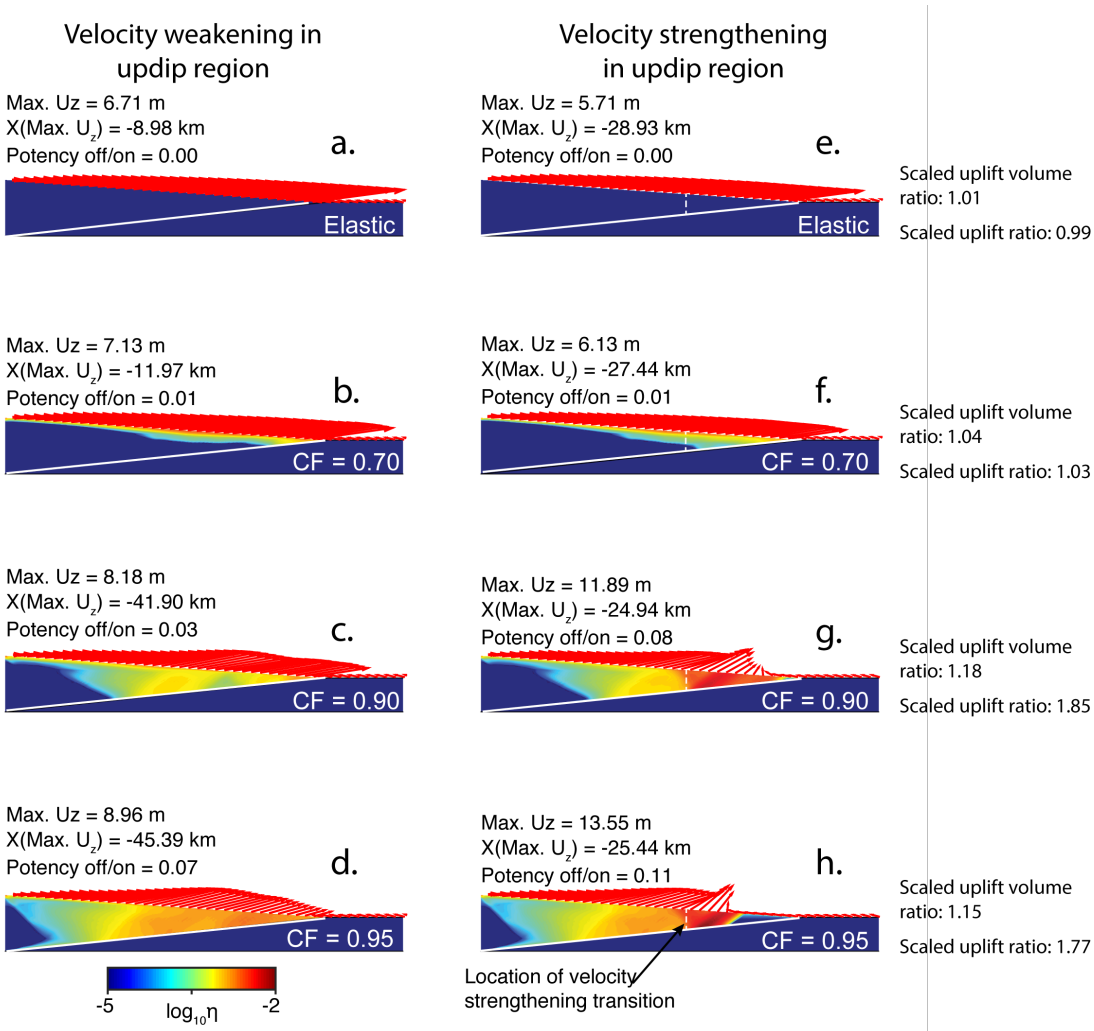

Figure 4.7. Same as Figure 4.5 but for 10° taper angle. In the case with velocity strengthening and CF = 0.95 (figure 7h), a large shear localization is apparent, which corresponds to a splay fault in the accretionary wedge.

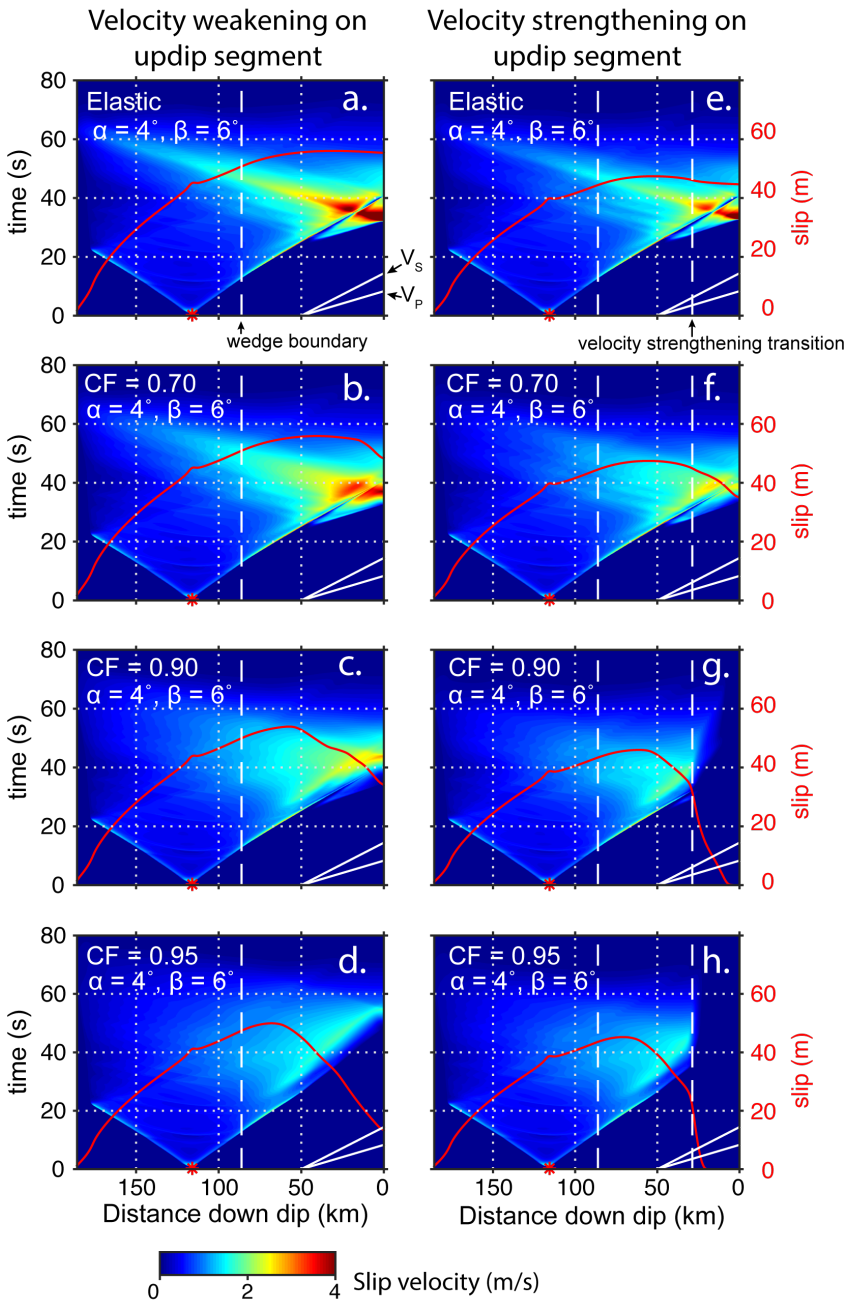

Figure 4.8. Same as Figure 4.6 but for 10° taper angle.

Chapter 5

Generation of Shear Motion from an Isotropic Explosion Source by Scattering in Heterogeneous Media

Abstract

One challenging task in explosion seismology is development of physical models for explaining the generation of S-waves during underground explosions. Recent analysis of ground motion from chemical explosions during the Source Physics Experiment [Pitarka et al., 2015] suggest that while a large component of shear motion was generated directly at the source, additional scattering from heterogeneous velocity structure and topography are necessary to better match the recorded data. In our study we used a stochastic representation of small-scale velocity variability in order to produce high-frequency scattering, and analyze its implication on shear motion generation during underground explosions. In our stochastic velocity model the key parameters that affect scattering are the correlation length and the relative amplitude of velocity perturbations. Based on finite-difference simulations of elastic wave propagation from an isotropic explosion source we find that higher velocity perturbations result in shear motion, while the correlation length, which controls the scatterers size, affects the frequency content of the scattered wave field.

5.1. Introduction

Geophysical monitoring for detecting and discriminating explosions from earthquakes relies on ground motion waveform data. In principal, an isotropic explosion source can only generate P-waves. Thus, most discrimination methods rely on P/S-wave amplitude ratios (e.g. Taylor et al., 1989; Kim et al., 1993; Walter et al., 1995; Hartse et al., 1997). Studies that employ these methods have been relatively successful in discrimination explosions from earthquakes; however, the distinctions between these two seismic sources are challenged by the fact that some explosions generate a significant amount of shear motion. In light of this, a better understanding of physical mechanisms for S-wave generation during explosions is necessary in order to better characterize explosive sources (Walter et al., 2007). The Source Physics Experiment (SPE), an ongoing series of underground chemical explosions at the Nevada National Security Site (NNSS), provides ground motion recordings of controlled chemical explosion sources in an effort to better understand the processes involved during explosions in both the source region and far field (Snelson et al., 2013). The objective of our study is to provide insight into the wave propagation scattering effects on shear motion generation that can help the interpretation of waveforms observed during the SPE explosions.

Several factors explaining shear motion generation as a result of non-linear and linear processes in the immediate vicinity of the explosive source have been proposed and modeled. These models include spall (or "spall slapdown"; Day et al., 1983; Day and McLaughlin, 1991), explosion-induced release of tectonic prestress (Wallace et al., 1985; Day et al., 1987; Stevens and Thompson, 2015), and sliding on newly formed or

preexisting cracks and joints due to the intense stresses in the immediate vicinity of the explosion (Johnson and Sammis, 2001; Patton et al., 2005; Vorobiev et al., 2015). The validation of these models using recorded data is complicated, since wave propagation is a large contributor to observed waveform characteristics. Specifically, a significant amount of shear motion from explosive sources may be a result of scattering of seismic waves, especially for explosions at shallow depths (e.g. Myers et al., 1999). This process can consist of P-, S-, or surface wave refractions, as well as p-S and Rg-S conversions that arise as waves propagate through complex Earth structures. Thus, accountability for path effects and their separation from source effects are necessary steps for more accurately discriminating between seismic sources (Taylor et al., 2002). Scattering may occur when seismic waves encounter topography at the free surface or heterogeneous velocity structures. Modeling efforts to address contributions from surface topography (Pitarka and Helmberger, 2009; Rodgers et al., 2010; Takemura et al., 2015) and large-scale heterogeneous velocity structure (e.g., McLaughlin et al., 1987) are abundant and have confirmed that they give rise to waveform complexity and reverberant coda even during explosions. Detailed modeling of topographic effects in particular regions can be performed with a high level of confidence, since we can directly observe the topographic profile at the surface. Similarly, large-scale velocity structures from geologic or tomographic models are relatively well constrained and have been shown to give rise to synthetic seismograms that match the observations quite well at low frequencies. However, deterministic modeling of ground motions at high frequencies commonly requires features of the velocity structure that are not resolved reliably by tomographic techniques. The goal of the current study is to model scattering and generation of

tangential motion, as a result of these small-scale features.

Resolution of Earth's velocity structure at decreasing wavelengths is difficult. Early studies suggested that the seemingly random parts of a waveform (e.g. the higher frequency parts of the waveform and the seismic coda) might be modeled with a statistical treatment rather than a purely deterministic one (Aki and Chouet, 1975; Zeng et al., 1991). Proposed physics-based models for wave scattering involve direct application of a random velocity field with some statistical characteristics into numerical models for wave propagation. Frankel and Clayton (1986) developed velocity models with perturbations in velocity that follow a variety of different spatially statistical distributions. In their model random velocity fields are characterized by correlation functions. In analysis of random media with different statistical distributions they found that in the presence of an explosive source, all classes of random media allowed multiple scattering which led to a significant amount of P-S conversions as evidenced by non-zero curl during wave propagation. However, they found that only Von Karman stochastic media with fractal distribution would account for teleseismic travel time anomalies and seismic coda at frequencies greater than 30 Hz similar to those observed during earthquakes. Analysis of borehole sonic logs that found velocity fluctuations to be described by a stochastic fractal distribution later supported this property of the crustal velocity structure (Holliger, 1996). Thus as a result of these findings, modeling efforts of this type have become common in ground motion models and usually incorporate media with Von Karman correlation functions (Hartzell et al., 2010; Imperatori and Mai, 2013; Takemura et al., 2015).

Pitarka et al. (2015) included stochastic velocity perturbations to a 3D velocity

model of the SPE site developed by combining geological structure, geophysical observations and ambient noise tomography. This was done specifically with the goal of reproducing recorded tangential motion from the SPE-3 explosion. Simulations using this velocity model and a physics-based source model suggested that a large contribution to shear motion is from nonlinear processes in the source region; however additional scattering was needed to reproduce the observed seismic waveforms. In the interest of computational efficiency, the method of wave number domain filtering of random numbers, proposed by Frankel and Clayton (1986) was not used, as the required three-dimensional Fourier transform is computationally expensive, especially when the simulation domain is large. Instead, velocity perturbations are generated in the spatial domain by generating a set of random numbers and smoothing them over an ellipsoidal volume with a Gaussian weighting function (Pitarka and Ichinose, 2009).

Though the model of Pitarka et al. (2015) was able to generate a large amount of tangential motion via scattering, we would like to better characterize the statistical parameters used in the generation of complex velocity structure and understand their contributions to the generation of tangential motion. In consideration of this, the use of relatively simple models with small computational domains allowed us to run a large number of models with varying statistical parameters. Our study is largely an experimental one in which we attempt to further understand model sensitivity to statistical aspects of the random velocity model used. The goal is to better understand and quantify the differences in results obtained with variations in these parameters, aiming towards providing constrains to development of near-source stochastic velocity models for explosion source modeling.

5.2. Finite-difference modeling

We model wave propagation from an explosive source in an elastic half space with a random velocity structure. To generate the random velocity structures we use the spatial domain method of Pitarka and Ichinose (2009), which gives rise to a Gaussian-like medium. To address the commonly held notion that small-scale velocity structure has fractal characteristics, we also tested cases with random velocity structures given by Von Karman distributions (e.g. Frankel and Clayton, 1986). We found the differences in the results from the two models to be negligible; thus all results shown here are for models with velocity structures generated by the first method. Our velocity models have two key parameters: a correlation length, **L**, and a scaling factor, **r**, which essentially controls the amplitude of the deviation from the background velocity. Figure 1 shows two typical examples of velocity models used in this study. One set of models consists of homogenous half-space with random perturbations. The second set considers a model with a low-velocity surface layer above the half-space. Background velocities (i.e. average velocities) in the half-space are Vp = 4330 m/s and Vs = 2700 m/s, and in the low-velocity layer are Vp = 2000 m/s and Vs = 1000 m/s. Perturbations are only applied to velocity, thus the density has a constant value of 2100 kg/m^3 and 2000 kg/m^3 in the half-space and the low-velocity layer, respectively.

In all simulations we used a purely isotropic explosion source located 120 meters below the free surface. Wave propagation is simulated using the SW4 seismic wave propagation code, based on a 4th order summation by parts finite-difference method (Petersson and Sjogreen, SW4 User's Guide). The computational domain is 10x10 km with 10 m grid spacing. The domain is bounded by a free surface boundary at z = 0 km

and absorbing boundaries on all other sides. The grid spacing was chosen so that the maximum resolvable frequency is 10 Hz. Stations are located at the surface in a circular grid around the source at distances of 1, 2, and 3 km, with azimuthal spacing of 20 degrees (Figure 1).

5.3. Results

Scattering at small-scale velocity heterogeneities results in immediately noticeable random perturbations to seismic waveforms emanating from an explosive source, with a significant amount of ground motion leaking into the transverse direction. This can be seen in Figure 2, where time series from stations in homogeneous and heterogeneous media are compared. In Figure 2, signals from equidistant stations at a number of azimuths are shown in each subplot. In the homogeneous media, the isotropic source gives rise to identical seismic records at all azimuths. In contrast, the heterogeneous medium includes azimuthally varying wave paths, and results in apparently random perturbations to the waveforms of the homogeneous case as well as reverberant at each station in all three components. Deviations from the waveforms of the homogeneous case occur as waves are scattered into different directions. Thus, seismic waves that are initially polarized into the radial and vertical directions by the isotropic source are redirected into the transverse direction mainly by P-S conversion and surface wave refraction.

To compare the tendency for models to generate shear motion, we plot the ratios of amplitude spectra for pairs of cases as a measure of relative S-wave conversion by scattering (Figure 3). Each curve represents the average of the ratio over all stations at a given distance. 90% confidence limits are also provided. The left panels show a ratio of

spectral power between a case with **r** = 8% and **r** = 3% for the half-space model in which **L** is held constant at 400 m. At all 3 distances, the shear motion is greater for the case with higher **r** over the entire considered frequency range. This is due to the fact that the more drastic velocity variations enhance scattering effects, allowing more energy to leak into the transverse component of motion. Large material contrasts may cause waves to propagate at larger refraction angles, and through stronger reflectors.

In the method used for generating the random velocity structure, the correlation length, **L**, corresponds to the standard deviation of the Gaussian weighting function used to smooth the random number distribution. Thus, **L** essentially sets a characteristic size for scatterers (which is not necessarily equal to **L**), where smaller **L** leads to scattering over smaller wavelengths. The right panels in Figure 3 provide spectral ratios between half-space models with **L** = 1200 m and **L** = 400 m, and **r** = 8%. It becomes clear that the capacity of random perturbations for generating shear motion is frequency dependent. Below ~2 Hz the ratio is relatively close to 1 (since the plot in Figure 3 is a log scale a ratio of 1 plots as 0), with a slight tendency for the case with **L** = 1200 m to have more energy in the transverse component of motion. However, at higher frequencies, the ratio clearly drops below 1 as more shear motion is generated in the **L** = 400 m case at higher frequencies. Overall, this reflects the fact that scatterers of different characteristic sizes will excite different parts of the ground motion spectra. In addition, we found that shear motion generally increases with propagation distance, however this result is not immediately noticeable by these plots.

To characterize a model's efficiency for generating shear motion, we looked at the relative amount of transverse to radial kinetic energy (T/R, hereafter). The variation

of T/R measured at 3km distance, at different azimuths, for the half-space and one layer over half-space velocity models is shown schematically in Figure 4. The length of each vector represents the value of T/R; the direction of the vector points to the azimuth of the station at which the energy is calculated. By comparing mean values (shown below each plot), we find that the energy ratio increases with decreasing **L**, and increases with increasing **r**. On average T/R increases from 10% to 16% when **L** decreases from **L**=1200m to **L**=400m. The addition of a softer shallow layer enhances the contribution of **r** to T/R increase. In this case T/R increases by a factor of three, from 11% to 33% for **r** = 8%. It is clear that additional structural complexity enhances scattering effects, thus creates more shear motion. All plots shown in Figure 4 are only for the ring of stations at 3 km from the source. Comparisons of the transverse-radial energy ratio for cases at closer stations, not shown here, reveal that it gradually increases with distance. This is because scattering effects accumulate as waves propagate to farther distances through the complex velocity structure.

5.4. Discussion and Conclusion

Complexity of ground motion recordings and generation of a significant amount of shear motion during underground explosions can be explained by a combination of source and path effects. Modeling of path effects requires velocity models that accounts for structural effects on frequencies of monitoring interest as high as 10Hz. Though current geologic and tomographic models account for structural complexities of various sizes, their capability at resolving small-scale heterogeneities is limited. The representation of such heterogeneities in velocity models used in high frequency simulations requires a statistical approach (e.g., Imperatori and Mai, 2015; Obermann et

al., 2013). Generation of a pseudorandom velocity structure and its employment in numerical simulations of wave propagation provides insight into scattering processes.

We analyzed the effects of parameters used in a stochastic seismic velocity model: the perturbation scaling factor, **r**, and perturbation correlation length, **L**. Overall, our numerical experiments for an isotropic explosion source show that a non-negligible amount of shear motion is generated in randomly heterogeneous media near the source. Our study shows that **r**, has a large influence on the amount of shear motion produced by wave scattering. When **r** increases, the amplitude of shear motion also increases. These effects are distance dependent. The amplitude of transverse component of motion relative to that of radial component increases with distance as scattering effects accumulate during wave propagation through complex media. The frequency content of the scattered wave field depends on the perturbation correlation length, **L**. More specifically, longer correlation lengths correspond to larger scatterers and thus affect the long period (low frequency) part of the signal. Shorter correlation lengths conversely affect the short period (high frequency) part of the signal.

It is important to note that we have prescribed a statistical description of the velocity heterogeneities for a rock model. This description may not completely cover the broad range of distribution in the crust. Furthermore, the use of constant parameters **r** and **L** throughout the entire domain would represent the simplest end member case, while in reality these parameters may vary spatially. However, we expect that the general conclusions reached here are not strictly linked to specific seismic properties of the materials used in our numerical experiments. Given its significant effect on ground motion, wave scattering has to be taken into account in inversions of waveform data for

explosion source deviatoric components.

Chapter 5, in partial form, has been submitted for publication of the material as it may appear in *Bulletin of Seismological Society of America – Short Notes*: Hirakawa, E. T., Pitarka, A. and R. Mellors. Generation of Shear Motion from an Isotropic Expolosion Source by Scattering in Heterogenous Media. I was the primary investigator and author of this paper.

References

Aki, K., and Chouet, B. (1975). Origin of coda waves: source, attenuation, and scattering effects. *Journal of geophysical research*, *80*(23), 3322-3342.

Day, S. M., and McLaughlin, K. L. (1991). Seismic source representations for spall. *Bulletin of the Seismological Society of America*, *81*(1), 191-201.

Day, S. M., Rimer, N., and Cherry, J. T. (1983). Surface waves from underground explosions with spall: Analysis of elastic and nonlinear source models. *Bulletin of the Seismological Society of America*, *73*(1), 247-264.

Day, S. M., Cherry, J. T., Rimer, N., and Stevens, J. L. (1987). Nonlinear model of tectonic release from underground explosions. *Bulletin of the Seismological Society of America*, *77*(3), 996-1016.

Frankel, A., and Clayton, R. W. (1986). Finite difference simulations of seismic scattering: implications for the propagation of short-period seismic waves in the crust and models of crustal heterogeneity. *Journal of Geophysical Research B*, *91*(B6), 6465-6489.

Hartse, H. E., Taylor, S. R., Phillips, W. S., and Randall, G. E. (1997). A preliminary study of regional seismic discrimination in central Asia with emphasis on western China. *Bulletin of the Seismological Society of America*, *87*(3), 551-568.

Hartzell, S., Harmsen, S., and Frankel, A. (2010). Effects of 3D random correlated velocity perturbations on predicted ground motions. *Bulletin of the Seismological Society of America*, *100*(4), 1415-1426.

Holliger, K. (1996). Upper-crustal seismic velocity heterogeneity as derived from a variety of P-wave sonic logs. *Geophysical Journal International*, *125*(3), 813-829.

Imperatori, W., and Mai, P. M. (2013). Broad-band near-field ground motion simulations in 3-dimensional scattering media. *Geophysical Journal International*, *192*(2), 725-744.

Imperatori, W., and Mai, P. M. (2015). The Role of Topography and Lateral Velocity Heterogeneities on Near-Source Scattering and Ground Motion Variability. *Geophys. J. Int. 202 (3)*: 2163-2181, doi: 10.1093/gji/ggv281.

Johnson, L. R., and Sammis, C. G. (2001). Effects of rock damage on seismic waves generated by explosions. *pure and applied geophysics*, *158*(11), 1869-1908.

Kim, W. Y., Simpson, D. W., and Richards, P. G. (1993). Discrimination of earthquakes

and explosions in the eastern United States using regional high‐frequency data. Geophysical Research Letters, 20(14), 1507-1510.

McLaughlin, K. L., Anderson, L. M., and A.C. Lees (1987). Effects of local geologic structure on Yucca Flats, Nevada Test Site, explosion waveforms: two-dimensional linear finite-difference simulations. Bulletin of the Seismological Society of America, 77(4), 1211-1222.

Myers, S. C., Walter, W. R., Mayeda, K., and Glenn, L. (1999). Observations in support of Rg scattering as a source for explosion S waves: regional and local recordings of the 1997 Kazakhstan depth of burial experiment. Bulletin of the Seismological Society of America, 89(2), 544-549.

Obermann, A, T. Planès, E. Larose, C. Sens-Schönfelder and M. Campillo (2013) Depth sensitivity of seismic coda waves to velocity perturbations in an elastic heterogeneous medium. *Geophys. J. Int.* (July, 2013) 194 (1): 372-382. doi: 10.1093/gji/ggt043

Patton, H. J., Bonner, J. L., and Gupta, I. N. (2005). Rg excitation by underground explosions: insights from source modelling the 1997 Kazakhstan depth-of-burial experiment. Geophysical Journal International, 163(3), 1006-1024.

Pitarka, A., and G. Ichinose (2009). Simulating forward and backward scattering in viscoelastic 3D media with random velocity variations and basin structure, Tech. Rep., USGS, award number 06HQGR0042.

Pitarka, A., and D. V. Helmberger (2009). Analysis and simulation of 3D scattering due to heterogeneous crustal structure and surface topography on regional phases; magnitude and discrimination, Report. AFRL-RV-HA-TR-2009-1058.

Pitarka, Arben, Robert J. Mellors, William R. Walter, Souheil Ezzedine, Oleg Vorobiev, Tarabay Antoun, Jeffery L. Wagoner, Eric M. Matzel, Sean R. Ford, Arthur J. Rodgers, Lewis Glenn, and Mike Pasyanos (2015). Analysis of Ground Motion From an Underground Chemical Explosion", Bull. Seism. Soc. Am., submitted 03/09/15, accepted 07/15,15.

Rodgers, A. J., Petersson, N. A., and Sjogreen, B. (2010). Simulation of topographic effects on seismic waves from shallow explosions near the North Korean nuclear test site with emphasis on shear wave generation. Journal of Geophysical Research: Solid Earth (1978–2012), 115(B11).

Snelson, Catherine M., Robert E. Abbott, Scott T. Broome, Robert J. Mellors, Howard J. Patton, Aviva J. Sussman, Margaret J. Townsend, and William R. Walter. "Chemical explosion experiments to improve nuclear test monitoring." Eos, Transactions American Geophysical Union 94, no. 27 (2013): 237-239.

Stevens, J. L., and Thompson, T. W. (2015). 3D Numerical Modeling of Tectonic Strain Release from Explosions. Bulletin of the Seismological Society of America, 105(2A), 612-621.

Takemura, S., Furumura, T., and Maeda, T. (2015). Scattering of high-frequency seismic waves caused by irregular surface topography and small-scale velocity inhomogeneity. Geophysical Journal International, 201(1), 459-474.

Taylor, S. R., Denny, M. D., Vergino, E. S., and Glaser, R. E. (1989). Regional discrimination between NTS explosions and western US earthquakes. Bulletin of the Seismological Society of America, 79(4), 1142-1176.

Taylor, S. R., Velasco, A. A., Hartse, H. E., Phillips, W. S., Walter, W. R., and Rodgers, A. J. (2002). Amplitude corrections for regional seismic discriminants. In Monitoring the Comprehensive Nuclear-Test-Ban Treaty: Seismic Event Discrimination and Identification (pp. 623-650). Birkhäuser Basel.

Vorobiev, O., Ezzedine, S., Antoun, T., and L. Glenn (2015). On the generation of tangential ground motion by underground explosions in jointed rocks. Geophysical Journal International, 200(3), 1651-1661.

Wagoner, J. L. (2014). Working toward a site-specific geomodel. Nevada National Security Site. RMR2014—Review of Monitoring Research for Ground-Based Nuclear Explosion Monitoring Technologies, Albuquerque, New Mexico, June 18, 2014.

Wallace, T. C., Helmberger, D. V., and Engen, G. R. (1985). Evidence of tectonic release from underground nuclear explosions in long-period S waves. Bulletin of the Seismological Society of America, 75(1), 157-174.

Walter, W. R., Mayeda, K. M., and Patton, H. J. (1995). Phase and spectral ratio discrimination between NTS earthquakes and explosions. Part I: Empirical observations. Bulletin of the Seismological Society of America, 85(4), 1050-1067.

Walter, W. R., Matzel, E., Pasyanos, M. E., Harris, D. B., Gok, R., and Ford, S. R. (2007). Empirical observations of earthquake-explosion discrimination using P/S ratios and implications for the sources of explosion S-waves. LAWRENCE LIVERMORE NATIONAL LAB CA.

Zeng, Y., Su, F., and Aki, K. (1991). Scattering wave energy propagation in a random isotropic scattering medium: 1. Theory. Journal of Geophysical Research: Solid Earth (1978–2012), 96(B1), 607-619.

Zeng, Y., Anderson, J. G., and Su, F. (1995). Subevent rake and random scattering effects in realistic strong ground motion simulation. Geophysical research letters, 22(1), 17-20.

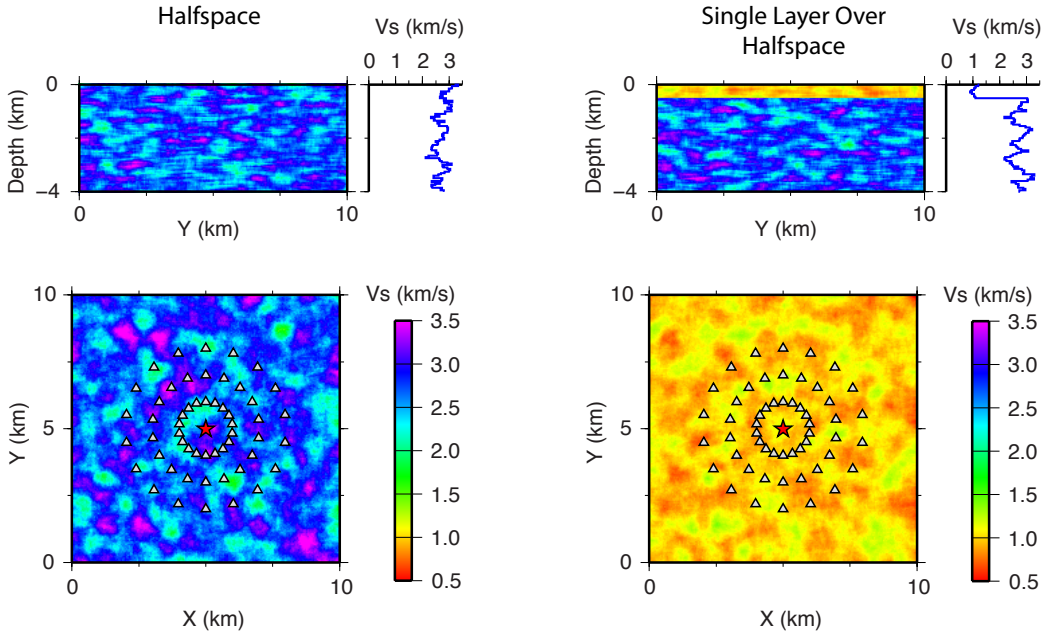

Figure 5.1. Typical velocity models used in this study. Models either consist of a randomly perturbed half-space (left panels) or a low-velocity layer over a half-space (right panels). In all cases the source location is in the center of the domain at 120 m depth. Concentric rings of stations circle the source at distances of 1, 2, and 3 km, with an azimuthal spacing of 20 degrees.

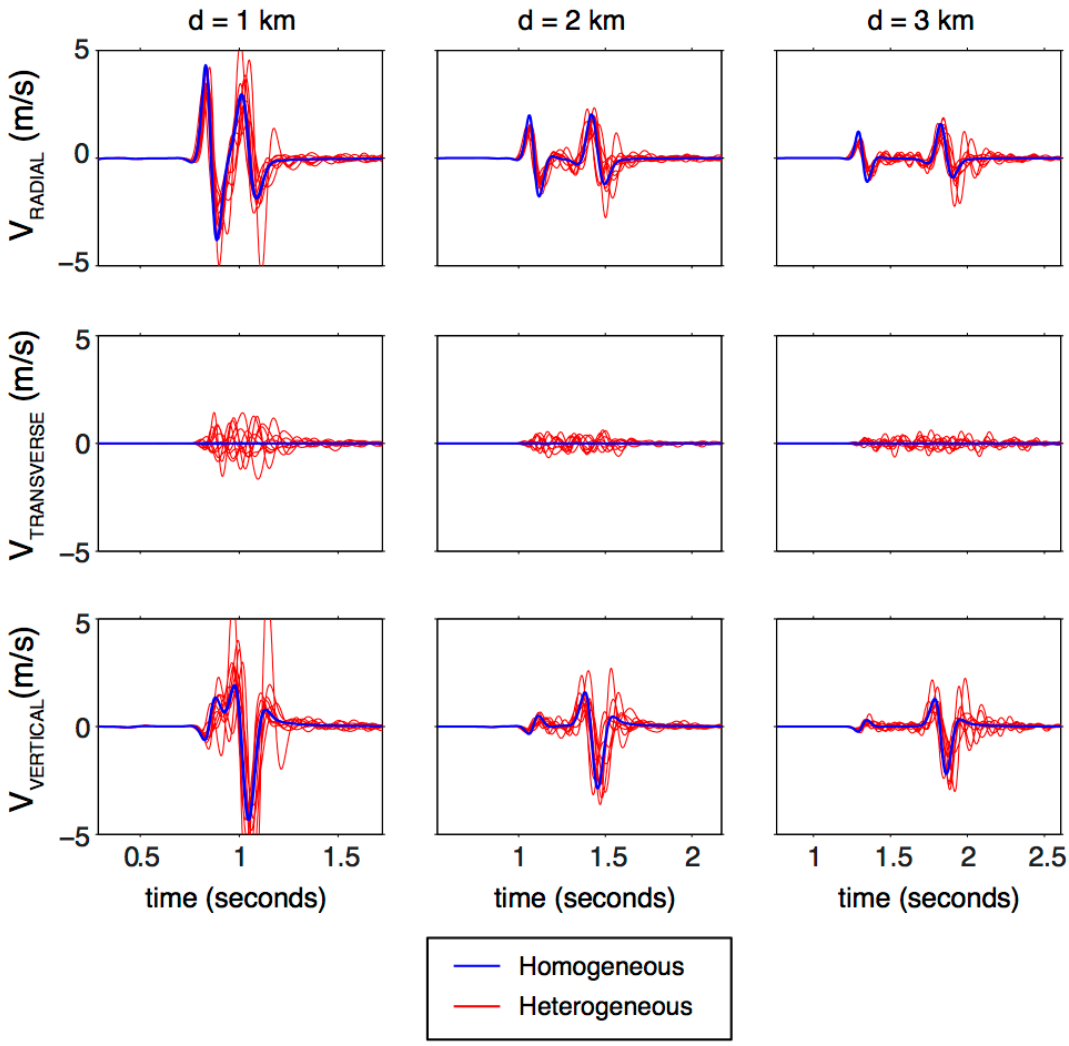

Figure 5.2. Three component time series for homogeneous velocity model (red curves) and stochastic velocity model with **r** = 8% and **L** = 400 m (blue curves). Individual curves of the same color represent time series from stations at different azimuths. Though the main features of the stochastic velocity model time series are similar to those of the homogeneous model, variability with azimuth is significant and is due to the scattered wave field. Scattering leads to a significant amount of energy in the transverse component motion, which is not present in the case of homogeneous model.

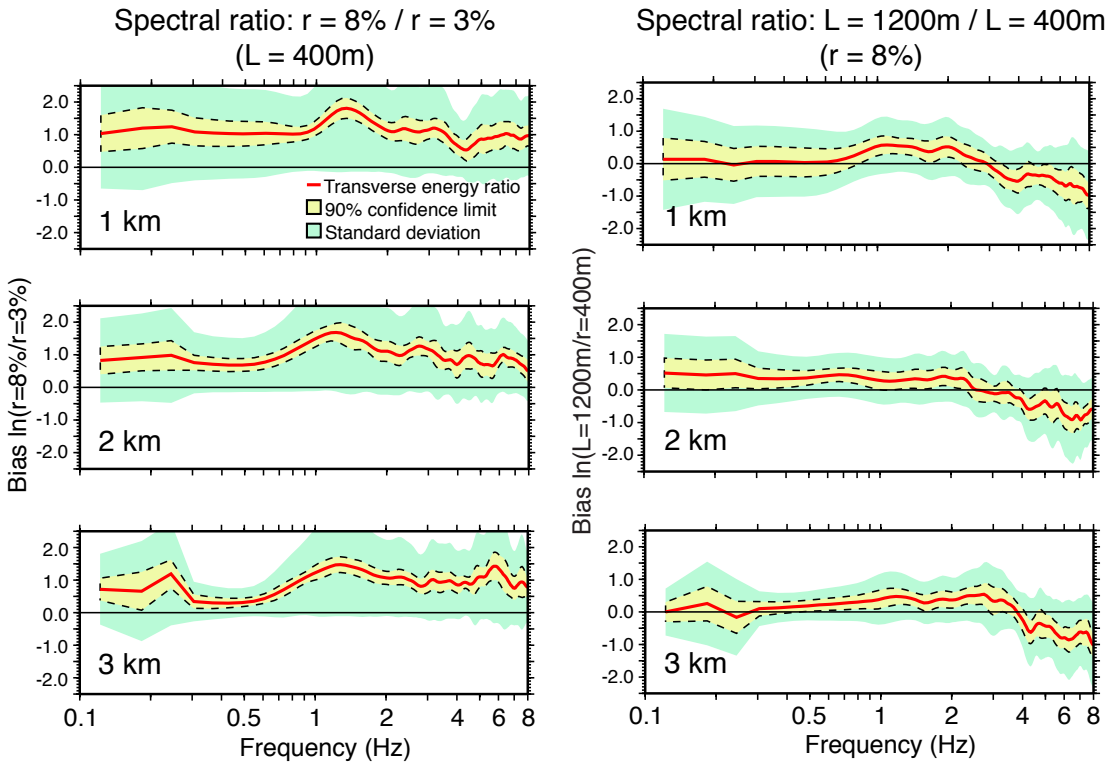

Figure 5.3. Ratios of Fourier amplitude spectra averaged over stations with equal distance from the source. Distance is indicated in the bottom left corner of each panel. Ratios are plotted in log normal scale. Left panels: Spectral ratios between models with **r** = 8% and **r** = 3% (**L** = 400m). Right panels: Spectral ratios between models with **L** = 1200 m and **L** = 400 m (**r** = 8%).

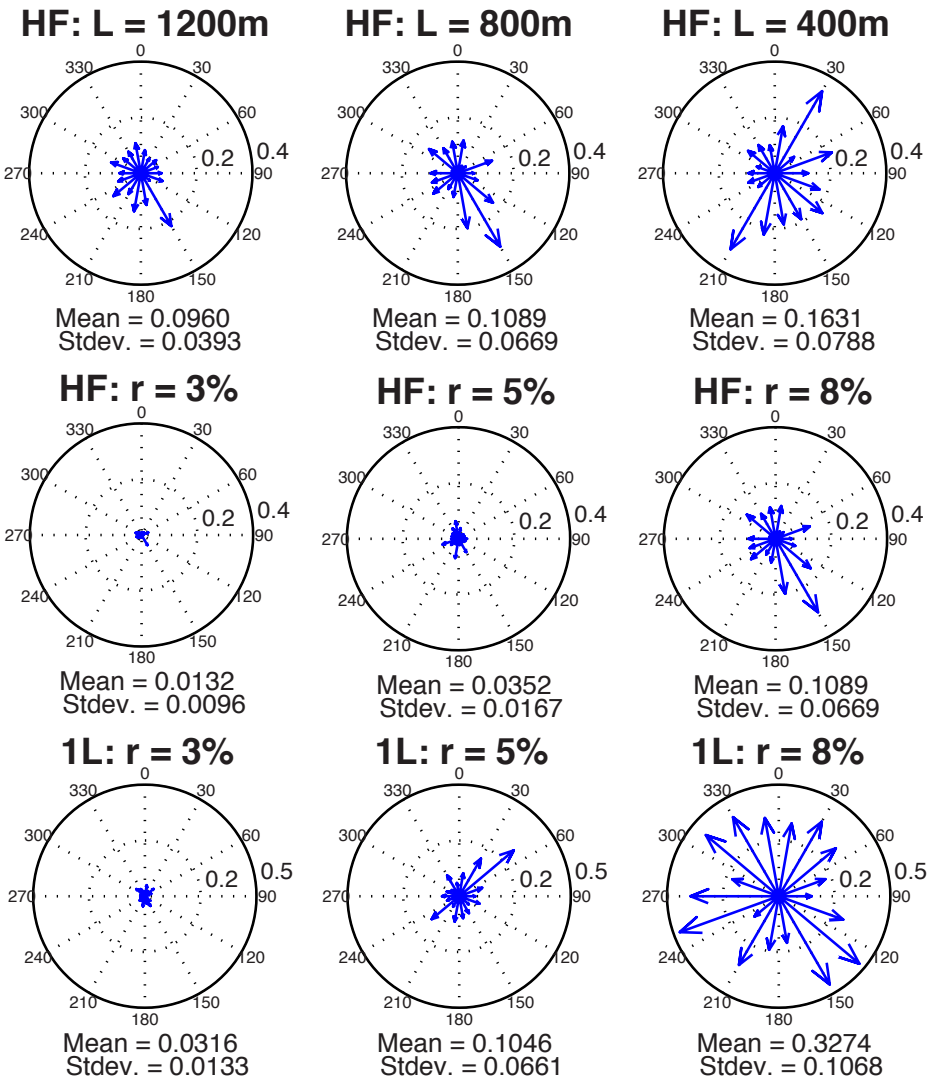

Figure 5.4. Directional plots of relative transverse to radial energy (T/R) for the ring of stations with 3km epicentral distance. Top and middle rows correspond to half-space model (HF), and the bottom row corresponds to one layer over half-space model (1L). The length of the blue vectors denotes T/R at a particular station while the direction points towards the station azimuth. Top row: cases with varying correlation length **L**, and constant **r** = 8%. Middle row: cases with varying **r** and constant **L** = 800 m. Bottom row: same as middle row but for a model with a low-velocity surface layer.

Supplementary Material

The following figures were included as 'supplementary material' in the submission of Chapter 1 to *Journal of Geophysical Research:*

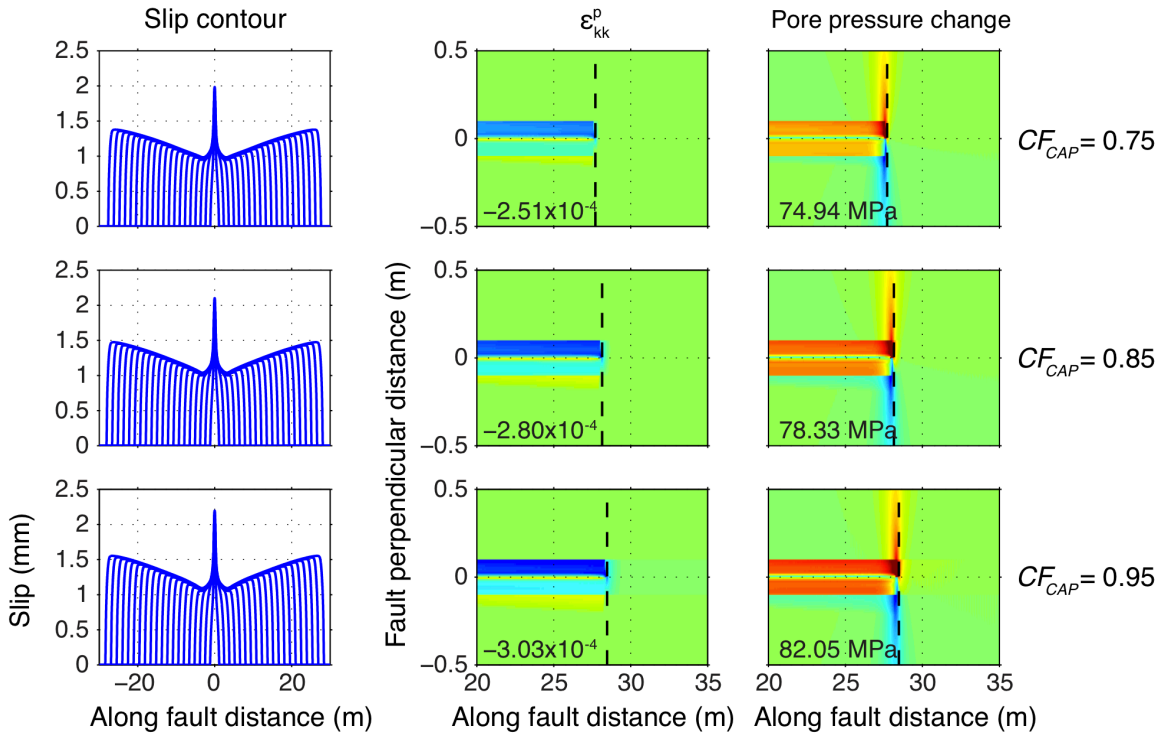

Figure S1. Comparison of results for three CF_{CAP} cases. Slip contours every 0.5 ms (left column), snapshots of inelastic volumetric strain at 8 ms (middle column), and pore pressure distribution at 8 ms (right column) are illustrated. The black dashed line shows the location of rupture front at that time. The color scales are the same as in Figure 5. The number in each panel denotes the peak value in the medium. The weakening effect is not significantly affected by CF_{CAP} .

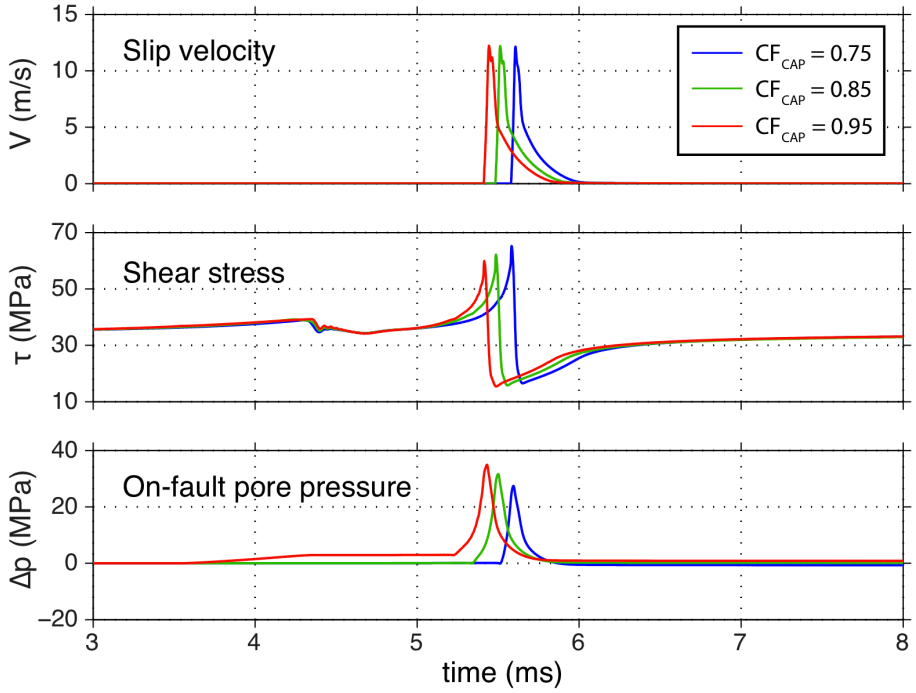

Figure S2. Time histories of slip velocity, shear stress, and on-fault pore pressure at x = 15 m are plotted for the same cases shown in Figure S1. Significant weakening is seen even in the lower CF_{CAP} cases.

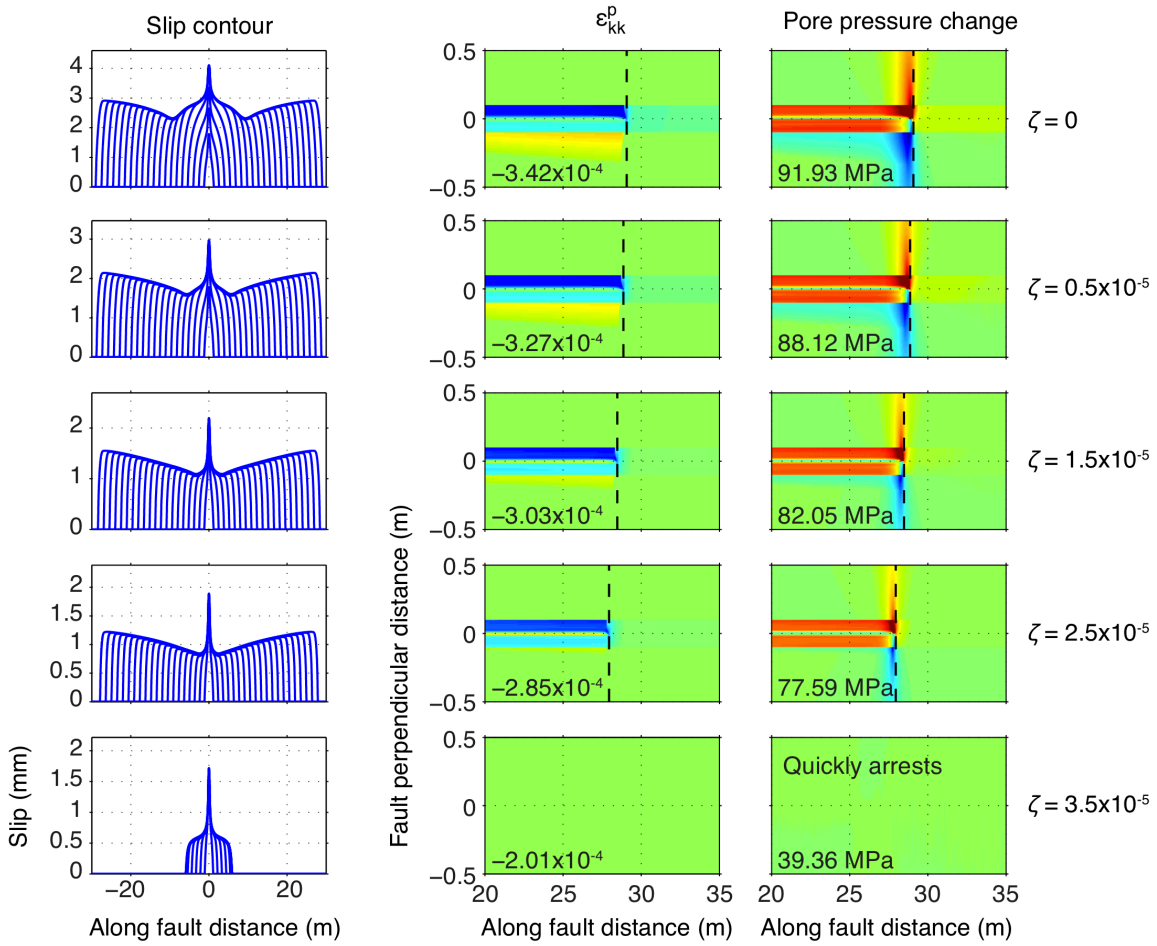

Figure S3. Similar to Figure S1, but effects of steady-state dilatancy factor ζ are shown.

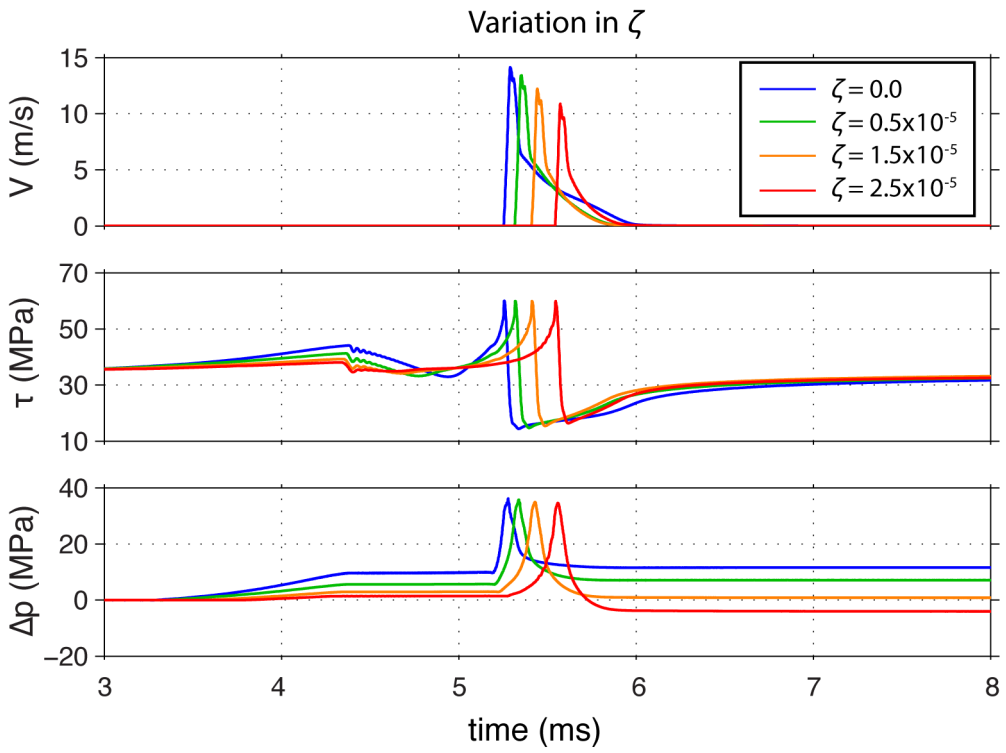

Figure S4. Time histories of slip velocity, shear stress, and on-fault pore pressure at x = 15 m are plotted for the cases shown in Figures S3. Stronger dilatancy leads to rapid pore pressure reduction, larger strengthening, smaller slip velocity, and shorter slip durations.

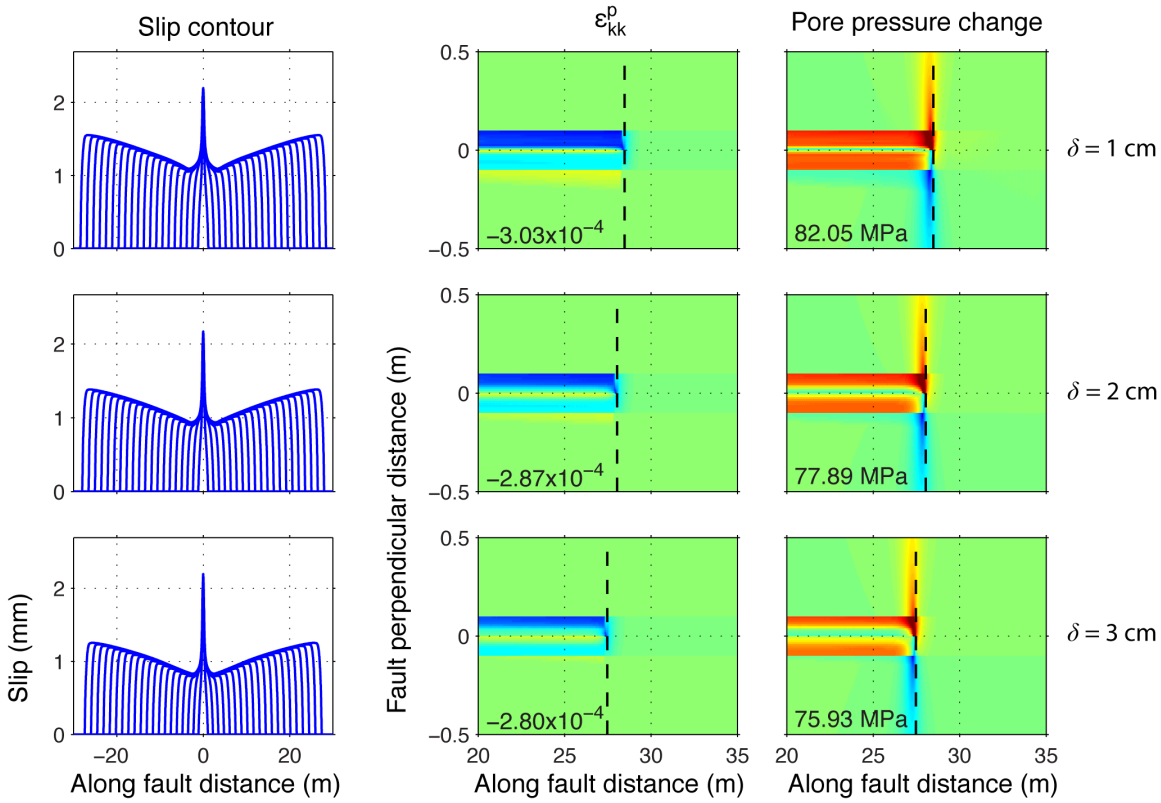

Figure S5. Similar to Figure S1, but effects of standard deviation of evolution velocity are shown.

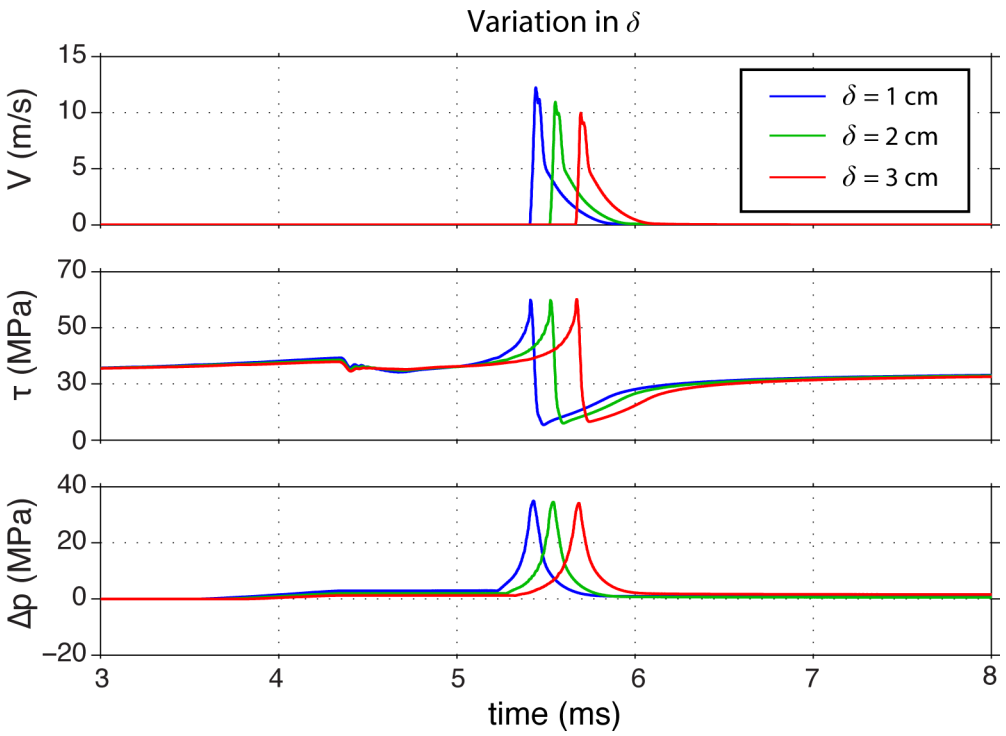

Figure S6. Similar to Figure S4, but effects of standard deviation of evolution velocity are shown.

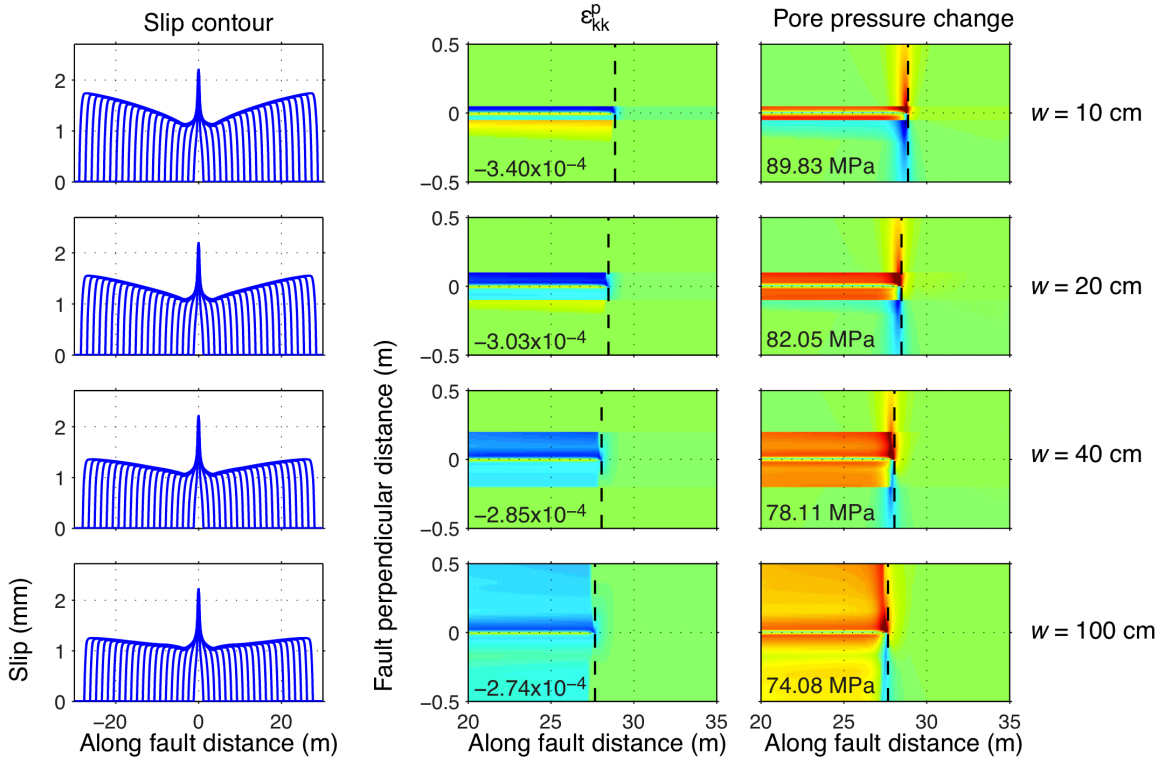

Figure S7. Similar to Figure S1, but effects of gouge layer thickness are shown. As the gouge layer decreases, the weakening is more pronounced and slip is more localized to the fault with larger amplitude. There are also noticeable differences between rupture times for the different cases. Narrower gouge layers allow faster rupture propagation than those with broader gouge widths given the same dilatancy parameters.